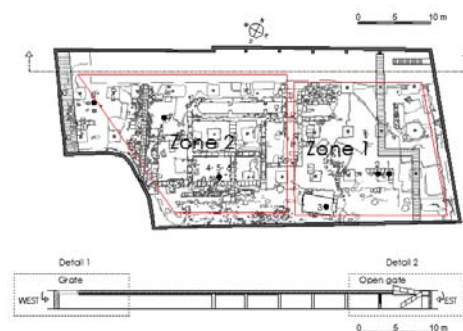
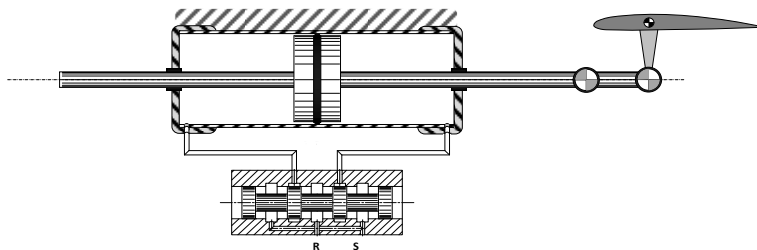
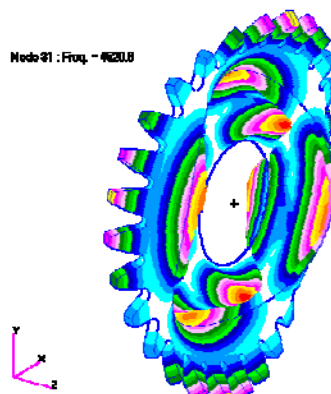


International Journal of Mechanics and Control

Editor: Andrea Manuello Bertetto



Editorial Board of the
International Journal of Mechanics and Control

Published by Levrotto&Bella – Torino – Italy E.C.

Honorary editors

Guido Belforte

Kazy Yamafuji

Editor: Andrea Manuello Bertetto

General Secretariat: Elvio Bonisoli

Atlas Akhmetzyanov
*V.A.Trapeznikov Institute of Control Sciences
of Russian Academy of Sciences
Moscow – Russia*

Domenico Appendino
*Prima Industrie
Torino – Italy*

Kenji Araki
*Saitama University
Shimo Okubo, Urawa
Saitama – Japan*

Guido Belforte
*Technical University – Politecnico di Torino
Torino – Italy*

Bruno A. Boley
*Columbia University,
New York – USA*

Marco Ceccarelli
*LARM at DIMSAT
University of Cassino
Cassino – Italy*

Amalia Ercoli Finzi
*Technical University – Politecnico di Milano
Milano – Italy*

Carlo Ferraresi
*Technical University – Politecnico di Torino
Torino – Italy*

Anindya Ghoshal
*Arizona State University
Tempe – Arizona – USA*

Nunziatino Gualtieri
*Space System Group
Alenia Spazio
Torino – Italy*

Alexandre Ivanov
*Technical University – Politecnico di Torino
Torino – Italy*

Giovanni Jacazio
*Technical University – Politecnico di Torino
Torino – Italy*

Takashi Kawamura
*Shinshu University
Nagano – Japan*

Kin Huat Low
*School of Mechanical and Aerospace Engineering
Nanyang Technological University
Singapore*

Andrea Manuello Bertetto
*University of Cagliari
Cagliari – Italy*

Stamos Papastergiou
*Jet Joint Undertaking
Abingdon – United Kingdom*

Mihailo Ristic
*Imperial College
London – United Kingdom*

János Somló
*Technical University of Budapest
Budapest – Hungary*

Jozef Suchy
*Faculty of Natural Science
Banska Bystrica – Slovakia*

Federico Thomas
*Instituto de Robótica e Informática Industrial
(CSIC-UPC)
Barcelona – Espana*

Lubomir Uher
*Institute of Control Theory and Robotics
Bratislava – Slovakia*

Furio Vatta
*Technical University – Politecnico di Torino
Torino – Italy*

Vladimir Viktorov
*Technical University – Politecnico di Torino
Torino – Italy*

Kazy Yamafuji
*University of Electro-Communications
Tokyo – Japan*

*Official Torino Italy Court Registration
n.5390, 5th May 2000*

*Deposito presso il Tribunale di Torino
numero 5390 del 5 maggio 2000*

Direttore responsabile:

Andrea Manuello Bertetto

International Journal of Mechanics and Control

Editor: Andrea Manuello Bertetto

**Honorary editors: Guido Belforte
Kazy Yamafuji**

General Secretariat: Elvio Bonisoli

The Journal is addressed to scientists and engineers who work in the fields of mechanics (mechanics, machines, systems, control, structures). It is edited in Turin (Northern Italy) by Levrotto&Bella Co., with an international board of editors. It will have not advertising.

Turin has a great and long tradition in mechanics and automation of mechanical systems. The journal would will to satisfy the needs of young research workers of having their work published on a qualified paper in a short time, and of the public need to read the results of researches as fast as possible.

Interested parties will be University Departments, Private or Public Research Centres, Innovative Industries.

Aims and scope

The *International Journal of Mechanics and Control* publishes as rapidly as possible manuscripts of high standards. It aims at providing a fast means of exchange of ideas among workers in Mechanics, at offering an effective method of bringing new results quickly to the public and at establishing an informal vehicle for the discussion of ideas that may still in the formative stages.

Language: English

International Journal of Mechanics and Control will publish both scientific and applied contributions. The scope of the journal includes theoretical and computational methods, their applications and experimental procedures used to validate the theoretical foundations. The research reported in the journal will address the issues of new formulations, solution, algorithms, computational efficiency, analytical and computational kinematics synthesis, system dynamics, structures, flexibility effects, control, optimisation, real-time simulation, reliability and durability. Fields such as vehicle dynamics, aerospace technology, robotics and mechatronics, machine dynamics, crashworthiness, biomechanics, computer graphics, or system identification are also covered by the journal.

Please address contributions to

Prof. Guido Belforte
Prof. Andrea Manuello Bertetto
PhD Eng. Elvio Bonisoli

*Dept. of Mechanics
Technical University - Politecnico di Torino
C.so Duca degli Abruzzi, 24.
10129 - Torino - Italy - E.C.*

www.jomac.it
e_mail: jomac@polito.it

Subscription information

Subscription order must be sent to the publisher:

*Libreria Editrice Universitaria
Levrotto&Bella
C.so Luigi Einaudi 57/c – 10129 Torino – Italy*

www.levrotto-bella.net
e_mail: info@levrotto-bella.net
ph.: +39 011 4275423
mob.: +39 328 5369063
fax: +39 011 4275425

PERSPECTIVES IN THE MECHANIZATION OF SAFFRON (CROCUS SATIVUS L.)

Filippo Gambella* Francesco Paschino* Andrea Manuello Bertetto**

* University of Sassari, Dipartimento di Agraria, Viale Italia 39, 07100 Sassari

** University of Cagliari, Dipartimento di Ingegneria Meccanica, Piazza d'Armi, 09123 Cagliari, Italy

ABSTRACT

In last decades it can be seen a strong growth of the biologic sector and, in UE and USA, in last years about 15-20 millions of Euro is the market value. The Sardinian Saffron spice DOP is certainly a biologic product. The saffron spice production is actually marginal because of high cost of the production phases, overall the harvesting phase of the flower on field, that is completely made by hand. The saffron harvesting mechanization is a winning chance also under a socio-economic point of view. In the production process of Saffron spice, flower harvesting and stigma separation are the most challenging phases of the entire process. In this paper, mechanical devices for supporting the human work in both these phases are presented and described. Results from field tests are provided as well. For the separation of saffron stigmas, an air separator was designed and realized. The air separator can be set with different geometric configurations to optimize separation efficiency. Results from several tests are given throughout the paper.

Keywords: saffron, hand harvest, hand separation, hand harvest, stigmas air separation.

1 INTRODUCTION

Starting from 2000 it can be seen a strong growth of the biologic sector. In UE and USA in last years about 15-20 millions of Euro is the market value. Actually Italy is one of the most "biologic" countries having about 50000 biologic farms compared to 150000 in UE; in Italy 1,5 million of hectares are worked biologically respect to 4,5 millions in UE (www.coldiretti.it). In Italy there is about the 30% of the UE biologic farms and the 25% of the worked surface. The sardinian saffron spice DOP [1] is certainly a biologic product and it is present in the 8% of the condiments. The harvest of flowers and the separation of stigmas makes the development of mechanical devices for picking the flowers and separated the stigmas as a necessity. At present, the production of flowers and stigmas without mechanization remains strongly limited to a marginal role, which does not lead to an increase in the economic importance of the product (spice). *Crocus Sativus L.* flowers must be harvested in the early hours of the day and only during a period 15 to 20 day in November.

The number of flowers per hectare ranged from 1.200.000 to 1.600.000. Sardinia has the national supremacy of the cultivated surface of saffron about 70% and of its production 80% and today the harvest of flowers and separation of stigmas still absorbs 55% to 66% of total work time because they are done exclusively by hand (Table I).

Table I – Repartition of the saffron cultivated surface (in hectares) in different Regions of Italy (ERSAT)

Italy Regions	Cultivated area (Ha)	Percentage on total of cultivated area (%)
Sardinia	35	66,8
Abruzzo	10	19,0
Tuscany	6	11,5
Umbria	1	1,9
Emilia Romagna	0,2	0,4
Liguria	0,2	0,4

Contact author: Gambella F.¹, Manuello Bertetto A.²

¹E-mail: gambella@uniss.it

²E-mail: andrea.manuello@unica.it

This work is generally laborious because flowers are structurally delicate and small. The harvest and mechanized processing of saffron flower is an important factor because gives farmers an economic opportunity. Some innovative prototypes have been proposed for picking different types of flowers [2]; [3]; [4]. In the case of saffron flowers (*Crocus Sativus L.*), the value of the powder extracted from its stamens makes the development of mechanical devices for picking the flowers and separated the stigmas a necessity.

2 MECHANIZATION OF SAFFRON CULTIVATION

2.1 TRADITIONAL CULTIVATION

The cultivation of saffron is certainly susceptible to sustain a satisfactory degree of mechanization, in most of crop cultivation normally are carried out in order to conduct the productive cycle. More studies and experiments are in progress [5]; [6]; [7]; [8]; to identify systems that would lead to partial or full implementation with the use of means technically advanced able to provide significant levels of work/capacity without compromising the quality of the final product. Normally, for the cultivation of saffron (Table II), the following operations in field in chronological order are need: soil preparation, plowing, chemical or organic fertilization, weeding, transplanting, weeding and ridging, weeding and harvesting flowers, drying, harvest and selection of bulbs for transplanting the following year.

Table II – Possibilities of mechanization to the farming operations for the cultivation/production of saffron (Source ERSAT).

Field operation	Locations of the operations	vehicle currently employed	Possibility of mechanization field operation
Surface tillage	in field	Animal/tract or	tillage, surface tiller
Fertilization	in field	by hand	Manure or fertilizer broadcaster sprayer
Wedding	in field	by hand	sprayer
Transplant	in field	by hand	transplanter
weeding e earthing-up	in field	animal	Disk weeder, tamping
Flowers harvest	in field	by hand	Hand picking/mechanical picking
stripping	farming	by hand	Air separation after flowers cutting
driyng	farming	Sun or drying	dryers
Harvest of the bulbs from field	in field	by hand	Universal harvester
Bulbs selection	farming	by hand	Rotary sorter

2.2 AIM OF THE WORK

The aim of the work was to compare the mechanical harvesting of saffron and, an air flow stigmas separation system with hand operation (harvest and stripping) conducted on field. Also, the study was set up to analyze all the phases that make up the operations of harvest and separation of the stigmas to the flower, through the detection and analysis of different parameters for the determination of the working capacity of the yard and of the individual worker.

3 MATERIALS AND METHOD

3.1 FLOWERS HARVEST IN FIELD

The experimental field on which were conducted our tests had on average a surface area of 1000m² and the study was set up to analyze all the phases that make up the operations of harvest (figure 1) and separation stigmas from the flower, through the analysis of different parameters for the determination of the working capacity of the individual worker.



Figure 1 Hand harvest of saffron flowers.

In particular have been found: the surface of cultivation, the number of workers, the numbers of harvest and separated flowers per hour, the effective and the total time for managing the total operation in field and in the factory. For the latter, we have used the effective time and total time for evaluate the difference between the mere execution of the separation of stigma and accessories that are all the speeches outline is complete. The working times total and individual were detected with the aid of a digital video camera appropriately prepared.

The separation of the flower stigmas was made by seven workers, each of which handled a number of flowers variable as a function of the time. Even in this case has been made of the recovery of all stages with a digital video

camera which has been supported by a parallel detection with the aid of a chronometer.

The mechanical harvesting was performed using the prototype proposed by Bertetto et al.(2011), with two main tasks, detaching the corolla from the stem and collecting the flower.

About the separation, Gambella *et al.* (2009) developing a controlled multi flow cyclone will process the harvested flowers to separate the stigmas from stem, petals and foils after the detachment/cutting of the flowers.

3.2 CHARACTERISTICS OF THE AIR FLOW SYSTEM TYPE 1, TYPE 2 AND TYPE 3

The separation of the stigmas was tested in 3 air flow systems. All the tests were carried out with a constant air speed of 3m/s. In the type 1 air flow system, the diameter of the duct was 30 cm and shaped like a plastic and transparent PVC tube with smooth walls to a height of 120 cm. In the type 2 system, the duct was divided into three sections with a constant diameter of 35 cm.

The first section (40 cm height) was made by metal while the two remaining sections on top of the first one (80 cm height) were made by a high resistant pyrex glass with smooth walls. In the type 3 system, the pyrex glass was replaced by three cones of grained metal with decreasing diameter, the duct diameter decreased from 40 cm to 13 cm and the height was 120 cm as type 1 and 2.

All three systems were powered by a small electric coaxial fan (2.2 kW) regulated by an inverter (e.p. 0.75 kW). After the flowers have been hand cut, the separation of stigmas was obtained by these three different air systems with a constant air speed (3 m/s), and with the diameter of the duct variable in the three different systems.

The air speed was measured with an anemometer (DO 2003, HVACRI, Salmoiraghi, Inc). The separation tests, for each type of cyclone used, were carried out on 630 flowers (210 flowers for each type of air system and 70 flowers for each replicate test).

3.3 FLOWER DIMENSION PARAMETERS.

Three hundred flowers were harvested in two different fields, 50 per site, located in San Gavino Monreale (Central Sardinia - Italy) and a hundred stigmas per site were separated and weighed. Flower statistical dimension parameters were determined with three replicates of 50 flowers, for each site. The longitudinal (L_d), transversal (T_d) and intermediate (W_d) diameters were measured by an electronic caliper model S 225 (Wurth), with a resolution of ± 0.001 mm. The average geometrical diameter (D_g) of the three parts of the flower was calculated using the Mohsenin (1970) formula (1):

$$D_g = (L_d \cdot W_d \cdot T_d)^{1/3} \quad (1)$$

3.4 STATISTICAL ANALYSIS

The weight of 100 stigmas was statistically analyzed with Minitab 16 software by simple analysis of variance (ANOVA) and the means were separated using the Tukey test at a 95% confidence interval. The separation efficiency expressed as a percentage (ES %) was calculated by the ratio of the number of stigmas, obtained with three filaments, divided by the number of broken stigmas (with one or two filaments). All the separation data were statistically analyzed with the Minitab 16 software by simple analysis of variance (ANOVA) and the means were separated using the Tukey test at a 95% confidence interval.

4 RESULTS AND DISCUSSION

4.1 IN FIELD HARVESTING TESTS

The device was tested in the field and the flowers were regularly placed along with rows.

The distance between two successive plants was about 10 cm while the distance between the rows was about 20 cm. The number of flowers was of about 1500000/ha (600000/acre).

It can be noted that each plant can produce more than a flower. Most of the flowers had bloomed for a few days (10 days) with a height of approximately 15 cm, a few flowers were only partially opened or even not opened yet and their height was about 5 cm.

For testing, the mechanism was mounted at the end of a hollow tube. The cam motion was controlled by an open loop position controller and the motor was supplied by a 6V power battery pack. To have a cam rotation during the cutting process the user rotates a control knob placed on a box mounted onto the hollow tube.

The cutting procedure consists of placing the device under the flower to locate the stem in the space between cam and striker (figure 2).

Once positioned, the cam was operated, forcing the flower to execute the kinematics required. During cutting, the device was held stationary. The flowers harvested had a mass variation of about 10% with an average value of 0.5 grams.

The size variation was higher, 20% to 25%, depending on the growing phase of the flower. Table III shows test results in terms of efficiency defined as number of flowers picked successfully against the number of trials with assigned time.

The analysed data refer to the number of successes in terms of picked flowers with respect to the number of semi-oscillations required.

The data obtained reveal 35% of successes in the tests with 2 cam semi-oscillations, 31% with 3 cam semi-oscillations, 16% with 1 cam semi-oscillation and 18% with a number of cam semi-oscillations larger than 3.



Figure 2 Steps of the cutting process in the tests on the saffron flower field: (a) flower location, (b) approach, (c) oscillating and cutting.

Table III – Number of flowers harvested based on the number of semi-movements in each test

Number of semi-oscillations Base Time (tb)	1 (t/tb) ⁻¹	2 (t/tb) ⁻¹	3 (t/tb) ⁻¹	≥4 (t/tb) ⁻¹
0.5 s	19c	44a	34ab	23bc
0.75 s	24b	47a	31ab	18b
1.0 s	15b	36a	46a	23b
Total	58	127	111	64
% of total flowers (360) picked	16	35	31	18

*Numbers not followed by a letter are significantly different ($p \leq 0.005$)

4.2 DIMENSIONAL PARAMETERS OF THE SAFFRON FLOWERS

The flowers analysed in the two experimental fields (A and B) showed differences for the sites and between the parts - petals, anthers and stigmas. As concerns the average geometrical diameter (Dg) of the three parts, it varied from 18.36 mm to 21.00 mm for the petals; from 4.04 mm to 4.98 mm for the anthers and from 2.66 mm to 4.84 mm in fields A and B respectively. The weight of the stigmas varied from 0.01 g in field B and 0.05g in field A. For the stigmas, the statistical analysis (Table IV) showed significant differences ($p \leq 0.05$) between sites.

Table IV – Comparison of weight of stigmas harvested on the same date in two different experimental fields.

Field	Stigmas weighed (n°)	Average weight of 100 stigmas (g)
A	100	0.014 b \pm 0.01
B	100	0.045 a* \pm 0.01

*Numbers not followed by a letter are significantly different ($p \leq 0.005$)

5 WORK TIME AND WORKERS CAPACITY

5.1 RESULTS OF HAND HARVEST

The time of hand-picked flowers in the field was 2.8 h for an area of 1000 m². The farmer, exploiting the short distance between the rows, approximately 30 cm, harvested

simultaneously in two rows the flowers present, running a double surface and increasing the working capacity as a function of the length of the rows (100 m each). Since detection is found that the harvest time of each row was not homogeneous because strongly influenced by the different number of flowers present. Therefore, the ability to work related to the covered area was 375 m²/h. In fact, given the very flowering scale forcing the farmer to frequently change its attitude losing the continuity that has had a profound impact on its performance. The flowers harvested were stored in small containers and then to harvest finished, transfer the premises in which they were stripped.

5.2 SEPARATION OF STIGMAS FROM THE REST OF FLOWER

It is one of the most traditional procedures that remain the same throughout the centuries. The separation by hand in Sardinia, traditionally, two methods are used for stigma separation: a) the flower is opened with both hands and the column is cut directly at the bottom of the three stigmas, very carefully, in order not to separate the stigmas. Finally, the white part of the column is removed; b) while the flower is still closed the column is removed with the fingernail or a scissor, while the other hand holds the stigmas. The work times of this operation (a) were measured on an ongoing basis for each phase and examined the values obtained from the average of three replicates for each worker. Whereas individually the work carried out by two workers, who worked with the same flowers and at the same time, is observed (Table V) that the former has used 10% less than the actual time for each flower (7.9 sec.) Compared per second (8.6 sec.), but the second, although a small difference, it has lost a total less time with 16.9 seconds compared to 17.1 seconds of the first worker. Observing the time of separation of stigmas for single flower (figure 3) and of the same workers, even after the two replicates, these do not change substantially and are between 6 and 16 seconds in the first and between 3 and 13 seconds in the second. Ultimately, in the first test the same worker has stripped the 15% of the flowers with times ranging between 1 and 6 seconds, 41% with times between 6 and 11 seconds, 15% between 11 and 16 seconds and 8% between 16 and 23 seconds.

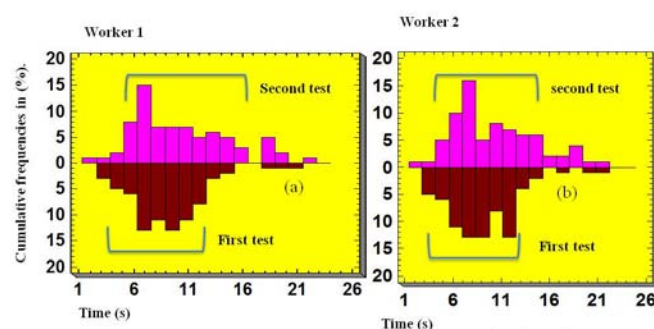


Figure 3 Cumulative frequency of 100 flowers stripping in two replicates obtained from two skilled workers.

Table V – Mean values of the time, effective and total work capacity of two workers by hand

Workers	Effective time	Total time	Total Capacity	
	s/flower ± std dev	s/flower ± std dev	flowers/h	g/h*
1	7,9 ± 1,5	17,1 ± 3,8	217 461*	1,07 2,27*
2	8,6 ± 1,4	16,9 ± 1,8	213 430*	0,84 1,70*

*fresh stigmas

Table VI – Number of flowers separated per minute (flowers /min) using three different air separation systems.

Air system (type)	Test (n°)	Flowers separated (flowers/ min.)	Separation efficiency (%)	Quality of stigmas n° filaments		
				Three (%)	Two (%)	One (%)
1	7	34a*	49%	49	28	23
2	7	19b	27%	27	55	18
3	7	15b	22%	22	65	13

*Numbers not followed by a letter are significantly different ($p \leq 0.005$)

In the second test, the same employee, gets a total time of husking best: 14% of the flowers will have been cleansed from 1 to 6 seconds, 50% between 6 and 11 seconds, 13% between 11 and 16 and 3 % between 16 and 23 seconds. In detail, the frequencies of the times the first agent has washed away 60% of the flowers in a time ranging between 6 and 16 seconds in the first test, while in the second oscillates between 6 and 12 seconds. This variability is mainly due to the breaks that the employee is granted as a result of his physical exhaustion or even for their own physiological necessity. In fact, it happens that with the progress of the workers progressively increase the time of husking and accordingly reduce the ability to work. This would not happen if it was a brief period of rest, even a few minutes, so that their business suffers the most from the effort. Obviously this is permissible when the period of husking not exceed a total of three hours, should it be extended, and that in the current situation seldom occurs, the average working time, refers to a single flower, would increase. The mean total work capacity, calculated by taking the number of flowers separately by two workers, amounted to 217 flowers/h for the first worker and 213 flowers/h for the second when referring to the total time. If you are referring to the same values to the actual time, these are doubled reaching, respectively, 461 flowers/h and 430 flowers/h. Referring to the amount of spice obtained in the

tests carried out and considering the total working time, the capacity of the first worker was 1.07 g/h against 0.80 g/h of the second. So for every gram of spice were needed from 203 to 253 flowers (Table VII).

5.3 RESULTS OF AIRFLOW SEPARATION

The separation of the various components takes place in conditions of constant increasing speed up to 3.0 m/sec (Table VI) beyond which the air speed determines the expulsion of stigmas as well. The operating cyclone capacity ranges from 15 flowers/min. (type 3) to 34 flowers/min (type 1) with stigmas of weight equal to 0.05g and from 41 flowers/min (type 3) to 50 flowers/min (type 1) with stigmas of weight equal to 0.01g (Table VI).

In both air separation systems, the anthers and petals of the saffron flowers were not completely expelled from the duct, and only in type 1, the saffron of stigmas showed the breaking of one or two filaments because of collisions with the duct borders for 49% (Table VI). Ruptures of the stigmas were high, from 28% to 65% (two filaments) and from 13% to 23% (one filament), and filament breakage determined the formation of a compact mass of floral product. Separation efficiency ranged from 22% in the system three to 49% in the system one. For the stigmas with weight equal to 0.01g (Table 5), the separation efficiency increased from 59% in the system three to 71% in the system one.

The anthers and petals of the saffron flowers were not completely expelled from the duct, and the stigmas remained inside the separation duct floating to a height of about 30 cm at the separation surface.

The damage observed on stigmas (Table VII) was relatively low, and therefore the quality of stigmas ranged from 24% to 27% and 35% in the case of two filaments and from 5% to 13% and 6% with a single filament.

Table VII – Number of flowers separated per minute (flowers/min) using three different air separation systems.

Air system (type)	Test (n°)	Flowers separated (flowers/ min.)	Separation efficiency (%)	Quality of stigmas n° filaments		
				Three (%)	Two (%)	One (%)
1	7	50a	71	71	24	5
2	7	42ab	60	60	27	13
3	7	41b	59	59	35	6

*Numbers not followed by a letter are significantly different ($p \leq 0.005$)

This air system (type 1) did not cause the formation of a compact mass of floral product formed by stigmas, anthers and petals inside the duct.

The vibrations transmitted through the fan to the surface on which the disjointed flowers were placed did not produce any accumulation of anthers and petals on the borders of the duct. The mean total work capacity, calculated by taking the number of flowers separately by cyclone type 3 in two replicates test, amounted to 1714 flowers/h for the first test and 1895 flowers/h for the second when referring to the total time.

If you are referring to the same values to the actual time, these are doubled reaching, respectively, 2250 flowers/h and 2571 flowers/h.

Referring to the amount of spice obtained in the tests carried out and considering the total working time, the capacity of the cyclone in the first test was 8.45 g/h against 7.49 g/h of the second test.

If you are referring to the same values of g/h to the effective time, these are doubled reaching, respectively, 11.12 g/h and 10.16 g/h (Table VII).

Table VII – Mean values of the time, effective and total work capacity with cyclone type 3

Air system type 3	Effective Time (ET)	Operational Time (OT)	Cyclone Work Capacity type 3	
			flowers/h	g/h
test	sec/flower	sec/flower	flowers/h	g/h
1	1,6	2,1	1714* 2250**	8,45* 11,12**
2	1,4	1,9	1895* 2571**	7,49* 10,16**

*Related to Operational Time (OT) (3600 sec/2.1sec)

**Related to Effective Time (ET) (3600sec/1.6)

4. CONCLUSIONS

The harvesting device described is based on an operating principle quite different from the method used for the manual harvesting of *Crocus Sativus L.* flowers. The principle proposed has been easily mechanized in a cam-striker mechanism. The device is an electric semi-automatic machine light enough to be a portable harvester. The cam's motor is supplied by a portable battery easy to use in field. As a result of tests, the device and the equipment appear to be suitable for mechanical harvesting and since almost 82% of the flowers were successfully picked in the field with an adequate number of cam's semi-oscillations up to 3.

The use of an air flow system, increased work capacity per worker from 430-461 flowers/h in the traditional method, to 2640-3360 flowers/h with the experimental prototype. The grams of fresh stigmas obtained ranged from 0.84 to 2.27 g/h in the traditional separation, versus the 48 g/h 132 g/h with the experimental prototype. Saffron quality is considered high when all stigmas are joined (three filaments). Two of the three separation systems produced damage to the filaments of stigmas up to 65% in the stigmas with weight equal to 0.05g and for these flowers

separation efficiency was lower (49%) than for the stigmas with weight of 0.01g (71%). For the operating conditions utilized the type 1 air system separator turned out to be the most suitable for the mechanical separation of stigmas with weight equal to 0.01g. For the other stigmas it was necessary to perform in the operating condition of separation (air speed) to reduce the number of stigmas with two filaments and increase separation efficiency. The use of a duct surface different from PVC or glass increased damage to the stigmas because the collision with the wall of the duct reduced the quality of the separated stigmas.

ACKNOWLEDGEMENTS

The research activity presented in this paper was supported by Provincia del Medio Campidano (Sardinia – Italy).

REFERENCES

- [1] European Council Regulation EEC No. 2081/92 of 14 July 1992 on the Protection of Geographical Indications and Designations of Origin for Agricultural Products and Foodstuffs.
- [2] Paschino F., Gambella F., First contribution to the mechanization string of saffron flowers (*Crocus Sativus L.*), *Innovation Technology to Empower Safety, Health and Welfare in Agriculture and Agro-food Systems*, Sept.15-17, 2008 Ragusa – Italy.
- [3] Erriu N., Manuello Bertetto A. and Ruggiu M., A two finger device for saffron flower harvesting, *Applied Mathematics and Mechanics series*, Acta Technica Napocensis, 49(2), 2006, pp. 45-50.
- [4] Ruggiu, M. and Manuello Bertetto, A. A mechanical device for harvesting *Crocus Sativus* (Saffron) flowers, *Applied Engineering in Agriculture, American Society of Agricultural and Biological Engineers (ASABE)*, Vol. 22 (4), 2006, pp 491-498.
- [5] Gambella F, Paschino F., Manuello Bertetto A. and Ruggiu M., A mechanical system to harvest the *Crocus Sativus* flowers and to separate stigmas, In: XXXIII CIOSTA - CIGR V Conference 2009, Reggio Calabria (Italy) "Technology and management to ensure sustainable agriculture, agro-systems, forestry and safety", vol. 1, pp. 719-723.
- [6] Manuello Bertetto, A., Falchi, C., Pinna, R. and Ricciu, R., An integrated device for saffron flowers detaching and harvesting. In: Proc. RAAD 11 - 20th International Workshop on Robotics in Alpe Adria Danube Region, Brno, Czech Republic, 2011.
- [7] Reed S.D., Armstrong P.R., Bruswitz G.H., Stone M. L., Resistance of marigold flowers to air flow. Transaction of ASAE, 2001, Vol. 44; pp. 639-642.
- [8] Gambella F., Paschino F., Manuello Bertetto A. and Ruggiu M., Application of mechanical device and air flow systems in the harvest and separation of saffron flowers (*Crocus Sativus L.*). Transactions of the ASABE. 56(4), 2013, pp. 1259-1265.

A STUDY OF FATIGUE IN HIGH SPEED GEARS

Francesca Curà*

Fabio Gallo*

Carlo Rosso*

*Department of Mechanical and Aerospace Engineering, Politecnico di Torino,
Corso Duca degli Abruzzi 24, 10129, Torino

ABSTRACT

This paper presents a study about a multiaxial fatigue approach in high speed gears. Once identified the main effects determining a variable stress state at the tooth root fillet, it has been developed a methodology for the superposition of mesh load, centrifugal field and dynamic behaviour of the gear. To this aim, a numerical model has been accomplished to simulate each loading condition independently. FEM analyses, in specific, have provided meaningful results about the time history of the stress tensors at the tooth root fillet. A comparative study has been included, which shows the rim thickness effect on the dynamic load variation. In addition, this paper warns the reader about the usage of standards for gears with low backup ratio.

Keywords: multiaxial fatigue, rim thickness, dynamic overloads, gears

1 INTRODUCTION

Nowadays, planetary gearings are massively exploited in the aerospace field thanks to their robustness and to a very good weight/power ratio. However, this field of application is characterized by two antithetical needs: on one hand high velocities and torques, on the other the lightening of the components. These features affect both design and manufacturing process of the aerospace gearings by leading to a very low rim thickness factor. Due to this “non-traditional geometry”, it is straightforward the importance of a deep and accurate study about the fatigue behaviour of the components.

One of the main concerns of gear transmission designer is the reduction of the dynamic overloads. The research on gear noise and vibrations has revealed that even if the input torque and speed are constant, significant vibration of the gear masses can exist. Beside the thermal deformations due to friction, indeed, the velocity influences the magnitude of the dynamic loads through the unavoidable errors characterizing the mounting and the manufacturing processes [1].

Therefore, harsh dynamic tooth forces result from the relative vibration of gears as they vibrate in response to an excitation known as “transmission error” [2,3]. Ideally, a gear set would have a uniform velocity ratio between input and output rotation.

Hence, the transmission error can be defined as the departure from the uniform relative angular motion of the pair of actual meshing gears. A further source of vibration is represented by the meshing stiffness variation [4].

Therefore, this present study is aimed to develop a methodology able to account for all the main effects enforcing a multiaxial fatigue state on the gears: in the first section of the paper it has been provided the reader a general overview about the principal fatigue failure criteria. In specific, since it has been talking about aerospace gearings, the research has been limited to the *stress-based models*, suitable for large class of components that must operate near or below the fatigue threshold [5]. Thus, having chosen the proper tools for the fatigue life assessment, the authors resorted to the FEM analysis in order to investigate the stress state characterizing the tooth root fillets of a reference gear model. By superimposing the mesh load and the centrifugal field it has been possible to rebuild the “static” time evolution of all the stress tensor components over a single revolution period of the gear. Then, the report goes through the core of the research by investigating the extent of the dynamic overloads. After being questioned about the applicability of the standards (AGMA, ISO) [6,7], for the computation of the dynamic factors K_v , a FEA approach has been adopted for the dynamic characterization of two gear models with different backup ratio (m_b , rim thickness/tooth height).

The final section of the present research work clarifies the theory underlying the methodology for the effect superposition and provides a practical example on a thin

Contact author: Francesca Curà¹

¹Corso Duca degli Abruzzi, 24 – 10129 Torino (Italy)
E-mail: francesca.cura@polito.it

rim gear. This way the reader is allowed to recognize the importance of the dynamics in terms of critical stress magnitude and its localization.

2 FATIGUE FAILURE CRITERIONS

2.1 OVERVIEW

In many applications, the mechanical components undergo multiaxial fatigue. This stress state occurs when at least two principal stresses are different from zero.

One of the main problems concerning multiaxial fatigue is that each of the principal stresses is characterized by its own time history. Hence, generally speaking, we can distinguish between three different cases:

- *Simple multiaxial stress states*: all the principal stresses achieve their maximum and minimum values at the same time; In addition, principal directions do not change over time;
- *Complex multiaxial stress states*: the stress sources operate out of phase with each other, so the principal directions change over time;
- *Intermediate case*: the stress sources are in phase with each other but the principal directions are not fixed, due to the presence of mean stresses whose principal directions do not coincide with the ones belonging to the alternate components.

The gearboxes are designed so to operate near or below the fatigue threshold. Therefore, what the reader is going to see next is an overview on the main multiaxial fatigue failure criteria developed on the so-called stress-base models [5]. All of them are characterized by the following general form:

$$\Delta\tau + k\sigma \quad (1)$$

Where $\Delta\tau$ is the shear stress, σ is the normal stress, k is a constant parameter.

Hence, the models under investigation will differ in the interpretation of shear and tensile stress terms.

2.2 MANSON-MCKNIGHT

The Manson-McKnight criterion [8] is based on Von Mises hypothesis and is aimed to reduce the multiaxial stress state to an equivalent monoaxial stress. Thus, by assuming the following characteristic parameters

$$\Delta\sigma_i = \sigma_{i,max}, -\sigma_{i,min} \quad (2)$$

$$\delta\sigma_i = \sigma_{i,max}, +\sigma_{i,min} \quad (3)$$

$$\Delta\tau_i = \tau_{i,max}, -\tau_{i,min} \quad (4)$$

$$\delta\tau_i = \tau_{i,max}, +\tau_{i,min} \quad (5)$$

it is possible to define the corresponding equations, as representative of the monoaxial mean component σ_m and the monoaxial alternate σ_a :

$$\sigma_a = \frac{1}{2\sqrt{2}} \sqrt{(\Delta\sigma_x - \Delta\sigma_y)^2 + (\Delta\sigma_y - \Delta\sigma_z)^2 + (\Delta\sigma_z - \Delta\sigma_x)^2 + 6(\Delta\tau_{xy}^2 + \Delta\tau_{xz}^2 + \Delta\tau_{yz}^2)} \quad (6)$$

$$\sigma_m = \frac{1}{2\sqrt{2}} B \sqrt{(\delta\sigma_x - \delta\sigma_y)^2 + (\delta\sigma_y - \delta\sigma_z)^2 + (\delta\sigma_z - \delta\sigma_x)^2 + 6(\delta\tau_{xy}^2 + \delta\tau_{xz}^2 + \delta\tau_{yz}^2)} \quad (7)$$

$$B = \frac{\sum \sigma_1 + \sum \sigma_3}{\sum \sigma_1 - \sum \sigma_3}, \text{ where } \sigma_3 < \sigma_2 < \sigma_1.$$

As we can notice from the equation (7), the sign and the magnitude of the mean stress are dependent on the factor B , itself related to the principal stresses, σ_1 and σ_3 , through the following expressions:

$$\begin{aligned} \sum \sigma_1 &= \sigma_{1,max} + \sigma_{1,min} \\ \sum \sigma_3 &= \sigma_{3,max} + \sigma_{3,min} \end{aligned} \quad (8)$$

2.3 SINES

After studying several failure criteria, Sines defined the octahedral shear stress as the critical parameter for the assessment of the fatigue damage and he concluded that the mean hydrostatic stress during a cycle has an effect on fatigue life [9]. In the same way as the octahedral stress represents an ‘‘average’’ shear value for a state of stress, the hydrostatic stress, σ_h can be considered as representing the average tensile stress in the material. Physically, it is the normal stress on the octahedral shear plane and it is related to the mean bending stress, σ_b through the following formula:

$$\sigma_h = \frac{\sigma_b}{3} \quad (10)$$

On the basis of these considerations, the author developed the analytical expression of the model:

$$\frac{1}{\sqrt{2}} \sqrt{(\sigma_{a,1} - \sigma_{a,2})^2 + (\sigma_{a,3} - \sigma_{a,2})^2 + (\sigma_{a,1} - \sigma_{a,3})^2} + m(\sigma_{m,1} + \sigma_{m,2} + \sigma_{m,3}) \leq \sigma_{D-1} \quad (11)$$

Where $\sigma_{a,i}$ is the principal stress amplitude, $\sigma_{m,i}$ is the principal mean stresses, σ_{D-1} is the monoaxial endurance limit, m is a coefficient accounting for the properties of the materials and it can be computed as far as the equation (11) still holds for the particular case of monoaxial loading. Thus, by setting the principal stress amplitudes $\sigma_{a,2}$, $\sigma_{a,3}$ and the principal mean stresses $\sigma_{m,2}$, $\sigma_{m,3}$ equal to zero, we get:

$$\sigma_{a,1} + m\sigma_{m,1} = \sigma_{D-1} \quad (12)$$

The equation (12) is just the Goodman condition:

$$m = \frac{\sigma_{D-1}}{\sigma_{UTS}} \quad (13)$$

where σ_{UTS} represents the ultimate tensile strength.

However, octahedral stresses can be obtained from direct computation using the six stress components for any coordinate system. In particular, for a generic non-principal reference frame, the equivalent stress amplitude becomes:

$$\sigma_{a,eq} = \frac{1}{\sqrt{2}} \sqrt{(\sigma_{a,x} - \sigma_{a,y})^2 + (\sigma_{a,z} - \sigma_{a,y})^2 + (\sigma_{a,x} - \sigma_{a,z})^2 + 6(\tau_{a,xy}^2 + \tau_{a,xz}^2 + \tau_{a,yz}^2)} \quad (14)$$

The equivalent mean stress, proportional to the 1st invariant of the mean stress tensor instead, simply turns into:

$$\sigma_{m,eq} = \sigma_{m,x} + \sigma_{m,y} + \sigma_{m,z} \quad (15)$$

Sines' formulation has the advantage that is easily solved for complex stress states and only relatively simple tests must be done to determine the constant m . However, the application of Sines' criterion is limited to proportional loading.

2.4 FINDLEY

Findley reviewed much of the same experimental data as Sines, but came to a slightly different model [10]. He suggested that the normal stress, σ_n , on a shear plane might have a linear influence on the allowable alternating shear stress, $\frac{\Delta\tau}{2}$. Thus, the infinite life condition is represented by the equation (16)

$$\left(\frac{\Delta\tau}{2} + k\sigma_n\right) \leq f \quad (16)$$

Where k is a characteristic constant, f is the fatigue limit in fully reversed axial loading.

This model differs from Sines' or Manson-McKnight's in that it identifies the stress acting on specific planes within the material. These are termed critical planes and they can be defined as one or more planes subject to a maximum value of a characteristic *damage parameter*. Findley identifies a critical plane for fatigue crack initiation and growth that is dependent on both alternating shear stress and maximum normal stress. The combined action of these stresses is responsible for fatigue damage and failure is expected to occur on the plane where the maximum value of the quantity in parenthesis in equation (16) is detected. Moreover, the constant k is determined experimentally by performing fatigue tests involving two or more stress state. Several examples are shown in Table I.

Anyway, for ductile materials, k typically varies between 0.2 and 0.3.

2.5 MCDIARMID

McDiarmid proposed a criterion very similar to Findley criterion [11]. What is different is the definition of critical planes. McDiarmid, indeed, defined the critical plane as the plane characterized by the maximum shear amplitude and not the by the maximum damage quantity. Thus, once this plane has been identified, by adding the shear stress amplitude, $\frac{\Delta\tau_{max}}{2}$, to the normal stress, σ_{max} , on the same plane, we end up with the infinite life condition according to McDiarmid:

$$\left(\frac{\Delta\tau_{max}}{2t_{A,B}} + \frac{\sigma_{n,max}}{2\sigma_{UTS}}\right) \leq 1 \quad (17)$$

where $t_{A,B}$ represents the shear fatigue strength for two type cracking modes. Case *A* propagates cracks that grow along the free surface, whereas the Case *B* results in cracks that penetrate into the material and σ_{UTS} is the ultimate tensile strength.

By comparing this criterion with the one developed by Findley, we notice that the constant k is replaced by the quantity $\frac{\sigma_{n,max}}{2\sigma_{UTS}}$. Thus, only one set of fatigue tests and one static test are necessary, as compared to the two set of fatigue tests needed to define k .

The difference in definition of the critical plane between McDiarmid and Findley is clearly illustrated by the case of

high stress ratio $R(= \frac{\sigma_{min}}{\sigma_{max}})$, in presence of uniaxial tension. The former criterion always predicts critical planes at $\pm 45^\circ$, whereas the latter foresees critical planes approaching to 0° as R increases toward 1.

Table I - Examples of solutions for k based on the ratio of fatigue strength for two stress states

Ratio of Fatigue Strength	k
$\frac{\sigma_{a,R=-1}}{\tau_{a,R=-1}}$	$\frac{2}{1 + \frac{k}{\sqrt{1+k^2}}}$
$\frac{\sigma_{a,R=0}}{\tau_{a,R=-1}}$	$\frac{1 + \sqrt{1+k^2}}{2k + \sqrt{1+(2k)^2}}$
$\frac{\sigma_{a,R=0.5}}{\tau_{a,R=-1}}$	$\frac{1 + \sqrt{1+k^2}}{4k + \sqrt{1+(4k)^2}}$

2.6 DANG VAN

The application of Dang Van's criterion [12] requires a deep knowledge level about the stress state of the component and this reflects the complexity of the model. For this reason, the present paragraph is limited to the description of the underlying approach. In particular, the author proposed an endurance limit criterion on the concept of microstress within a critical volume of material. This model arises from the observation that fatigue crack nucleation is a local process and begins in grains that have undergone plastic deformations and form characteristic slip bands. In addition, since cracks usually nucleate in intragranular slip bands, it has been hypothesized that the microscopic shear stress on a grain must be an important parameter. In the same way, it has been reasoned that the microscopic hydrostatic stress will influence the opening of these cracks or slip bands. Finally, the simplest failure criterion involving these two variables is the linear combination, as shown in equation (18), where $\tau^{(t)}$ and $\sigma_h^{(t)}$ are respectively the instantaneous microscopic shear stress and the hydrostatic stress, and a and b are constants.

$$\tau(t) + a\sigma_h(t) = b \quad (18)$$

The microscopic stresses and strains within critical grains are different from the macroscopic stresses and strains commonly computed for fatigue analysis. Therefore, it was necessary to distinguish these two size scales as follows:

- *Macroscopic scale*, characterized by an elementary volume $V(M)$ surrounding a point where the fatigue analysis is to be performed. This size scale is of the order of a strain gage or FEM element. Macroscopic stresses are denoted $\sum(M, t)$ and strains $E(M, t)$. Both are functions of position within the structure, M , and time, t .
- *Microscopic scale*, of the order of a grain or other suitable microstructural unit corresponding to a subdivision of $V(M)$. The microscopic stresses $\sigma_{m,t}$ and strains $\varepsilon_{m,t}$ are related but not equal to macroscopic (at a microscopic scale a material is neither isotropic nor homogeneous).

3 STATIC ANALYSIS

3.1 INTRODUCTION

In the present paper, the term static is going to be used for any loading condition not inducing a dynamic response of the component under investigation. Thus, this section has been devoted to the analysis of the stress state induced by mesh and inertial load only. In order to achieve the goal, several FEM analyses have been carried on the gear model presented in the technical report on crack propagation studies by NASA [13].

3.2 BENDING EFFECT

3.2.1 Bending stresses

Since the mesh load induces a “local” stress state, it has been thought to extract a 4-teeth sector out of the reference model (Figure 1) to reduce the computational time at the solution stage.

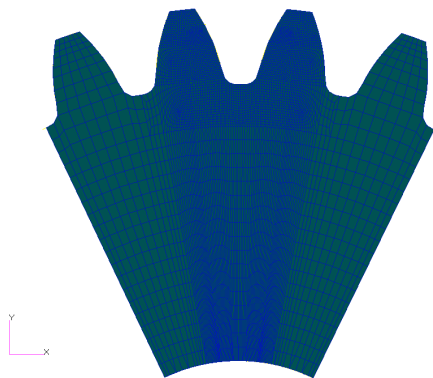


Figure 1 Mesh of the 2D model of the 4-teeth sector.

For our simulations, since the teeth 2 and 3 are the only ones undergoing the bending load (having assumed a clockwise rotation, it has been carried out the teeth numeration as shown in Figure 1), it has been made a mesh refinement in the neighbourhood of their common fillet.

By following a tooth during a complete revolution, we can define the segment AB as the portion of the line of contact along which the engagement with the mating tooth takes place. The Figure 2 specifically shows the ideal bending load history for a certain rotation angle.

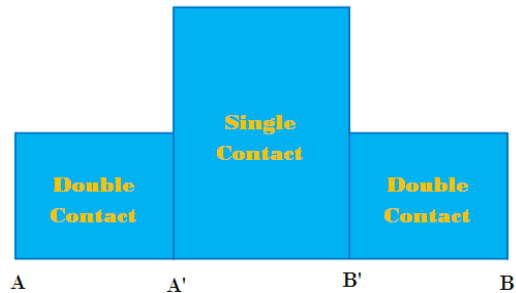


Figure 2 Ideal bending load history on a tooth, over the segment of contact AB.

Hence, since the tooth experiences the engagement over an arc of revolution, it has been thought to develop a time history of the stresses. To this aim, the engagement has been discretized into meaningful instants corresponding to the transitions of the teeth 2 and 3 on the points A, A', B', B of the contact line, and the stresses of some elements at the tooth root fillet have been detected.

The Figure 3 shows the qualitative distribution of the stresses, for some characteristic loading conditions.

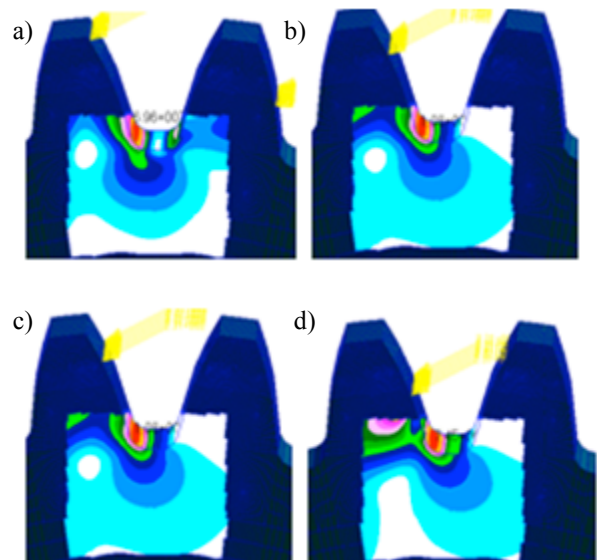


Figure 3 Engagement of the tooth 3 along the segment of contact: a) A, b) A', c) B', d) B.

Beside the graphical representation, it has been possible to quantitatively know the extent of all the components of the stress tensor evaluated in the centroid of the element under investigation. In specific each simulation, representing a

precise loading condition, allowed the rebuilding of the stress-time history over the arc of engagement. In particular, the next figure (Figure 4) is going to show the most relevant normal stresses σ_x for an element belonging to the tooth root fillet.

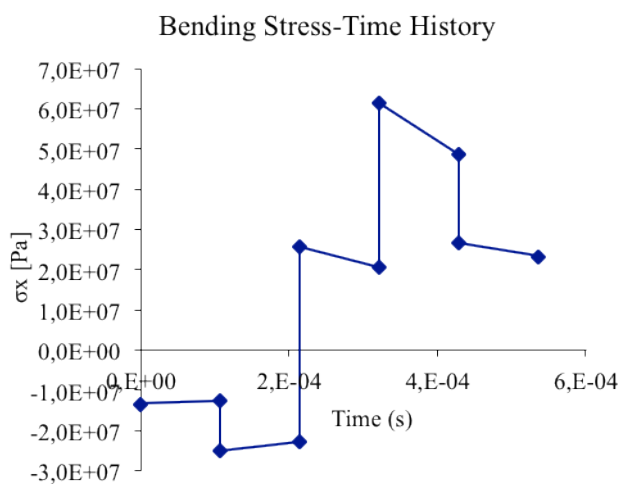


Figure 4 Bending stress time history of an element: σ_x .

The stress-time history shown in Figure 4 is qualitatively representative of all the other elements under investigation. This first result, then, seems to confirm what some gearing manuals have reported about the bare static analysis [4]. What the reader can easily observe is that the single contact condition with maximum flexural arm (situation corresponding to the point A' on the contact line) is the most critical for the element belonging to the tooth root fillet. Also all the other components of the stress tensor, indeed, assume their own maximum values as soon as the tooth 3 takes over the whole bending load. However, the static failure is something really rear to be detected in a gearing system. Another feature clearly visible in Figure 4 is that the element experiences a compression stress state (negative stress values) before the tooth 3 starts to be involved in the engagement. The clockwise rotation, indeed, leads the tooth 2 to carry the load in advance, by inducing pure compression of the fillet of interest for a time instant $t < 0,2$ ms. However, when the tooth 3 enters the first single contact segment (point A of the contact line), the stress state turns into a tensile state. Thus, at the time instant $t = 0,2$ ms, all the time histories of the tensor components are characterized by a sharp jump, up to relevant positive values.

3.3 CENTRIFUGAL EFFECT

3.3.1 Centrifugal stresses

As we already said, another feature affecting the stress state at the tooth root fillet is the centrifugal field. The literature about gears extensively talks about the velocity effect on gears as the main source of vibrations. However, the centrifugal forces themselves are proportional to the square

of the spinning speed. Thus, this paragraph will investigate the influence of the centrifugal field on the stress state induced by the mesh load only. Since the centrifugal field involves all the inertias of the gear, it has been decided to develop a 3D mesh for the complete CAD model. Thus, by keeping the reference mesh of the 4-teeth sector unchanged, the centrifugal analysis has been carried out on the whole gear model, with a coarser mesh away from the fillet. Furthermore, since it has been thought of a shrink fit coupling between the gear and the mating shaft, we decided to fix all the translations along X, Y, Z, directions (Cartesian coordinates) of all the nodes belonging to the hub interface. The processing of the above described boundary conditions leads to the following results shown by the Figure 5.

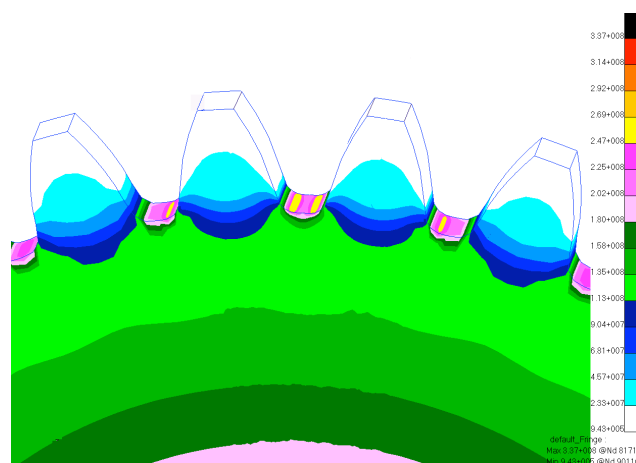


Figure 5 Stress field due to the centrifugal field.

The stresses seem to decrease along the radial direction. This first result agrees with the theory of the rotating disks [14]. In particular, it is possible to detect the most stressed area around the hub interface, since the restraints previously enforced prevent the deformation of the gear in that region. The chromatic distribution highlights a stress concentration in the neighbourhood of the tooth root fillets. This effect can be explained by assuming the teeth as lumped masses, applied on the root circle, that somehow pull the whole structure along the radial direction, in presence of the centrifugal field. Thus, this effect leads to a relevant stress enhancement around the fillets. Then, what is possible to notice is a symmetrical stress distribution with respect to the centreline of the compartment between the teeth. In particular, it is easy to recognize two yellowish areas characterized by the maximum stress concentration factor. The compartment, indeed, is not characterized by a full round fillet rather by two variable radius fillets, where it is possible to detect an important notch effect. However, this detail seems to disappear in the outer fillets of the sector of interest but we have to specify that this is only due to the mesh size in those areas. Anyway, the numerical superposition has been limited to the central fillet of the 4-teeth sector, where the good accuracy of results is assured. Finally, despite what we may have thought, the centrifugal

stresses have a relevant importance and we cannot ignore them. The high spinning speed of 10000 rpm, indeed, is able to induce equivalent stresses up to the order of 100 MPa. Almost one order of magnitude more than the extent of the most critical stresses induced by the mesh load.

4 MULTIAXIAL FATIGUE

Two different fatigue failure criteria have been selected for the evaluation of the extent and the location of the critical stress state in the mechanical fatigue process. However, before applying a suitable fatigue failure criterion, it has been necessary to work out the numerical values of stresses of each elements of interest. In particular, since the mechanical fatigue is a process over time we had to rebuilt the time histories of the tensor components. The spinning speed of 10000 rpm enables the gear to complete a single revolution in 0,006 s. Each tooth experiences the mesh load only once per revolution. Therefore, setting the instant 0 s as the moment at which the tooth 2 (benchmark) comes into engagement, after 0,006 s the loading history on the elements gets repeated. Therefore, the stress histories that are going to be shown next can be seen as periodical signals with a period equal to the time needed by the gear to carry out one single revolution. The centrifugal field, indeed, induces mean stresses that can be algebraically summed to the step load trend, arisen from the teeth engagement, instant by instant. Thus, these components don't change the "shape" of the stress history, but they can either shift it downwards (compressive stresses) or upwards (tensile stresses).

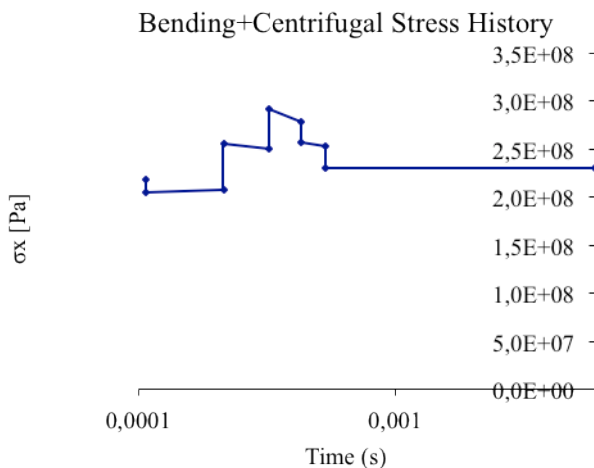


Figure 6 Superposition of bending and centrifugal effect: time history of the tensor component σ_x , for an analyzed element, time scale is logarithmic for highlighting the stress values.

In Figure 6 the reader is allowed to appreciate the time history of the stress tensor component σ_x of an element, over a complete revolution.

4.1 COUNTING CYCLE METHOD

As far as the gear is concerned, after having analyzed different models for the prediction of the fatigue failure, the time has come for the application of the following fatigue failure criteria: Sines and McKnight. Both models presented by the paragraphs 2.2 and 2.3 involve mean stress tensors and alternating stress tensors. Therefore, it has been necessary to think of a proper mean for working out constant amplitude cycles from a non-uniform time histories.

The time trends of the shear and normal stress components are not sinusoidal functions but it is still possible to talk about periodic signals. In specific, as it has already been said, each stress state is repeated after 6 ms (period revolution). Therefore, by insulating an observation time, beginning and ending at the maximum stress value, it has been thought to apply the "Rainflow" counting method in the so called "bathtub" version. Nevertheless, the extraction of constant amplitude cycles out of non-uniform stress histories was not so straightforward. For sake of clarity, it has been reported the following example. Firstly, each loading condition has been numbered in a chronological way (first condition at $t=0s$, last condition at $t=0,012s$). Then, the Rainflow cycle counting method has been applied over σ_x and τ_{xy} histories.

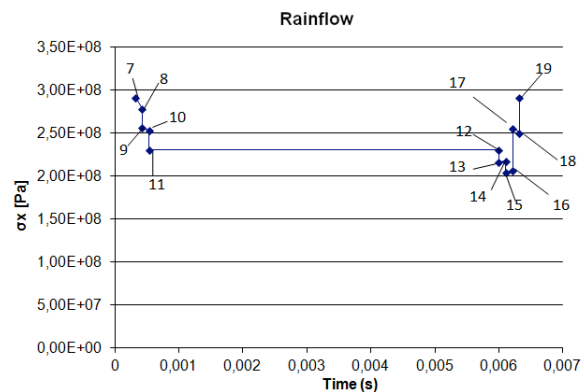


Figure 7 Time sample needed for the application of the "Rainflow" method on the time history of σ_x .

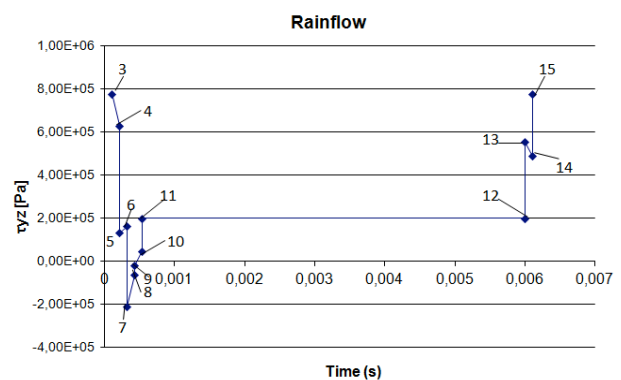


Figure 8 Time sample needed for the application of the "Rainflow" method on the time history of τ_{xy} .

What comes out from the Figures 7 and 8 is the different shape of the two “bathtubs”. Thus, by proceeding with the application of the Rainflow it is possible to extract the following cycles out of the two stress histories (Table II).

Table II - Constant amplitude cycles extracted from σ_x and τ_{xy} history, by means of Rainflow method.

Cycle	Peak-Valley σ_x	Peak-Valley τ_{xy}
1	7-15	3-7
2	17-18	13-14
3	14-13	6-5

The alternating and mean stresses in Sines and Manson-McKnight formulas are to be computed across a couple of stress tensors, identifying two specific loading conditions. However, by comparing the second and the third column of the table II it is possible to notice a mismatch in the number couplings representing the peak and the valley of the characteristic cycles. As a consequence, none of the selected fatigue criteria can be properly applied.

Whence, what has been done in order to solve this ambiguity was to reduce the three-dimensional stress state to an equivalent mono-dimensional one. In specific, we developed a different counting methodology through the application of Von Mises criterion [15]. By applying the corresponding formula to any “sampling instant”, the revolution period T is made of, indeed, we were able to rebuild the characteristic time trend of an equivalent stress σ_{eq} (Figure 9). Thus, having obtained a unique time history representative of the three dimensional stress state of the element under investigation (over a single revolution of the gear) it has been possible to apply the Rainflow method so by-passing the problem of the non proportional load histories. Finally, each peak valley association (column 1, Table III) were, then, picked to identify the tensor couples needed for the fatigue life prediction. By applying Sines and Manson-McKnight criteria, indeed, it has been possible to compute the mean and the alternating equivalent stresses associated to each of the characteristic cycles (Table III).

Table III - Fatigue criteria application (most stressed element): Sines VS/ Manson-McKnight.

Peak-Valley	$\sigma_{m,eq}$ Sines [Pa]	$\sigma_{a,eq}$ Sines [Pa]	$\sigma_{m,eq}$ Mans.-Mck [Pa]	$\sigma_{a,eq}$ Mans.-Mck. [Pa]
7-15	2,93E+08	4,68E+07	2,97E+08	4,68E+07
17-18	2,98E+08	3,10E+06	3,04E+08	3,10E+06
14-13	2,55E+08	4,83E+08	2,58E+08	4,83E+05

4.2 HAIGH DIAGRAM

For the safe life approach in gearbox design the manufacturer has to make sure that every component will never be involved in any crack nucleation phenomenon. In order to fulfil this requirement, the equivalent stress

amplitude of the critical cycle has to be lower than the endurance limit. The Haigh Diagram has been used for the fatigue strength assessment of the component. In specific, having assumed AISI9310 as constituting material of the gear, it has been verified that all the points $(\sigma_{m,eq}, \sigma_{a,eq})$, univocally representing the loading cycles, are included within the triangular region defined by the Goodman’s limit curve. By looking at the Figure 10, it is possible to notice how Manson-McKnight slightly overestimates the mean equivalent stresses with respect to Sines whereas, as far as the equivalent stress amplitudes are concerned, they basically predict the same values. In addition, none of the constant amplitude cycles is able to induce a fatigue failure. Nevertheless, the Figure 10 refers to a specific element. Thus, in order to verify the infinite life of the component it would be necessary to reiterate the whole procedure for any element at the tooth root fillet. However since the stress history of the element under investigation is qualitatively representative of all the elements of the fillet, it has been enough to identify a critical cycle for all the centroid involved in the analysis. To this aim, the safety factors have been computed, by assuming a proportional increment between the mean stress, $\sigma_{m,eq}$, and the equivalent stress amplitude $\sigma_{a,eq}$.

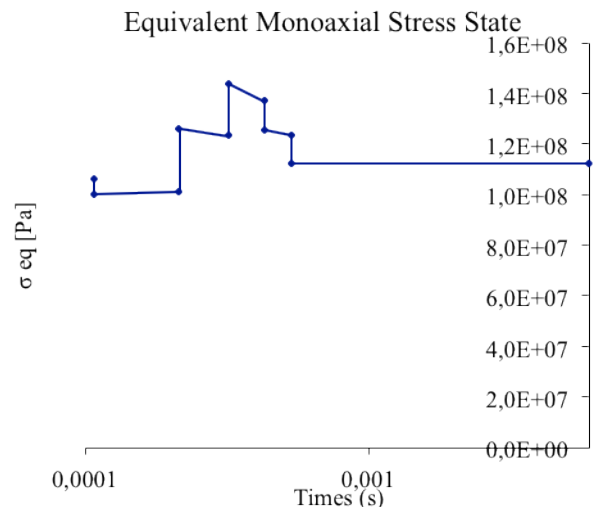


Figure 9 Time history of the equivalent mono-axial stress state (σ_{eq}).

What comes out is that the couple 7-15 is the cycle characterized by the minimum safety factor. So finally, for each element, it has been enough to apply Sines and Manson-McKnight criteria across the tensors 7-15. This way it has been possible to compute the critical values of mean equivalent stress and equivalent stress amplitude to be put in the Haigh Diagram. In specific, for the case being analyzed, the combined effect of the mesh load and the centrifugal field is unable to induce a fatigue failure of the component at the tooth root fillet. In fact, all the critical stresses, experienced by each element, are anyway contained within the triangular safety region of the Haigh Diagram, with a certain safety factor.

5 DYNAMIC EFFECT

5.1 INTRODUCTION

Having analysed the combined effect of the inertial and the mesh load, it is now time to shift our focus on the dynamics of the gear. As it has already been pointed out many times, gear transmissions, throughout their working life, undergo relevant vibrations that cannot be neglected in case of accurate design process. Thus, this paragraph is dedicated to better understand the influence of the dynamic behaviour as a further feature affecting the stress field at the tooth root.

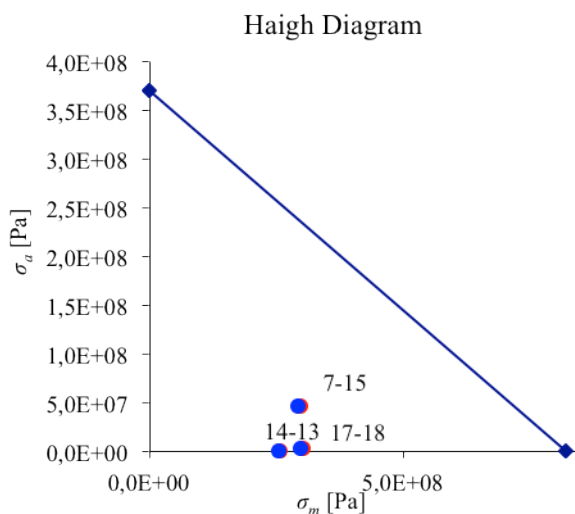


Figure 10 Haigh Diagram: cycle representation through monoaxial equivalent stresses.

5.2 FREQUENCY RESPONSE FUNCTION

The modal analysis in structural mechanics can be described as an useful medium for the dynamic characterization of components. In specific, it allows the analyst to determine the mode shapes and the corresponding frequencies during free vibration.

The characteristic parameters affecting the free response of the component are essentially three:

- The masses and the moment of the inertias of the structure
- The stiffness of the structure
- The boundary conditions in terms of restraints, applied to the structure.

However, the normal modes so computed do not represent the actual response of a system undergoing an external excitation. The FRF solution, instead, allows to map the amplitude of the dynamic response as a function of the exciting frequency. In order to successfully complete this study, it has been necessary to feed a further physical parameter of the gear to the FEM solver: the damping. By the way, it has to be said that the estimation of this additional parameter would require an accurate study of the material behaviour, the lubrication conditions and the friction effect. However, since the research study couldn't afford experimental tests on physical components, a reasonable damping ratio has been picked from the

literature about gears: ζ equal to 0,01. As the name of the paragraph 5.2 suggests, the output of this analysis will be a function linking a dynamic parameter (i.e. stress displacement, velocity, etc.) on the ordinate axis to the frequency (independent variable measured in Hertz). Thus, during the boundary condition definition it has been necessary to specify an exciting force to be associated to a frequency field. Through a careful bibliographic research [3] it is highlighted how the internal sources of vibration (transmission errors) explicate the system excitement in relation to the meshing frequency of the teeth. Thus, being z_1 the number of teeth of the gear and n_1 its working spinning speed it is easy to compute the exciting frequency as:

$$f_z = \frac{n_1}{60} z_1 \quad (19)$$

In other words, the gear experiences z_1 "shocks" per revolutions and dynamically responds with a frequency equal to the meshing frequency.

The reasons underlying the vibration phenomena of gearings have been deeply investigated. However, due to the complexity of the problem, it has been picked an harmonic forcing function with amplitude equal to $\frac{1}{2}$ the force exchanged between the teeth ($R=0$). In addition, having identified the upper point of the single contact region as critical for the bending load, this exciting force has been distributed over the nodes along the face width.

The FRF analysis involves the frequency domain. For the specific case, the exciting frequency has been swept over the range 100 Hz-5000Hz and the Von Mises equivalent stress function has been computed as an indirect measure of the dynamic response of the gear.

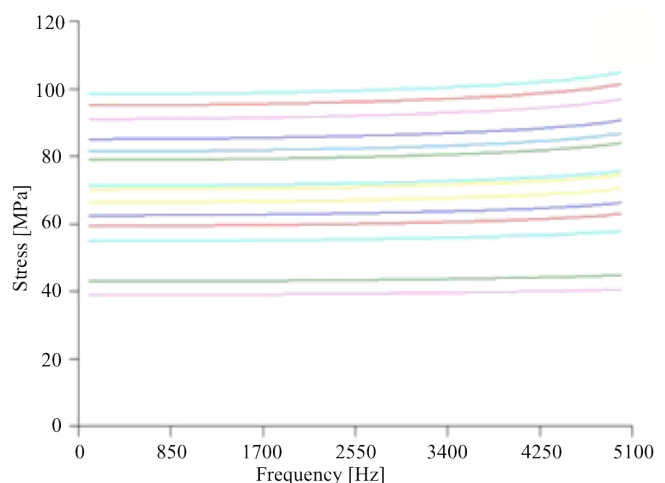


Figure 11 Frequency Response Function: Von Mises stresses for the elements representative of the tooth root fillet.

Therefore, in the Figure 11 the reader can appreciate the frequency response functions concerning some of elements belonging to the fillet. What is pretty clear is that all the stresses, steadily increase as the exciting frequency grows. Nevertheless, no relevant peak resembling somehow a

resonance is detected. After being questioned about the meaning of such a FRF, a clarification has been provided by the modal analysis. By checking all the normal modes, indeed, it is pretty evident that none of these is able to massively deform the tooth root fillets. As a consequence, all the response functions slightly increase along the abscissa axis. However, as we already said, the dynamic behaviour is influenced by the mass and the rigidity of the structure. Thus, the focus of the investigation was shifted on a specific constructive parameters: the rim thickness. It is worth remembering that so far it has been analysed a gear with a pretty high back up ratio ($m_b=3.3$). Therefore, it is pretty intuitive that the thickness of the rim contributes to the stiffening of the structure somehow, by preventing any inflections of the tooth root fillets. Hence, in order to give robustness to this theory it has been necessary to repeat the FRF for a gear having a backup ratio, m_b , equal to 1 and a very thin web (Figure 12).

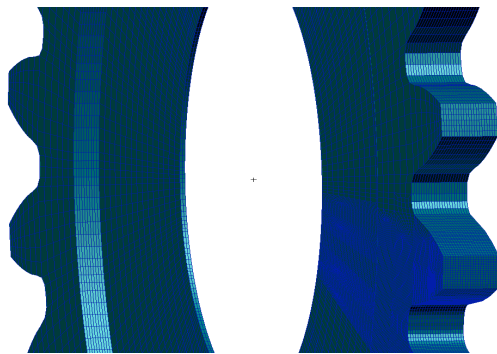


Figure 12 Minimum Backup Ratio ($m_b=1$): 3D mesh of the complete gear model.

Thus, by applying the same boundary conditions as the previous case, it has been possible to compute the frequency response functions of the corresponding elements. As it was expected, the FRF plot has drastically changed. Indeed, it is now evident the presence of preferential frequencies where the amplitude of the response is a relative maximum. In particular, the main peak of all the functions is detected at a frequency of 4510 Hz. The final goal of this research work is the development of a methodology aimed to the superposition of all the main effects involved in the mechanical fatigue process. Thus, in order to stress out the importance of the dynamic response on the fatigue life of the component, it has been assumed a new operative frequency coincident to the main resonant frequency. Once again, the modal analysis turns out to be really useful for the comprehension of the FRF.

In particular, what the Figure 14 shows is the 31st mode shape of the present gear, detected at a frequency of 4520 Hz. Since the new working condition is really close to the 31st natural frequency, indeed, it is reasonable to think that the actual response of the gear somehow resembles the mode shape under investigation.

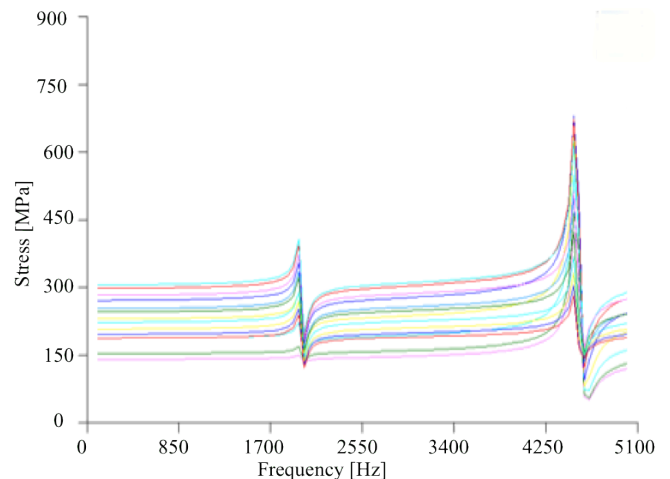


Figure 13 Frequency Response Function: Von Mises stresses for the elements representative of the tooth root fillet in case of minimum $m_b=1$.

As it was expected, this normal mode is characterized by a massive deformation of the web and of the rim. Due to a lower stiffness of the structure, thus, the tooth root experiences an important strain-stress state. As a consequence the FRF reflects a very high peak for a frequency of 4510 Hz. Then, it has been possible to numerically evaluate the extent of the dynamic overloads at the working frequency, in percentage:

$$K_s = 100 \frac{\sigma_{FRF,j} - \sigma_{stat,j}}{\sigma_{FRF,j}} \quad (20)$$

where $\sigma_{FRF,j}$ is the equivalent stress of the j-th element at the working speed and $\sigma_{stat,j}$ is the static stress (frequency equal to 0 Hz) of the j-th element.

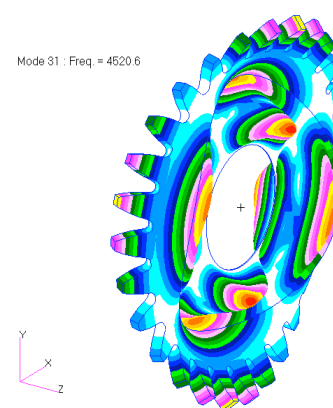


Figure 14 31-th Mode shape (4520 Hz).

In specific, the graph reveals, the dynamic response of the gear can induce a stress enhancement up to 205,85 % static stress. However, it is common to use a further index for the estimation of the dynamic overload. In specific, all the standards about gears prescribe formulas for the computation of the dynamic factor K_v [4], whose most general definition is:

$$K_{v,j} = \frac{\sigma_{FRF,j}}{\sigma_{stat,j}} \quad (21)$$

Once carried out the FRF analyses, thus, it has been straightforward to compute the numerical value of the dynamic factor for the elements, through the equation (21). Nevertheless, the K_v factor has also been calculated according AGMA and ISO [6,7], respectively the American and the European standards about gears. Thus, the following the Table IV is aimed to compare the goodness of the analytical results with respect to the numerical ones, for the most critical element.

Table IV – Intensification factor at the working frequency: numerical and analytical result comparison.

K_v	$K_{v,AGMA}$	$K_{v,ISO}$
3,0585	1,2617	1,1316

In specific, the outcome of the table IV warns the reader about the usage of the standards. Although AGMA and ISO represent the two main references for the gear designers, it is evident how the values of K_v listed in the column 2 and 3 of the table excessively underestimate the dynamic overload. From the study, thus, it turns out that for thin rim gears the dynamic contribution cannot be overlooked. In addition, the designer is recommended not to rely on standard prescriptions without resorting to an accurate FEM analysis for the dynamic characterization of the component.

5.3 DYNAMIC EFFECT SUPERPOSITION

Throughout the section 5 of the report the reader had the chance to figure out the role of the dynamics in the determination of stress state of the tooth root fillet. The former paragraph, in particular, quantitatively determined the extent of the overloads induced by the dynamic response of the component, in presence of an harmonic excitement. Therefore, this last paragraph is aimed to provide an answer to the final open question: how to superimpose the dynamic stresses to the mesh and the inertial load. For each of the elements of interest (thin rim gear with $m_b=1$), it is possible to compute the dynamic factor K_v corresponding to a certain working speed. These dimensionless numbers, basically, represent a direct measurement of the relative stress increment due to the dynamic response of the gear with respect to the static mesh load. Therefore, having computed the stress histories of each element, it has been thought to multiply all the tensor component time trends by a scale factor equal to the corresponding K_v . Finally, having validated this methodology for the superposition of the dynamic effect, the centrifugal mean stresses have been summed to the alternating stresses arisen from the “dynamic correction”, instant by instant. This way it has been possible to obtain the stress histories inclusive of all the three main effects.

Hence, the paper ends with the fatigue life prediction of the component. Nevertheless, no further Rainflow counting method has been performed to get constant amplitude

cycles out of a new equivalent stress history. By scaling all the stress components for the same corrective coefficient, indeed, the “bathtub” shape doesn’t change. Therefore, for each element it has been enough to apply the selected criteria across the tensors identifying the critical cycle (tensor 7 and tensor 15). Once again all the critical stresses are anyway located within the safe region of the Haigh Diagram. Thus, neither the addition of the dynamic contribution is able to induce a fatigue failure of the component at the tooth root fillet. However, even if the infinite fatigue life of the gear is predicted, the characteristic points get closer to the boundary of the triangular region, inducing a reduction of the safety factors compared to “static” case (Figure 15).

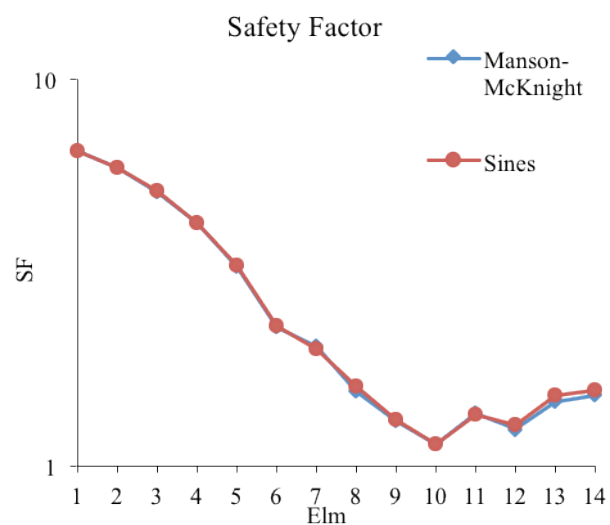


Figure 15 Safety factor of each investigated element, y-axis is logarithmic.

Finally, through a location coordinate check it is possible to state that due to a relevant dynamic response the maximum stress state has shifted towards the flank of the tooth rather than the middle of the fillet.

6 CONCLUSION

An investigation on the multiaxial fatigue in high speed gears is presented in the paper. Through a bibliographic research it has been investigated the scenario of the fatigue failure criteria. In specific, what comes out from the study is that none of the *stressed-based models* accounts for the stresses arising from the dynamic behaviour of the gear. By means of FEM analysis, then, it has been possible to trace the stress history experienced by the tooth root fillet. In case of “statics” the numerical results seems to fairly match the analytical results presented by the literature about gearings. However, the main outcome of the present study is about the dynamics. Through the FRF analysis it has been possible to figure out the extent of the dynamic overloads on a reference gear model. In specific, the application case being analysed is characterized by a

maximum K_v factor of 3,0585. However, the paper warns the reader about the usage of the international standards of gears. In presence of thin rim (low backup ratio), indeed, AGMA and ISO excessively underestimate the dynamic overloads. Therefore, by exploiting the results of the FEM, the numerical values of K_v factors have been exploited as multiplying coefficients of the static stress histories. This way, it has been possible to apply two selected fatigue criteria on a stress scenario (in the time domain) already inclusive of all the three main effects: bending, centrifugal and dynamic.

NOMENCLATURE

Symbol	Description
m_b	Backup ratio
$\Delta\tau$	Shear stress amplitude
σ	Normal stress
k	Material constant
R	Stress ratio
$\sigma_{i,max}$	Maximum normal stress
$\sigma_{i,min}$	Minimum normal stress
$\tau_{i,max}$	Maximum shear stress
$\tau_{i,min}$	Minimum shear stress
σ_a	Alternating normal stress
σ_m	Mean normal stress
$\sigma_1, \sigma_2, \sigma_3$	Principal stresses
$\sigma_{m,eq}$	Mean equivalent stress
$\sigma_{a,eq}$	Alternating equivalent stress
f	Fatigue limit in axial loading ($R=-1$)
σ_{D-1}	Fatigue limit in bending loading ($R=-1$)
σ_{UTS}	Ultimate tensile stress
$V(M)$	Elementary volume
$\sum(M, t)$	Macroscopic stress
$E(M, t)$	Macroscopic strain
$\sigma_{m,t}$	Microscopic stress
$\varepsilon_{m,t}$	Microscopic strain
t	Time
T	Revolution period
σ_{eq}	Equivalent stress
ζ	Damping ratio
f_z	Meshing frequency
n_1	Spinning speed
z_1	Number of teeth

K_s	Percentage of load increment
$\sigma_{FRF,j}$	FRF stress output
$\sigma_{stat,j}$	Static stress
K_v	Maximum dynamic factor
$K_{v,AGMA}$	Dynamic factor according AGMA
$K_{v,ISO}$	Dynamic factor according ISO

REFERENCES

- [1] Buckingham E., Dynamic loads on Gear Teeth, *Machinery*, pp. 117-121, 1958.
- [2] Timoshenko S. and Baud R. V., Strength of Gear Teeth, *Mechanical Engineering*, Vol. 48, p. 1105, 1926
- [3] Baud V. and Peterson R. E., Load and Stress Cycles in Gear Teeth, *Mechanical Engineering*, Vol. 51, No. 9, p. 653.
- [4] Niemann G., Winter H., *Elementi di Macchine*. vol. 2, Studio M&B, 1986.
- [5] Socie D. F., Marquis G. B., *Multiaxial Fatigue*. Society of Automotive Engineers Inc, 1999.
- [6] International Standard ANSI/AGMA 2001-C95.
- [7] International Standard ISO 6336-3.
- [8] Filippini M., Folletti S., Criteri Multiassiali e Nucleazione di Fratture per Fatica in Materiali per l'Impiego ad Elevata Temperatura, *Congress IGF19*, Milano, July 2-4, 2007.
- [9] Sines G., Failure of materials under combined repeated stresses with superimposed static stress, *National Advisory Committee for Aeronautics* (N.A.C.A), Technical Note 3495, Washington, 1955.
- [10] Findley W. N., A theory for the effect of mean stress on fatigue of metals under combined torsion and axial load or bending. *J Eng Ind, Trans ASME*, Vol. 81, pp. 301-6, 1959.
- [11] McDiarmid D. L., Fatigue under out-of-phase bending and torsion. *Fatigue Eng Mater Struct*, Vol. 9, No. 6, pp. 457-75, 1987.
- [12] Dang Van K., Griveau B., Griveau O., On a multiaxial fatigue criterion. Theory and application, *Rapport SKF*, R.E. 1123.
- [13] Lewicki D., Crack Propagation Studies to Determine Benign or Catastrophic Failure Modes for Aerospace Thin-Rim Gears, *NASA Technical Memorandum* 107170, *U.S. Army Research Laboratory Technical Report* ARL-TR 971, pp. 1-182, 1996.
- [14] Roccati G., *Elementi Costruttivi delle Macchine*. CeTeM, Politecnico di Torino, 2004.
- [15] Meggiolaro M.A., Pinho de Castro J.T., An improve multiaxial rainflow algorithm for non-proportional stress or strain histories-Part II: The modified Wang-Brown method, *International Journal of Fatigue*, pp. 194-206, 2012

MAGNETO-INDUCTIVE ENERGY HARVESTING: APPLICATION TO A COMPUTER MOUSE

Elvio Bonisoli

Nicolò Manca

Politecnico di Torino, Dept. of Management and Production Engineering

ABSTRACT

Feed electrical wireless devices by recycling the energy “wasted” in other phenomena is the main aim of the energy harvesting process. However, the reduced amount of available energy compared to the requirements of common electrical devices, is due not only to the type of source but also to the dimensional constraints imposed, and it makes necessary to develop a design method able to optimize the energy recovery performance of the device adapting it to the specific application.

In the present study, a linear magneto-inductive energy harvester is considered. To highlight the potential of such device and the robustness of the developed design method, a particular application characterized by stringent constraints in terms of dimensions, available energy and power requirement is analysed; this is a computer mouse. The purpose is to make the device electrically independent. The considered application allows illustrating the effectiveness of a design procedure that combines methods for signal analysis, for modelling of the device, and for optimization of the parameters in the design of an energy harvester. The aim is to show the strength of an integrated process that allows the development of devices suitable for a large variety of applications.

Keywords: energy harvester, mouse

1 INTRODUCTION

Through the recovery of the energy “wasted” by other phenomena, energy harvesting devices derive energy from non-traditional alternative sources typically present in everyday life, in order to transform it into directly available electrical energy.

The desire to recover energy from this kind of sources stems from different factors, mainly the exigency of reducing the energy demand from traditional sources and the need to make electrically autonomous devices that can

be placed in isolated positions difficult to reach. Energy harvesting devices described in literature [1] exploit multiple physical phenomena to convert into electricity the energy present in the environment where they are. The type of energy harvester (EH) considered in this study is based on the phenomenon of electromagnetic induction generated by a moving magnet that moves linearly inside a coil in response to a vibrational excitation [2,3]. Studies conducted by DIGEP, DENERG, S. Tornincasa, M. Repetto et Al. [4, 5, 6] have been successful in two practical cases of great interest showing that such device is particularly effective from the standpoint of the recovered energy density; they made electrically independent a sensor for monitoring pressure and temperature inside an automotive tire and a pedometer inserted in the sole of a shoe. In the present study, a further step has been taken by analyzing a particular application characterized by even more stringent constraints. This is energy harvesting applied to a computer mouse, i.e. to a device whose movement is the source to

Contact author: Elvio Bonisoli¹, Nicolò Manca²

¹Politecnico di Torino
Dept. of Management and Production Engineering
Corso Duca degli Abruzzi, 24 – 10129 Torino, Italy
E-mail: elvio.bonisoli@polito.it , nicolo.manca@polito.it

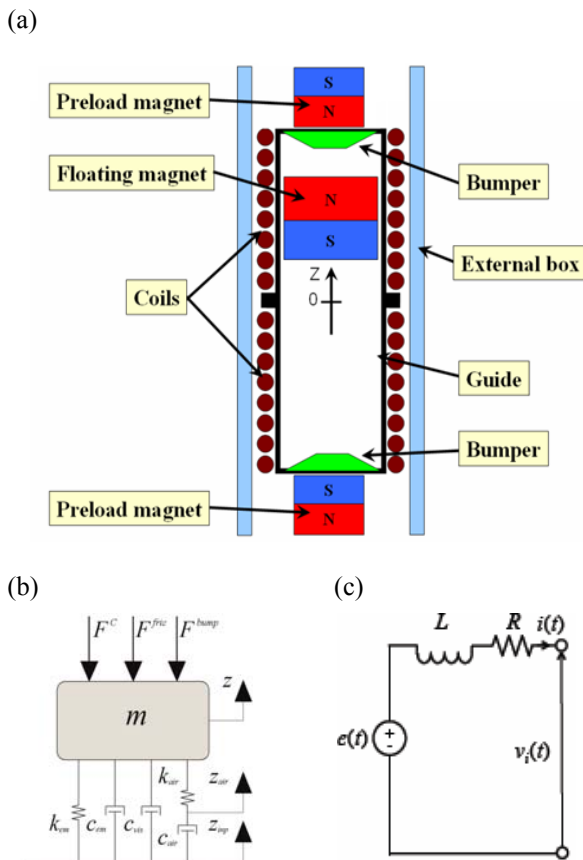


Figure 1 EH device components (a), dynamic model of the forces acting on the moving magnet (b) and electrical scheme (c).

exploit and whose operation is the electrical load to feed. The purpose is to make the device electrically independent. This type of application presents strict dimensional constraints, due to the small space that an EH inserted into a mouse can occupy. Furthermore, compared to the case of the tire and of the shoe, it also presents more rigorous input conditions; in fact it must recover energy from low intensity and frequency vibrations, therefore having a lower energy content. The developed design procedure results very effective in adapting the device at the particular application through an integrated process that combines methods for signal analysis, for modelling of the device, and for optimization of the energy harvester parameters; furthermore the versatility of the method allows developing energy harvester devices suitable for a large variety of applications.

2 THE EH DEVICE

The energy harvester considered is a device able to recover energy from the movement, or rather from the vibrations of the system on which it is installed. It is based on the electromagnetic induction phenomenon: a magnet is moved by the vibrations which excite the system and, moving with

respect to fixed coils, induces electromotive force and electric current, generating power. The power is recovered and used to power an electrical load, in this case a mouse. Two preloads magnets inversely oriented with respect to the moving magnet make it oscillate around a central equilibrium position, figure 1.a.

From the mechanical point of view, the device can be modelled as a mass-nonlinear spring-damper system, where the moving magnet represents the mass, the preload magnets the non-linear spring and the coils the damper. Actually, other two contributions are present: the dissipative one caused by friction between the moving magnet and the guide, and the one, both elastic and damping, due to the presence of the air which is compressed by the moving magnet during its movement. Figure 1.b shows the mechanical scheme of the forces acting on the moving magnet, m , along the axial direction where F_C is the input force, F_{fric} is the friction force due to the contact with the guide, F_{bump} is the force generated by the contact with the bumpers, k_{em} and c_{em} represent the electromagnetic coupling with coils, k_{air} and c_{air} represent the pneumatic effect of the air in the device and c_{vis} represents the viscous effect.

From the electrical point of view, the EH device can be seen as a non-ideal voltage generator, as not only the resistance and the inductance of the applied load are considered, but even the resistance R and inductance L of the coils, figure 1.c.

3 DESIGN PROCEDURE

The design procedure counts of different steps. What makes it versatile and easily adaptable to the design of energy harvester intended for a vast number of applications is the fact that, once the dimensional constraints and the accelerometric stories to be analysed are set, it is completely detached from the specific application case thanks to a core model based on a parametric geometry. In this way solutions that are well adapted to the various needs can be obtained.

Contextualization: the first step consists in the contextualization of the EH in a specific application environment by analysing the dimensional constraints and by sampling the accelerometric stories relating to the movement of the device. The following frequency analysis allows defining which are the main harmonics of the input signal to the system, namely the motion of EH, and through the PSD analysis estimating its energy content in different situations; in this way it is possible to select the best positioning and orientation of the harvesting device.

Performance simulation: the best input condition and the dimensional constraints known, a preliminary configuration of the design parameters is defined in order to simulate and analyse the performance of the EH by implementing a simulation software; it is a software based on a parametric Matlab model integrated with Simulink, FEMM and

Solidworks developed by POLITO DIGEP, DENERG, S. Tornincasa, M. Repetto & Al. [7]. By varying the values of the different design parameters, the influence they have on the power recovery is highlighted; it is so defined where to go to act in the following optimization process.

Optimization: the last step of the design procedure consists in the optimization of the design parameters in order to obtain the optimum condition in terms of power recovery. The optimization process performs an iterative process that implements different optimization algorithms as Matlab `fmincon` and `pattern search`; by varying the desired parameters in a coherent range, the process continues until the best result is reached.

4 DESIGN PROCEDURE

4.1 CONTEXTUALIZATION

4.1.1 Constraint definition

For the mouse application the EH model considered is a cylindrical shape device; the overall dimension constraints are defined so that the size of the device is comparable with an AA battery, namely height of 50 mm and diameter of 14 mm; in this way it is possible to place more than one EH device in the mouse. All the magnets are cylindrical and their dimension can vary accordingly to the constraint imposed; the preload magnets present the same dimension in order to make the harvester symmetric. The two coils are obtained by wrapping opposite a copper wire; they are connected in series in order to add the effects of the inductance generated by the moving magnet which enters one and quits the other.

4.1.2 Movement recording

The recording of the input signal to be used to simulate and analyse the performance of the EH device consists in tracking the accelerometric stories referring to the mouse movement and it is performed in two different experimental ways; both of them present advantages and disadvantages and is better suited to the study of a particular usage condition of the mouse. The first method is to record the track followed by the cursor on the screen and then go back to that of the mouse on the support surface; this procedure is easy to perform but, due to the non-linearity of the transfer function, its accuracy decreases with increasing speed of movement of the mouse. The other method consists in processing a video of the mouse during the movement; a coloured adhesive is pasted on the device and used as the reference point to follow in the image to define the movement of the mouse. This procedure, if on the one hand allows greater precision at higher speeds and displacements, on the other hand affects the reliability in case of small movements, due to the difficulty to register the variation of the position of the centre of gravity of the circular adhesive.

4.1.3 Strategies for energy harvesting

Given the nature of the application, in order to make the mouse electrically autonomous, two different strategies to perform energy recovery are considered:

1. harvesting energy exclusively from the movement of the mouse during its usage;
2. recovering energy mainly from an oscillating movement which must be performed before using the device.

The two strategies are very different from each other, and both have advantages and disadvantages. The first approach is certainly the most interesting but also the most difficult to achieve; in fact, it consists in providing a device identical in usage to those powered by USB cable or internal battery. However, the oscillations produced are very short in duration, limited in amplitude and very variable in time; there follows a considerable difficulty in energy recovery. The second approach allows working with much more regular oscillations with longer duration and greater intensity; therefore, energy recovery is easier. However, the "recharge" operation that must be done before using the mouse, makes the device less comfortable to use than the traditional.

In the following, the input signals in the two cases are analysed and the energy contents compared.

4.1.4 FIRST APPROACH: energy harvesting exclusively during the use of the mouse.

As anticipated, in this case it is considered to perform the energy recovery only during the use of the mouse; therefore it is necessary to harvest from the movement of the device the power needed to detect the operations performed at the same time, namely the movement and the use of buttons.

The normal use of the mouse implies that the EH device is subject to an input signal characterized by very short intervals of oscillation during which energy is recovered and consumed, alternate with periods of stop, generally longer, in which there is no recovery but may be only consumption, due for example to the "click" operations.

By decomposing the input signal along the axial direction of the EH and along the two radial directions perpendicular to it and perpendicular to each other, it follows that only one of the three contributions has a positive effect on the energy recovery. In fact, the axial component is responsible for displacement of the movable magnet along the coils, while the two radial components are responsible of friction between magnet and guide, due to the perpendicular movement of the device and gravity. It follows that a different orientation of the EH inside the mouse implies a different exploitation of the motion components. The comparison between the PSD along x and y directions, figure 2, shows that it is more convenient to align the axial direction of the EH device to the x-axis of the movement of the mouse. Obviously, intermediate placements between the two configurations considered are also possible.

Unlike other kinds of application [4, 5, 6] characterized by periodic input, due to the periodicity of the phenomenon that generates the vibration, in this case it is impossible to

identify a period repeated with regularity; in addition the available accelerations are considerably lower. Therefore, it is necessary to identify some significant intervals and to study the behaviour of the EH in these conditions. Three

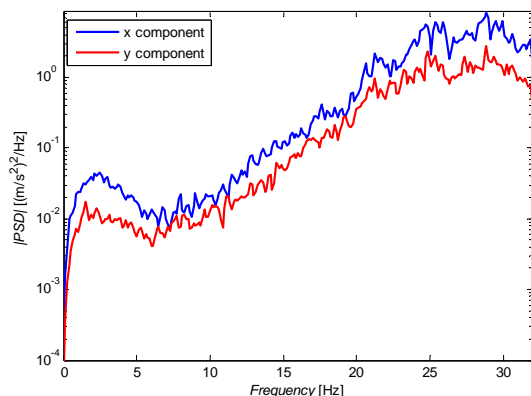


Figure 2 PSD comparison components along x and y (a)

intervals characterized by low (a), medium (b) and high (c) input intensity, with respect to the average, have been selected. As can be seen in figure 3, the three intervals present very different features, both from the standpoint of the energy content, both from the standpoint of the main harmonic frequency.

4.1.5 SECOND APPROACH: energy harvesting mainly from an oscillatory movement before use

The second approach to energy recovery consists in exploiting mainly, and almost exclusively, an oscillatory movement that must be performed before using the device. In other words, before using the mouse, the operator makes it oscillate in order to store sufficient energy for the next use. As anticipated, this strategy presents advantages from the point of view of the input to the system, but disadvantages associated with the use of the mouse. An oscillating movement performed specifically for charging allows working with much more regular and longer in duration oscillations, but makes the device less comfortable to use than the traditional ones. Therefore, it is necessary to define a configuration of the EH which allows storing an amount of energy sufficient to operate with the mouse for an adequate period of time. Simple observations have shown that the oscillation along the x direction represents the best solution; it is a movement neither difficult nor laborious, and it can be performed using only the wrist or with the help of the forearm. Furthermore, since the EH is arranged as in the case of the previous analysis, this solution allows an energy recovery also during the use of the mouse. Figure 3 show the acceleration amplitude and the energy content of the principal harmonics of the various input signals identified as comfortable charging movement. They present displacement amplitude of about 5 cm, are all not tiring and can be performed with no fatigue even for a few tens of seconds. By comparing the energy content of the considered signals with the energy content of the mouse

movement in the first approach, it can be observed that the available, and therefore recoverable, power in this second case is much higher. Furthermore these kinds of inputs last for a longer period of time.

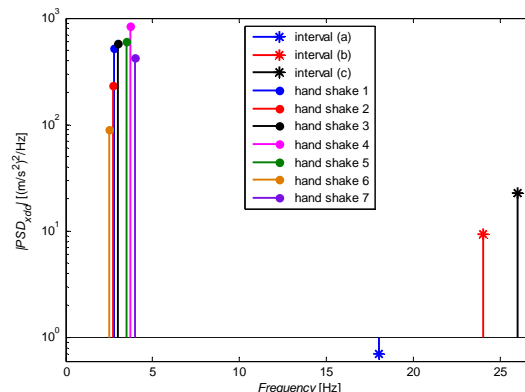


Figure 3 Comparison among the principal harmonic of the acceleration input signals in the first and second approach

4.2 PARAMETERS INFLUENCE

Before studying and simulating the two different operative situations, a preliminary study on the influence of the various design parameters on the performances of the EH is conducted. As obvious, the most influential parameters in defining the maximum recoverable power are the moving magnet size and its stroke. As a first approximation, the magnetic flux is proportional to the volume of the moving magnet and to an increase of its stroke, a greater variation of the magnetic flux corresponds, and thus a greater electromotive induced force. Clearly, the size of EH being defined, to the dimensional increase of the moving magnet corresponds the decrease of the available stroke. Therefore, they are two conflicting parameters of which it is necessary to evaluate the optimal ratio. The other parameter that greatly affects the energy recover is the size of the coils; the easiest way to change the value of the linked-flow is by adding or removing copper windings around the guide. However, this operation must be performed with caution since an excessive increase of loops leads to a small increasing of connected flow, compared to a considerable increase of the electrical resistance and, therefore, of leaks due to the Joule effect. In addition, the damping coefficient c_{em} is quadratically connected to the flux-linkage - the higher the flow, the higher the damping - and is inversely proportional to the resistance of the coil [5]. It follows that acting on the size of the coils means acting on a very influential parameter on both the electrical and the mechanical behaviour of the system; it should also be considered that increasing the radial dimension of the coils implies, due to the size constraints, a decreasing of the size of the moving magnet. Studies present in literature [5] show that the recovery is heavily influenced by the resistance of the load; in particular the better condition is obtained in matched load condition. Another aspect of extreme importance in the design is the alignment between

the resonant frequency, or better between the band of resonance of the system, and the main harmonics of the signal; this makes it is possible to have a movable magnet which is able to cover most of the available stroke, due to the

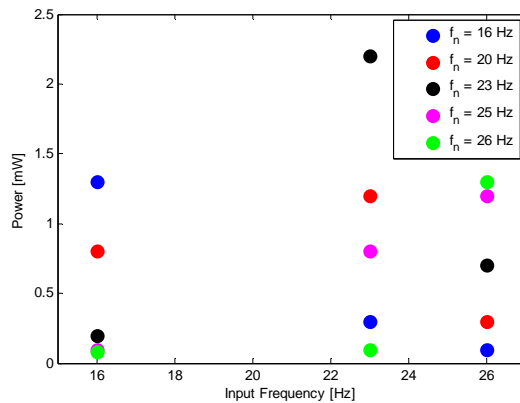


Figure 4 Input and natural frequency alignment effect

amplification of the input accelerations. To highlight this fact, figure 4 shows a comparison between the performance obtained keeping the moving magnet and coil dimensions constant and varying the preload magnet dimension in order to modify the resonant frequency of the EH is reported; a sinusoidal input signal has been used. The resonant frequency in the different cases is obtained through a sweep test. As expected, the best performance is obtained when the input frequency matches the resonant frequency of the system.

4.3 PERFORMANCE SIMULATION, OPTIMIZATION AND PROTOTYPING

4.3.1 FIRST APPROACH: energy harvesting exclusively during the use of the mouse.

The best configuration obtained presents a medium size moving magnet and a resonant frequency at around 27 Hz; the first feature allows having high available stroke without excessively penalizing the mild excitation operating conditions, the second allows resonating in these cases, and then obtaining the maximum energy recovery. The performance of the resulting model is simulated also considering the possibility of placing the EH with the axis 45° inclined with respect to the x direction. In this way, if on the one hand it is possible to exploit for the energy recovery both the mouse displacements along x and along y, on the other both produce a radial component in the force acting on the moving magnet causing the contacts against the guide. It has been observed how this configuration allows improving performance when the input signal is of very low intensity, due to the low friction forces produced, but excessively penalizes the operating conditions characterized by higher intensity inputs; therefore, the first solution is preferable. A prototype of the EH device is made. Before winding the coils, some experimental tests are performed to check the values of the parameters used in the simulation model. The experimental analysis points out

some errors in the estimation of the model parameters with consequent repercussions on the performance of the device. In particular, the experimental evidences show that the coefficient of friction between the moving magnet and the guide is significantly higher than the estimated using literature values. Tests with the updated values of friction coefficients show as the recovery of power in real conditions is much lower and inadequate to power the device.

As result it can be said that this type of model is inadequate for energy recovery under the considered input. Recover energy exclusively from the movement of the mouse during its normal use means to exploit too weak and too short oscillations, which not allow the floating magnet making large enough excursions. It follows that, with this sort of signal, the magnet moves almost integral with the guide.

4.3.2 SECOND APPROACH: energy harvesting mainly from an oscillatory movement before use

For the simulation and the optimization processes, the real friction coefficient previously got, have been used. Due to the smaller frequency of the input signal, the optimal configuration obtained for this kind of approach presents a couple of preload magnets very much smaller than in the previous case. To better exploit the higher energy content of the input signals, bigger coils have been used, always remaining into the defined dimensional constraints. The very high damping efficiency, due to magneto-dynamic optimization, allows obtaining very high power values with respect with the energy source. Table I summarises the performance obtained under the hand shaking inputs with two different EH configurations.

The second analysis has shown how this type of approach to energy recovery provides much better results than the previous one. The charging operation preceding the use of the mouse makes it possible to work with a signal having a decidedly higher energy content, characterized by a more regular and lasting oscillation. Moreover the very high power density with respect to the volume and to the very low energy source, allows continue recovering energy even during the normal operating conditions.

The optimization process has led to a configuration of the geometric parameters of the EH such as to allow an energy recovery that, for an excitation of medium intensity, is of the order of 5 mW.

Table I - Experimental input simulations

Hand Shaking	Configuration 1		Configuration 2	
	Power [mW]	Voltage [V]	Power [mW]	Voltage [V]
1	3.5	3.5	1.7	4.5
2	2.0	2.5	0.8	2.5
3	4.5	4.0	2.5	4.0
4	8.0	5.0	4.5	5.0
5	7.0	4.5	4.0	4.5
6	1.5	2.0	0.7	2.0
7	7.0	4.0	4.0	4.5

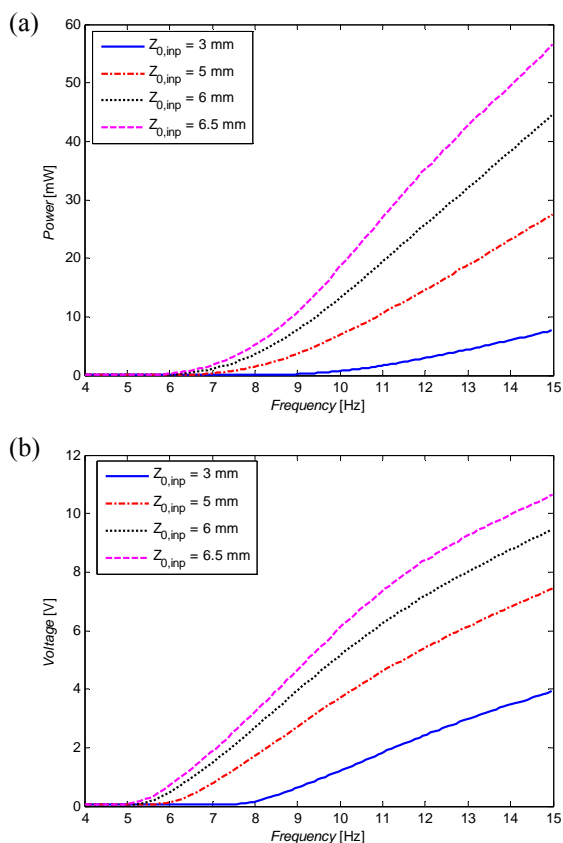


Figure 5 Sweep tests

Supposing to perform the charging operation for a time of 30 s, the stored energy amounts to

$$E = P_{EH} t = 5 \text{ mW} \cdot 30 \text{ s} = 150 \text{ mJ} \quad (1)$$

The consumption of a LED computer mouse is approximately

$$P_{mouse} = 2.5 \text{ mA} \cdot 1.5 \text{ V} = 3.7 \text{ mW} \cong 4 \text{ mW} \quad (2)$$

namely it consumes about 4 mJ per second of usage. Therefore, the charge performed makes the device autonomous in active mode for a period of

$$t_{active} = \frac{150 \text{ mJ}}{4 \text{ mJ/s}} \cong 35 \text{ s} \quad (3)$$

The investigation made on the use of the mouse has shown that, during a normal use of the device, its state of activation, i.e. the state in which energy is consumed to track the movement or to record buttons signals, is about 10% of the time that the operator spends at computer.

Consequently, the charging operation makes the mouse autonomous for a total time of about 6 min.

This result is certainly very positive. Furthermore, the small size of the EH also allows the use of two devices within the same mouse; in this way the energy recovery would be greatly increased as well as the autonomy of the computer device.

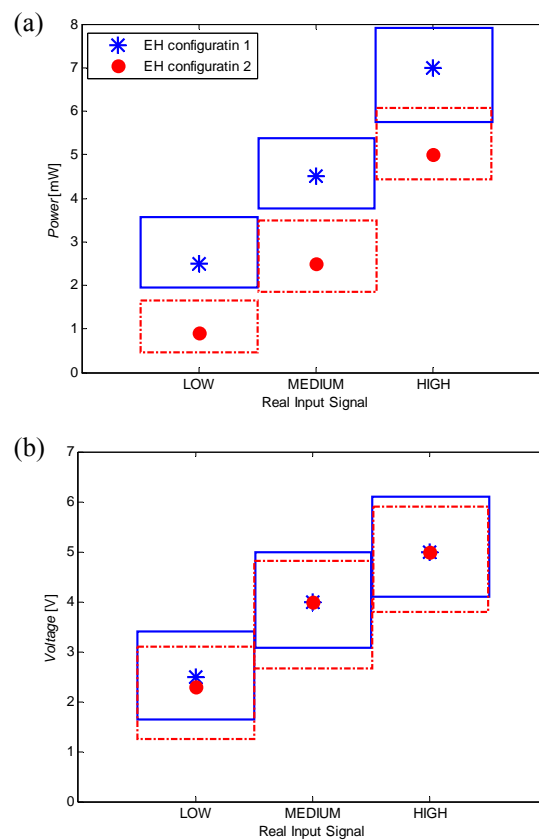


Figure 6 Real input simulations with 3 different oscillation frequency levels

5 PROTOTYPE CHARACTERIZATION

In the following a characterization of the prototype made is reported.

Main geometrical and dynamic parameters:

- external dimensions: $D \times h = \Phi 137 \times 480$ mm;
- natural frequency: $f_n = 5.7$ Hz;
- mechanical damping ratio: $\zeta = 51.7\%$.

Figures 5.a and 5.b show test sweeps made with different input amplitude. The reported results refer to “low to high” frequency sweeps. The results obtained with “high-to-low” frequency sweeps are qualitatively similar.

Figures 6.a and 6.b summarize the performance obtained with oscillatory movements having different frequencies executed by operator. For simplicity and to better give an idea of the type of the movement, the input signals are divided in “high”, “medium” and “low” frequency; these inputs respectively present frequency of about 4, 3 and 2 Hz.

6 CONCLUSIONS

With the aim of showing the potential of linear electromagnetic energy harvesters in energy recovery from low-intensity vibrational sources, a practical application has been considered: energy harvesting has been applied to a computer mouse in order to make it electrically autonomous.



Figure 7 Prototype

This type of device presents characteristics that are well suited to the purpose: it is a vibrating electric device which is both the source and the consumer of energy. Furthermore, the low intensity vibrations that characterize the input signals and the strict dimensional constraints make the design of considerable interest. The EH considered presents a linear monostable configuration; this device exploits the electromagnetic induction generated in a coil by a magnet that moves with linear translatory motion under the input of a vibrational signal. The geometrical constraints are the dimensions of an AA battery, namely a diameter of 14 mm and an axial length of 50 mm pins excluded. The study has been performed following two different approaches. The first approach is certainly the most interesting and consists in recovering energy exclusively from the movement of the mouse during its use. The second approach involves making a charging oscillatory movement before using the device in order to store the energy needed to power the mouse.

The analysis in the first case revealed that the obtainable performance with this approach to the energy recovery is very low and not sufficient to power the device.

On the contrary, the second recovery strategy has provided good results. It has been shown that by using a single EH a satisfactory autonomy of the mouse is achieved; in addition, the small size of EH allows the simultaneous use of several devices for energy recovery, improving the overall performance of autonomy.

The future targets are basically two. On the one hand, to perform the experimental verification of the results obtained with this analysis; if the performance is confirmed, it will be possible to proceed with the realization of the electrical part, and then of a prototype of a self-powered mouse. On the other hand, to improve the performance obtained by using two different types of linear electromagnetic energy harvester: the "sandwich" configuration and the bistable layout.

The first of the two configurations consists in exploiting a linear monostable EH in which the magnetic field generated by the floating magnet is made more variable in space. In order to obtain this feature, the moving element is split into several parts whose orientation is alternately inverted; for example, the floating magnet can be decomposed into three magnets where the first and the last are oriented in the same direction, while the central presents reversed polarity. Consequently, it is necessary to act on the number, the size and the winding direction of the coils in order to maximize the energy recovery. The bistable configuration consists in a linear EH characterized by a moving magnet whose stroke presents two equilibrium positions separated by a potential barrier. This method represents a possible solution providing good results even with the first approach to the energy recovery. Through a configuration of this type, by properly calibrating the potential barrier, a moving magnet that bounces from an equilibrium position to the other can be obtained. In this way, a longer stroke is exploited and, therefore, the energy recovery is improved, especially in the cases of low intensity excitations. As already pointed out, this solution involves greater difficulties both in the calibration of the bistable characteristic of the system, and in its practical realization.

In conclusion, the analysis presented in this paper shows that the energy harvester considered has the requirements for a satisfactory energy recovery, and there are also the conditions to improve the performance obtained. It is clear that devices of this type present an infinite number of possible applications, including cases characterized by severe dimensional constraints and low intensity excitations. In addition, it has been proven the efficiency of a modelling approach based on the integration of an accurate analysis of the input, a solid mathematical model and an effective optimization process, making the device adaptable to different application needs in a relatively simple way.

REFERENCES

- [1] Zhu D., Tudor M.J., Beeby S.P., Strategies for increasing the operating frequency range of vibration energy harvesters: a review. *Measurement Science and Technology*, Vol. 21, No. 2, pp. 1-29, 2010.
- [2] Von Buren T., Troster G., Design and optimization of a linear vibration-driven electromagnetic micro-power generator. *Sensors and Actuators A: Physical*, Vol. 135, No. 2, pp. 765-775, 2007.
- [3] Mann B.P., Sims N.D., Energy harvesting from the nonlinear oscillations of magnetic levitation. *Journal of Sound and Vibration*, Vol. 319, No. 1-2, pp. 515-530, 2009.
- [4] Tornincasa S., Repetto M., Bonisoli E., Di Monaco F., Energy harvester for vehicle tires: Nonlinear dynamics and experimental outcomes. *Journal of Intelligent Material Systems and Structures*, Vol. 23, No. 1, pp. 3-13, 2012.
- [5] Tornincasa S., Repetto M., Bonisoli E., Di Monaco F., Optimization of magneto-mechanical Energy Scavenger for automotive tyre. *Journal of Intelligent Material Systems and Structures*, Vol. 23, No. 18, pp. 2055-2064, 2011.
- [6] Tornincasa S., Repetto M., Bonisoli E., Di Monaco F., Robust Optimization of Magneto-Mechanical Energy Harvesters for Shoes. *Special Topics in Structural Dynamics*, Volume 6, Eds. Springer New York, 2013, pp. 571-576.
- [7] Tornincasa S., Bonisoli E., Di Monaco F., Virtual prototyping through multi-software integration for energy harvester design, *Journal of Intelligent Material Systems and Structures*, IN PRESS.
- [8] Bonisoli E., Di Monaco F., Manca N., Marcuccio G., Repetto M. e Tornincasa S., *Self-powered computer mouse equipped with a magneto-mechanical energy harvesting system for electrical power generation*, TO2013A000642, 2013.

METHODOLOGY TO INVESTIGATE THE MICROCLIMATE OF A CULTURAL HERITAGE INSERTED IN A SEMI-CONFINED ENVIRONMENT

Gianfranco Carcangiu* Marta Casti** Giuseppe Desogus** Paola Meloni*** Roberto Ricciu**

* IGAG–CNR - Istituto di Geologia Ambientale e Geoingegneria, UOS Cagliari

** Dipartimento di Ingegneria Civile, Ambientale e Architetture (DICAAR), Università di Cagliari.

*** Dipartimento di Ingegneria Meccanica, Chimica e dei Materiali (DIMCM), Università di Cagliari.

ABSTRACT

The aim of the research has been to analyse the decay observed in the semi-confined archaeological site in Cagliari. A multidisciplinary approach has been purposed. Differential decay with zones with great damage for the structures (pulverization, detachments, efflorescences) and other zones with less damage (only efflorescences) appeared from the survey conducted in the site. Diagnostics have been carried out to reveal the decay forms and their distribution; microclimatic monitoring has been carried out to detect temperature and relative humidity, eventually harmful values for the conservation and possible differential values of them inside the site. Sodium sulphate results the main decay agent and it is diffuse homogeneously inside the site. Microclimatic monitoring has detected a microclimatic zoning originated by the semi-confined environment. The zones closest to the outside have a trend very similar to it, instead the most confined one have a great thermal and hygrometric inertia. The comparison between the hygrothermal conditions monitored in the site and those thermodynamic favourable to salt crystallization has finally revealed the reason of the differential decay in site: different microclimatic conditions allow the sodium sulphate crystallisation as efflorescences in the zones most confined, and cryptoefflorescences in the closest to the outside one.

Keywords: microclimate control, differential decay, semi-confined environment, archaeological site.

1 INTRODUCTION

Semi-confined environment is a very widespread typology of environment especially in archaeological structures in which often shelters have been built for their conservation [1-3]. But it has been so far little explored and the studies until now are principally focused on outdoor and indoor environment [4].

The semi-confined environment can be more dangerous for the conservation because the shelters don't avoid the action of weather allowing changes of material and energy with the outside.

Moreover, such as the Ara Pacis blackening in 1990 [3], semi-confined environment allows a differential decay inside it favouring, for example, the preferential transport of pollutants in a specific part of the monument according microclimatic conditions [5, 6].

In other situation is frequent the development of the greenhouse effect as in the Perspex structures of Eraclea Minoa Theatre in Minissi's restoring [1, 2].

The changes of temperature induce differential expansions in the materials. High humidity is responsible for deterioration of many materials (wood and paper), biological attack [7] but also salt crystallisation in porous stones [8, 9]. Microclimatic changes may promote the pollution transport (mechanism of thermoforesis, diffusioforesis, Stefan flow) [3, 5, 7] and in presence of salt crystallization they are responsible to condensation-evaporation cycles [8, 9].

In particular salt crystallization in porous building materials is one of the principle agent of decay in historic monuments and archaeological sites. High ventilation increases evaporation velocity of the water solution promoting the growth of cryptoefflorescences inside the pores of the stone [10, 11], with great damage for porous materials according Everett law's [12]. Alkaline sulphates are very dangerous salts and they can be found especially in presence of

Contact author: Giuseppe Desogus¹

¹Email: gdesogus@unica.it

cement in polluted atmosphere [13, 14], very used in restoring of 19th and 20th century [8]; in particular sodium sulphate is the most dangerous salt used for this in the salt crystallization tests [10]. If many variations of thermohygrometric conditions happens, many changes in phases of the sodium sulphate can be produced. In the changes in phases an high damage for porous stones can be produced because the high crystallization pressures can exceed the resistance of the stone [15, 16].

In this work the differential decay observed in the archaeological site of Cagliari has been investigated correlating the microclimatic conditions monitored in the site with the crystallisation conditions of sodium sulphate contaminating the archaeological structures.

2 MATERIALS AND METHODS

2.1 DESCRIPTION OF THE CASE STUDY

The archaeological area of Viale Trieste 105 in Cagliari is a multilayered complex whose first phase is assigned to the late Punic and Roman-Republican; it was frequented until the early Middle Ages [17]. The site is characterized by masonry structures (Fig. 1), oriented according to the axis NE-SW, that delimit square areas built with biomicritic limestone blocks, parallel to a tripartite cistern. There is also a sewer disposed along the SE-NW axis, limestone pavement in the SW part, *signino* floors and a fragment of mosaic in the SE side.

The northern area, in correspondence of a section of the excavation, part of a *cappuccina* burial, with traces of incineration, was found. The function of these buildings is still uncertain, but the type of the floors and the thickness of

wall suggest that they could be connected to a settlement structure. During the excavation many evidences from different ages have been found such as fragments of Roman amphorae and roof tiles, painting plasters and coins [17].

The discovery of the site took place in 1985 during the works for the construction of office building by the Autonomous Region of Sardinia. Following the discoveries, a restriction was established for the archaeological area and an alternative solution was adopted for its exploitation (reduced, after the discovery, from 3870 square meters to 910 square meters). This situation has involved to the building of a reinforced concrete cover with supporting frame of the same material, raised at least two meters from the archaeological structures. On this cover, the parking, to which all the area was originally designed, was built (Fig. 2 a) with the aim to allow the archaeological excavations and the subsequent public use of the area [17].

This solution led to the formation of a semi-confined area because on the short sides of the site there are some openings that allow the exchange of matter and energy with the outside (Fig. 1). After the excavation, the site was abandoned until 2010 when it was performed some interventions aimed at recovering the area. The archaeological structures had a very advanced state of decay such as sputtering and detachment, biological colonization, salt crystallization, earthy deposits and accumulation of waste. Also the concrete structures showed a clear state of decay, characterized by cracking, detachments and salt crystallization with the presence of infiltrations of water in the pipes, arranged along the perimeter of the building envelope (Fig. 3).

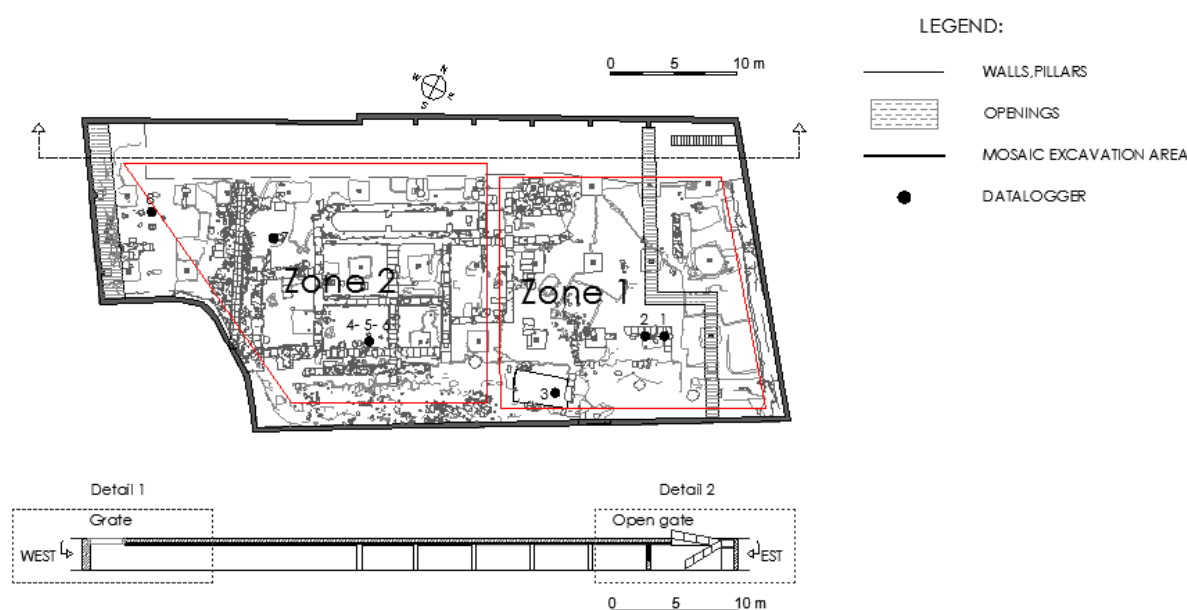


Figure 1 Map of the archaeological complex with indication of the walls and openings. In the SW side there is a small opening represented by a metal grate, in the NE side a larger opening constituted by a metallic railing. Localization of the data logger used for the microclimate monitoring; in red the identification of the two microclimatic zoning.



Figure 2 a View of the reinforced concrete floor supported by pillars; b View of the site after the insertion of the ceiling, added in February 2012.



Figure 3 SE wall: cement decay of the building envelope, water infiltrations from pipes and corrosion of metal structures.

During 2010's interventions, archaeologists conducted another excavation, with the aim to clean the site from the materials resulting from deposition of waste and ground accumulated over the years. The subsequent restoration concerned the cleaning and consolidation of walls, floors, plasters and mosaic. However, the restoration did not provide for removal the causes that contribute to maintaining a high level of humidity and to prevent the vehiculation of saline substances.

To overcome the infiltration phenomenon, favoured by the gaps in the cover, in February 2012, it was decided to realize sealing and to build a false ceiling (Fig. 2 b). However, high values of relative humidity were still measured in the site, due to the percolation of water from the pipes, its penetration in correspondence of the side openings and the consequent phenomena of capillary rise from the ground. Another constant source of humidity is represented by the water present in the cistern (about 30 cm). The saline sources are identified instead in the decay of the concrete structures and pillars but probably also in the entry of pollutants into the site; the parking, realized on the archaeological structures, is a very insidious source of

pollutants, interacting with the materials. For these reasons, despite the removal of salts from the surface structures, the phenomenon of salt crystallization persists but the decay phenomena have different degree of damage in the site with pulverization or detachments of the *Pietra Cantone* (lithotype dominant in these archaeological structures) in the zones closest to the opening, only efflorescences in the most confined one. In order to discover the development of the decay state and plan the conservation interventions the diagnostics and the microclimatic monitoring have been carried out.

2.2 METHODOLOGY AND INSTRUMENTS

Stone materials have been sampled in accordance with UNI EN 16085:2012 [18]; the salts present in the site have been taken in different zones and seasons (February, April and June). The nature of the sampled materials, their microstructure and composition have been investigated by different techniques as microscopic optics (with a polarized light microscope, Axioscop 40), SEM microscopy with a scanning electron microscope ZEISS EVO LS 15, equipped with a LaB6 filament, accompanied by a INCA microanalysis apparatus with a solid state detector X-Max 50 mm², powder X-ray diffraction analysis using a Rigaku Miniflex II diffractometer, operating with monochromatic beam of CuK α , 15 KV, 30 mA, ion-exchange chromatography with suppression (SIC - Suppressed Ion Chromatography, with instrument Metrohm 883) and by porosimetric analysis using a Micromeritics porosimeter mod. AutoPore IV 9500.

The microclimatic monitoring has been performed for a representative period, from February to June 2012 in order to investigate a cold, hot and intermediate season. It was carried out in accordance to UNI 10829:1999 [19] through eight miniaturized data logger. They have been positioned in different points inside the site (Fig. 1) in order to map the microclimatic conditions.

Tinytag ULTRA 2 allow to measure continuously the air temperature and relative humidity. The data loggers have been placed at least 1 meter from any source of direct radiation and they haven't been exposed directly to air

draughts. They constitute a fully integrated system with temperature sensors (thermistors NTC 10k) and relative humidity, signal conditioning, digitization and registration. The measuring range of sensors is -25°C - 85°C for temperature and 0% - 95% for relative humidity, with accuracy of $\pm 0.2^{\circ}\text{C}$ in the range between 0°C and 70°C and $\pm 3.0\%$ RH at 25°C for relative humidity. The data have been acquired every half of hour.

WST 800 climatic station has been also placed outside to monitor the external temperature and relative humidity every five minutes. This station have the temperature measuring range from -40 to $+65^{\circ}\text{C}$, accuracy $\pm 0,5^{\circ}\text{C}$, the relative humidity measuring range from 0% to 100%, accuracy 3 %.

The data from data loggers have been elaborated by statistical methods using a spreadsheet. Monthly and daily analyses have been carried out in order to understand the relative monthly and daily variations of temperature and moisture. Daily analyses have been carried out individuating the typical day for each month of monitoring and for each data logger by the statistics of Finkelstein-Shafer [20] in order to evaluate the daily maximum, minimum and range of temperature and relative humidity. For each data logger all data of temperature and relative humidity have been divided by month. A first empirical cumulative curve has been obtained using the average daily value of the temperature acquired for each month, for all month of the whole dataset, placing in increasing order these values and assigning an integer, defined rank, which represents the position of the value. The defined first cumulative distribution curve ΦT has been calculated by the following relationship:

$$\Phi T(T, m, i) = \frac{K(i)}{N + 1} \quad (1)$$

Where ΦT is a function of the temperature, p is the temperature, m is the month, i is the i -th value, $K(i)$ is the rank of the i -th value of the daily average of the considered month and N is the number of observations for each month. A second cumulative function FT was calculated for each day of the month using 48 value of temperature (1 measure for an half hour):

$$FT(T, d, m, i) = \frac{J(i)}{n + 1} \quad (2)$$

Where FT is the function of the temperature, p is the temperature, d is the day, m is the month, i is the i -th value, $J(i)$ is the rank of the i -th value of the daily average and n is the number of observations for each day.

Subsequently FST , the difference between ΦT and FT , for each day of each month, has been calculated:

$$FST = |\Phi T - FT| \quad (3)$$

$\Sigma iFST$, for each day of each month, has been then calculated. This procedure has carried out also for the parameter relative humidity, calculating ΦRH , FRH , $F SRH$ and $\Sigma iFSRH$. Then, ΣiFS total, the summation between $\Sigma iFST$ and $\Sigma iFSRH$, has been then calculated; the typical

day has been found calculating the minimum value of ΣiFS total. After that maximum, minimum and range of temperature and relative humidity have been calculated using spreadsheet.

Monthly analysis have been carried out drawing percentile curves of temperature and specific humidity for each data logger and for each month of monitoring. These curves allow to evaluate the evolution of the hourly temperature and specific humidity values during each month and their frequency inside each month. These curves have been drawn also for the outside trend to carry out a comparison between the outside environment and each monitored zone of the site and to evaluate the influence of the outside on the site. The SH (specific humidity) have been calculated from relative humidity values using [21]:

$$SH = 37,95 \times 10 \wedge \left(\frac{a \times T}{b + T} \right) \times \left(\frac{RH}{p} \right) (\text{g/kg}) \quad (4)$$

Where 37.95 is a constant, T is the temperature ($^{\circ}\text{C}$), a and b are two parameters from Magnus formula and $a = 7.5$ and $b = 73.15^{\circ}\text{C}$, RH is the relative humidity (%), p is the atmospheric pressure (mbar).

Finally the correlation between temperature and relative humidity values with the crystallisation points of the salts contaminating the structures has been carried out. The aim is to individuate the eventually dependence of the decay due to salt crystallisation of the structures from the microclimatic conditions of the site.

3 RESULTS AND DISCUSSION

The biomicritic limestone, which constitutes the walls, is porous, not very compact and easily alterable. The X-ray diffraction (XRD) has revealed the presence of calcite, accompanied by small impurities of quartz and rarer phyllosilicates. The lithotype most representative is the so-called "Pietra Cantone", a biomicritic limestone belonging to Cagliari Limestones formation [22]. The observation in optical microscope has shown the presence of abundant micritic cement binding allochemical components, consisting of fossilized remains of marine origin and clasts of variable size, ranging from about 0.1 to 0.6 mm (Fig. 4 a). The porosimetric analysis has revealed a high porosity (30-35%) with pores mainly concentrated in the range of 0.1-5.0 μm . However, there are pores with $r > 5.0 \mu\text{m}$ and, to a minor extent, pores with $r < 0.1 \mu\text{m}$ (Fig. 4 b).

In this lithotype it is possible to recognize different forms of decay such as biological colonization and, in particular, efflorescence and cryptoefflorescence. XRD revealed the nature of the salts contaminating the archaeological structures and the modern concrete. Sodium sulphate, is the most widespread in the site (Fig. 5) and the anhydrous form has been detected especially in summer and the hydrated one in winter. However, there are also chlorides and nitrates underlined by chromatographic technique and gypsum and syngenite detected by XRD technique.

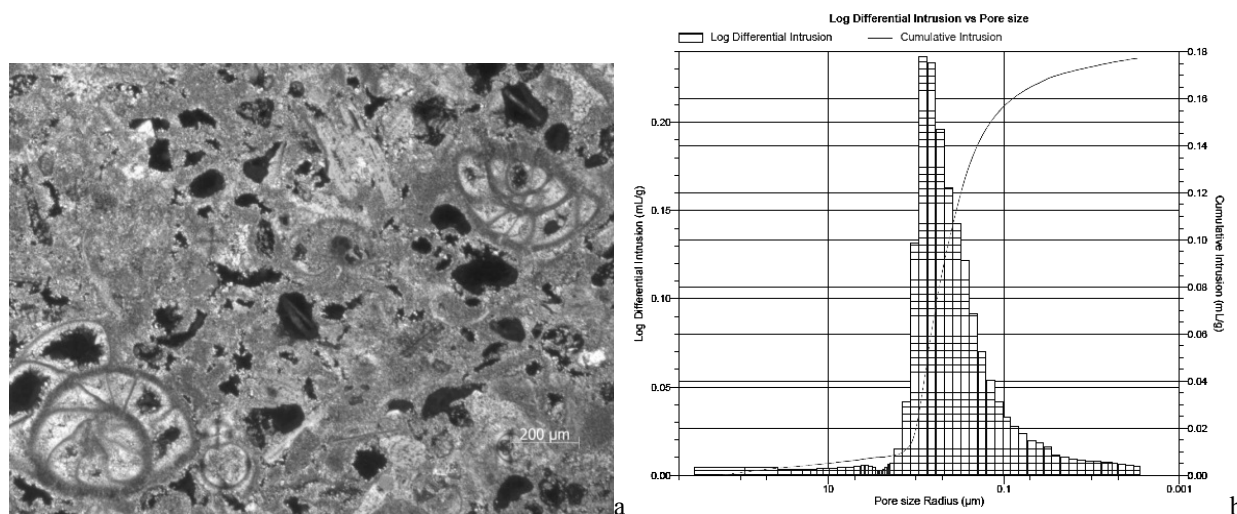


Figure 4 a Optical image of a biomicritic fragment sampled from the walls (Nicols X); b pores size distribution of Pietra Cantone.

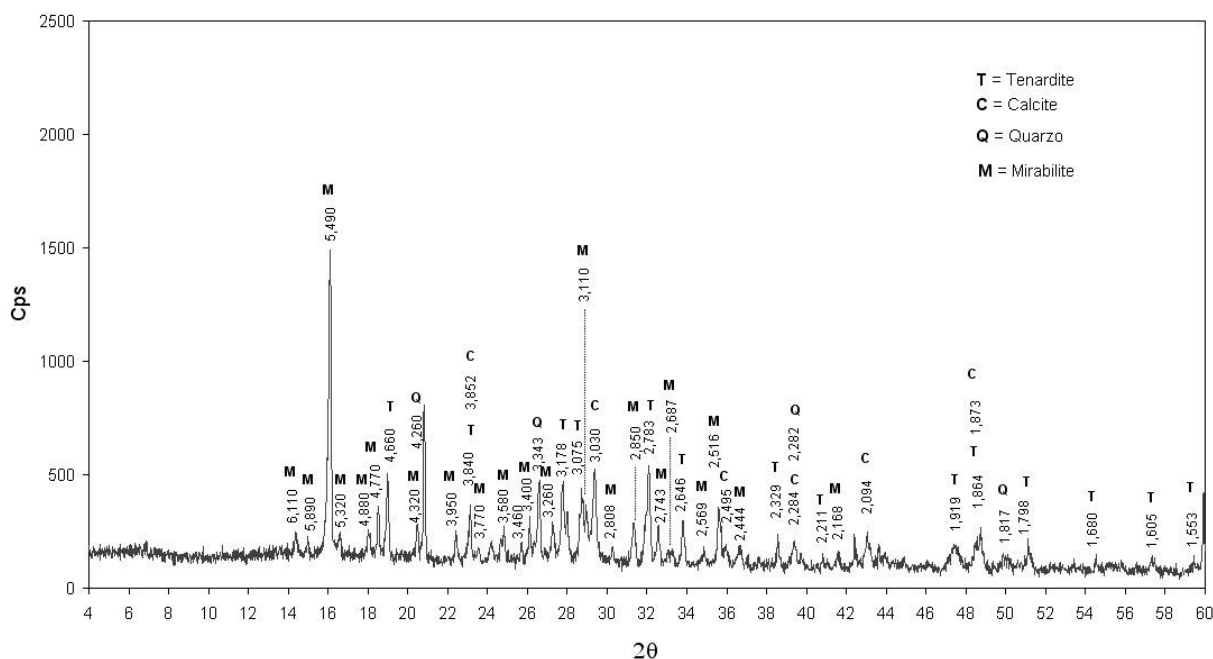


Figure 5 XRD Spectrum of saline efflorescence.

The microclimatic monitoring has revealed high values of relative humidity during all acquisition periods. The whole dataset has shown a microclimatic zoning within the site. Two main zones can be individuated (Fig. 1):

-Zone 1: values of temperature and relative humidity very similar to the outside.

-Zone 2: high thermal and hygrometric inertia and very high values of relative humidity(80-100%) in all the season. The typical day for each month and for each data logger has been evaluated through the methodology presented in 2.2. In table I the list of the typical day for each zone has been reported.

The typical day for the zone 1 and 2 has been used to individuate the temperature and relative humidity range for the two zones and the differences between them.

From the table II and III it is possible to observed that in February and June the zone 1 has a great fluctuation of the maximum and minimum values of temperature and relative humidity; instead in the zone 2 there is a greater thermal and hygrometric inertia than zone 1. From the observation of the percentiles (Fig. 6, 7, 8) appears that the zone 1 have a very similar trend of temperature to the outside: both of them shows two inflection point of percentiles in February; a negative inflection from 4:00 to 8:00, and a positive inflection from 12:00 to 18:00. Instead in the zone 2 the inflection point is just outlined and it is possible to observe a flatten curve, almost horizontal.

Table I List of the typical day for each month of each zone.

Data logger	Typical day				
	February	March	April	May	June
ZONE 1	16/02/2012	13/03/2012	21/04/2012	05/05/2012	12/06/2012
ZONE 2	17/02/2012	13/03/2012	21/04/2012	05/05/2012	18/06/2012

Table II Maximum, minimum and daily range of temperature and relative humidity referred to the typical day of February calculated for each zone.

ZONE NAME	FEBRUARY					
	T _{max} (°C)	T _{min} (°C)	T _{daily range} (°C)	RH _{max} (%)	RH _{min} (%)	RH _{daily range} (%)
ZONE 1	7,3	2,3	5,0	78	44	35
ZONE 2	9,2	7,8	1,4	92	79	13

Table III Maximum, minimum and daily range of temperature and relative humidity referred to the typical day of June calculated for each zone.

ZONE NAME	JUNE					
	T _{max} (°C)	T _{min} (°C)	T _{daily range} (°C)	RH _{max} (%)	RH _{min} (%)	RH _{daily range} (%)
ZONE 1	26,6	21,8	4,8	74	40	35
ZONE 2	23,0	21,4	1,5	98	86	12

In summer for outside and zone1 the percentile curves move to values of temperature higher than winter (Fig. 6, 7) and the inflection points appear shifted in the upper part of the diagram; instead the zone 2 shows the same flatten curve than winter (Fig. 8). The observation of specific humidity percentiles shows greater values of zone 2 SH than outside and zone 2, both in

winter and in summer (Fig. 9, 10, 11). However in winter the three zone have similar trend and the inflection point are at the same hours than inflection point of temperature, but they are less evident than temperature percentile inflection. In summer the inflection points are more evident than winter for the three zones and the zone 2 have the highest values of SH.

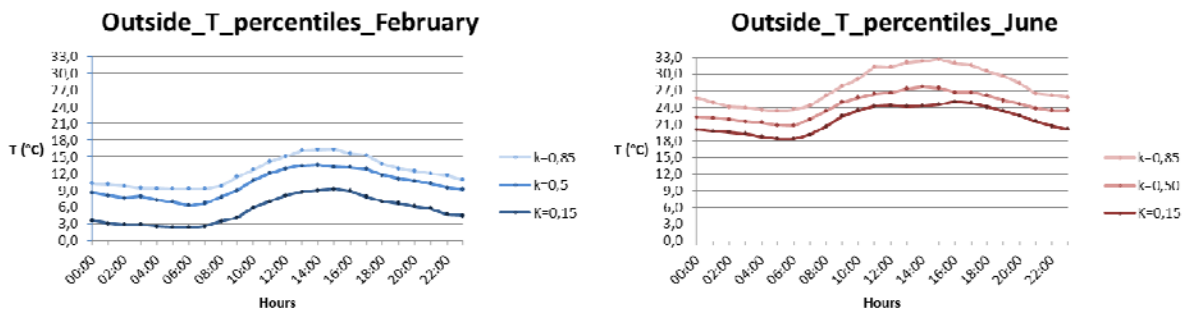


Figure 6 Temperature percentiles of February and June for outside.

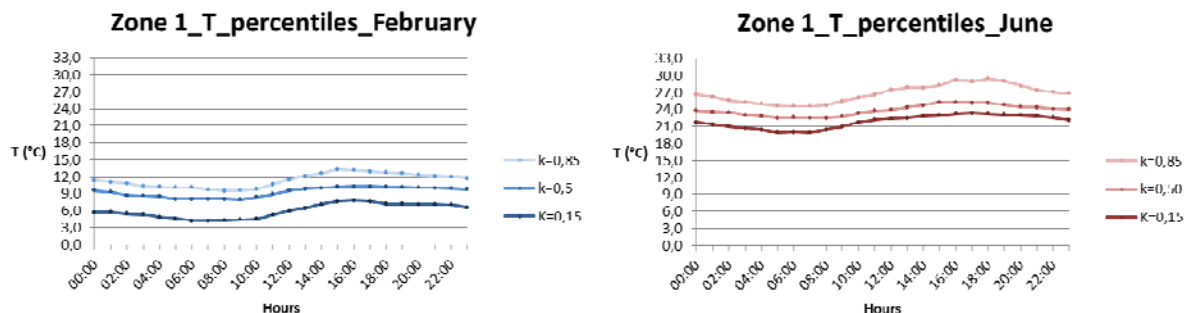


Figure 7 Temperature percentiles of February and June for zone 1.

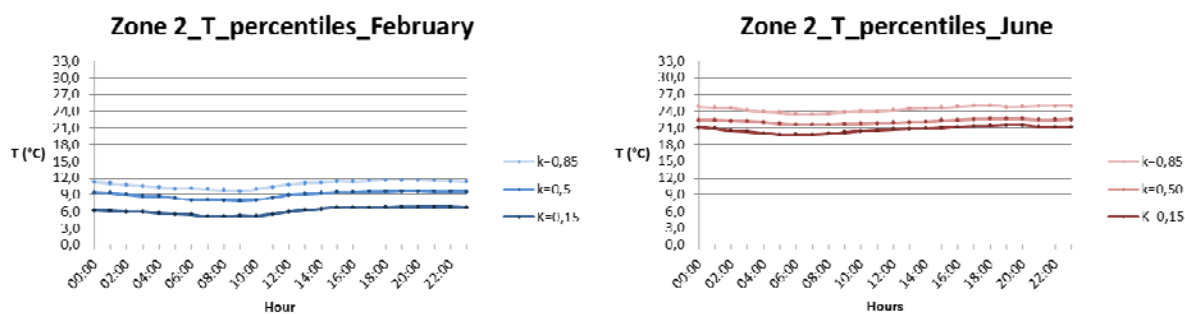


Figure 8 Temperature percentiles of February and June for zone 2.

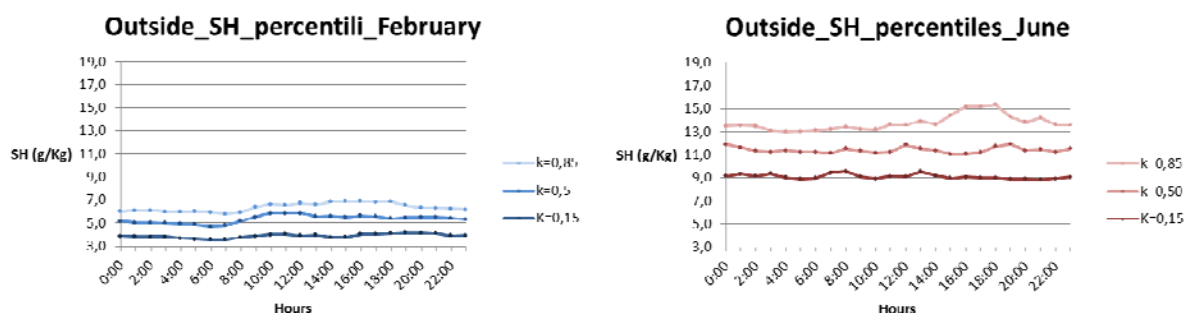


Figure 9 Specific humidity percentiles of February and June for outside.

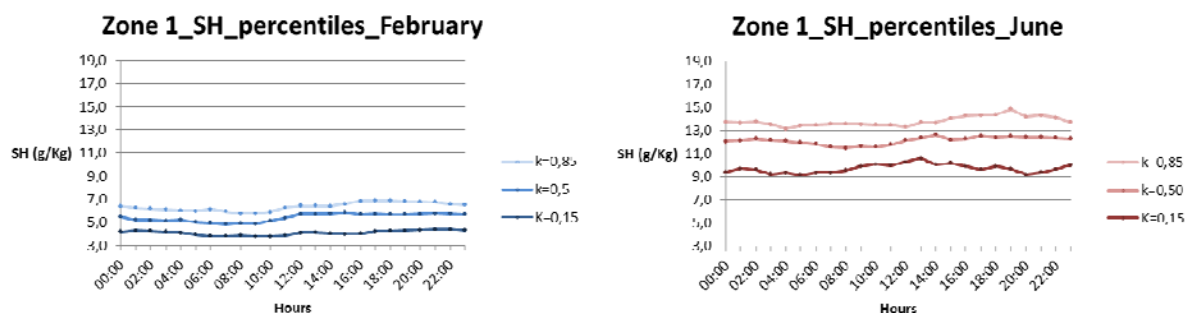


Figure 10 Specific humidity percentiles of February and June for zone 1.

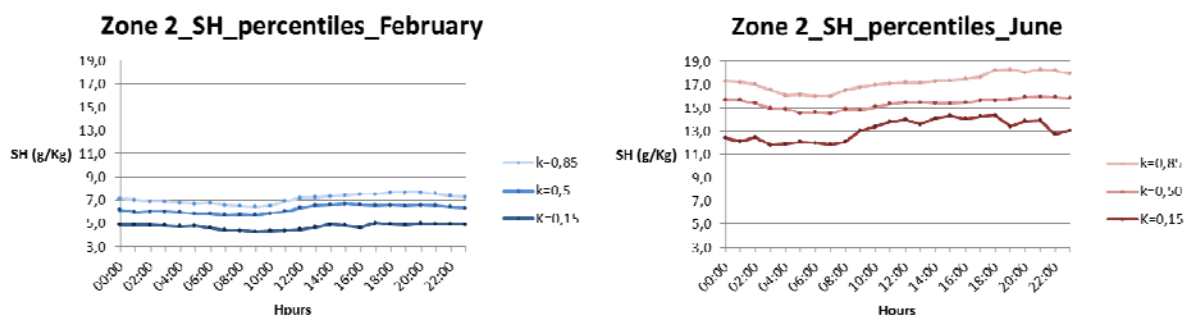


Figure 11 Specific humidity percentiles of February and June for zone 2.

The comparison between the 2 microclimatic zones coincides with the differential decay observed in the site:

-Zone 1 copious phenomena of pulverization and detachment.

-Zone 2 only efflorescences.

Because air temperature and the relative humidity values strongly influence the crystallization of soluble salts [8] it is possible to suppose that the differential decay of the

structures depends from the microclimatic zoning. The phase diagram of sodium sulphate reveals that the anhydrous phase Na_2SO_4 (thenardite) precipitates directly from a solution over 32.4°C and a relative humidity value of 84% while the hydrates phase $\text{Na}_2\text{SO}_4 \cdot 10\text{H}_2\text{O}$ (mirabilite) under 32.4°C and 84% as regards the relative humidity (Fig. 12).

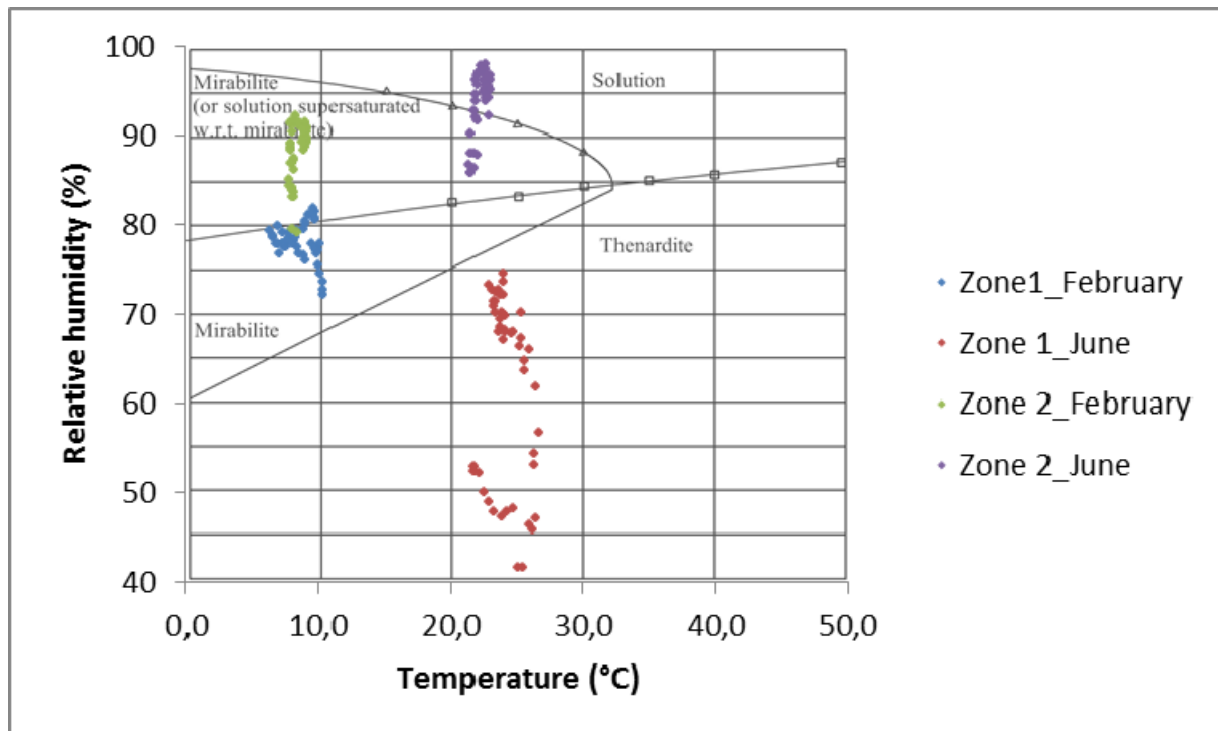


Figure 12 Phase diagram for sodium sulphate. The continuous lines indicate the boundaries of the stable phases. Triangles and squares are experimental data for mirabilite and thenardite, respectively [16]. The coloured points are the superimposed couple of temperature and humidity for each zone from February and June typical day.

According to the phase diagram of sodium sulphate, can be deduced that the hygrothermal values measured in the site are such as to favour practically always the crystallization of either phase (Fig. 12). The formation of mirabilite is favoured in the cold months when high relative humidity (average values ranging between 75% and 87%) and low temperatures (average values around 9 °C) can be found. The formation of thenardite is favoured in the warmer months in which lowest relative humidity (average values between 65% and 92%) and higher temperatures (average values between 22 °C and 24 °C) can be observed. Sometimes, in more confined areas (zone 2), the high relative humidity values are such as to inhibit the crystallization of the salt which remains in solution; for example, in the summer month a relative humidity of 99% and a temperature of 20 °C is often measured, values for which the sodium sulphate remains in the state of deliquescence. Furthermore also when it is possible the crystallisation of the salt the relative humidity is so high to allow the crystallisation as efflorescences and it could explain the less intense decay of the structures localised in this zone.

In the zone 1 the greater ventilation could increase the evaporation rate favouring the crystallisation of sodium sulphate as cryptoefflorescences [10, 11]. In this zone frequent fluctuation of temperature and relative humidity could also allow frequent phase transition also in a only day (table II and III) with great damage for the structures. However, inside the pores of the stone, the hygrothermal conditions can be different from the air conditions and,

inside a support rich in defect (i.e. porous materials), the hygrothermal conditions that influence the formation of a specific phase of salt can be modified respect those termodinamic [9, 15]. Nevertheless This hypothesis is confirmed by surveys carried out in different periods of the year. During the hottest periods there have been a reduction in the thickness of the salt deposits due to hot winds particularly present around the structures closest to the openings. Instead, in the most confined areas, efflorescences have been rather abundant in all periods of the year.

CONCLUSIONS

Semi-confined environment can be dangerous for the conservation of cultural heritage. In the archaeological structures of Viale Trieste 105 in Cagliari the alarming decay state evolve in a differential way with intense phenomena of pulverisation and detachments of the limestone stones composing the structures in the zones closest to the openings and only efflorescences in the most confined ones. Saline efflorescence results depending from the decay of cement materials that constitute the floor. They are the most harmful decay form because they can crystallise inside the pores of the stone as cryptoefflorescences breaking it. A multidisciplinary approach has been purposed to investigate the decay phenomena and individuate the correlation between salt crystallisation and the microclimatic condition in order to elaborate a solution for the conservation of the structures.

The microclimatic monitoring has revealed high values of relative humidity during all acquisition periods. The whole dataset has shown a microclimatic zoning within the site: the zone closest to the openings has values of temperature and relative humidity very similar to the outside, the most confined one has high thermal and hygrometric inertia and very high values of relative humidity (80-100%) in all the season. The zone closest to the openings corresponds to the most copious phenomena of pulverization and detachment, the most confined one to the zones with only efflorescences. Because air temperature and the relative humidity values strongly influence the crystallization of soluble salts it is possible to suppose that the differential decay of the structures depends from the microclimatic zoning. In the zones most confined the high relative humidity values are such as to inhibit the crystallization of the salt which, however, remains in solution; when it is possible the crystallisation of the salt the relative humidity is so high to allow the crystallisation as efflorescences and it could explain the less intense decay of the structures localised in this zone. In the zone closest to the openings the greater ventilation could increase the evaporation rate favouring the crystallisation of sodium sulphate as cryptoefflorescences explaining the greatest damage of these structures. In this zone frequent fluctuation of temperature and relative humidity could also allow frequent phase transition also in a only day with great stress for the structures.

This hypothesis is confirmed by surveys carried out in different periods of the year. During the hottest periods there have been a reduction in the thickness of the salt deposits due to hot winds particularly present around the structures closest to the openings. Instead, in the most confined areas, efflorescences are rather abundant in all periods of the year.

REFERENCES

- [1] Stanley-Price N. P., Jokilehto J., *The decision to shelter archaeological sites. Three case-studies from Sicily*, Conservation and Management of Archaeological Sites, Vol. 5, 19-34, (2001).
- [2] Meli P., *Teatro greco di Eraclea Minoa: gli studi propedeutici all'intervento di restauro, I beni culturali: tutela e valorizzazione*, Vol. 4, No. 6, pp. 14-19, 1996.
- [3] Camuffo D., Bernardi A. , *Deposition of urban pollution on the Ara Pacis, Rome*, The Science of The Total Environment, Vol. 189/190, pp. 235-245, 1996.
- [4] Becherini F., Bernardi A., Frassoldati E., *Microclimate inside a semi-confined environment: Valuation of suitability for the conservation of heritage materials*, Journal of Cultural Heritage , Vol. 11, pp. 471-476, 2010.
- [5] Camuffo D., *Microclimate and Deposition*, in: La pietra dei monumenti in ambiente fisico e culturale, 1st edition, Edipuglia, Bari, 1997, pp. 37-48.
- [6] Camuffo D., Del Monte M., Sabbioni C., *Influenza delle precipitazioni e della condensazione sul degrado superficiale dei monumenti in marmo e calcare*, in: Ministero Beni Culturali ed Ambientali "Materiali Lapidari", special issue of Bollettino d'arte, 1st edition, Istituto poligrafico e Zecca dello Stato P.V., Roma, 1987, pp. 15-36.
- [7] Camuffo D., *Microclimate for cultural Heritage*, 1st edition, Elsevier Science Amsterdam, 1998.
- [8] Arnold A., Zehnder K., *Salt weathering on monuments*, in: Atti del 1 Simposio la conservazione dei monumenti nel bacino del Mediterraneo, Bari 1989, Grafo, Brescia, 1989, pp. 31-58.
- [9] Camuffo D., *Physical weathering of stones*, The Science of the Total Environment, Vol. 167, pp. 1-14, 1995.
- [10] Scherer GW., *Stress from crystallization of salt*, Cement and Concrete Research, Vol. 34, pp. 1613-1624, 2004.
- [11] Massidda L., Sanna U., *La cristallizzazione salina nei materiali da costruzione*, Enco Journal, Vol. 14, pp. 8-9, 2001.
- [12] Everett D.H., *The Thermodynamics of Frost Damage to Porous Solids*, Transactions of the Faraday Society, Vol. 57, pp. 1541-1551, 1961.
- [13] Secco M., Stievanin E., Da Porto F., Modena C., Artioli G., Mazzoli C., *Non destructive and medium destructive analyses on an early 20th century, reinforced concrete structure: the case study of the Victory Monument in Bolzano*, in: Proceedings of the 10th International Conference on non-destructive investigations and microanalysis for the diagnostics and conservation of cultural and environmental heritage – , Firenze 13-15 April 2011, ART '11, CD proceeding NDT21, 2011.
- [14] Thaulow N., Shau S., *Mechanism of concrete deterioration due to salt crystallization*, Materials Characterization, Vol. 53, pp. 123-127, 2004.
- [15] Rodriguez Navarro C. , Doehne E. , Sebastian E. , *How does sodium sulfate crystallize? Implication for the decay and testing of building materials*, Cement and Concrete Research, Vol 30, pp. 1527-1534, 2000.
- [16] Tsui N. , Flatt R. J. , Scherer G. W. , *Crystallization damage by sodium sulphate*, Journal of Cultural Heritage, Vol. 2, pp. 109-115, 2003.
- [17] Montgiu M. A. , *Archeologia urbana a Cagliari: l'area di Viale Trieste 105*, in: Quaderni, 1st edition, Cagliari, STEF, 1987, 4 (II), pp. 51-78.
- [18] UNI EN 16085:2012 Conservation of Cultural property - Methodology for sampling from materials of cultural property - General rules.
- [19] UNI 10829:1999 Works of arts of historical importance – Ambient conditions for conservation – Measurement and analysis.
- [20] EN ISO 15927-4:2005 Hygrothermal performance of buildings - Calculation and presentation of climatic

data - Part 4: Hourly data for assessing the annual energy use for heating and cooling.

- [21] Bernardi A., Conservare opera d'arte. Il microclima negli ambienti museali, 1st edition, il Prato, Saonara, 2004.
- [22] Various authors, *Foglio 557, Cagliari*, in : Carta geologica d'Italia alla scala 1:50.000, S.EL.CA, Firenze, 2005, pp. 98-105.

NOMENCLATURE

T	temperature (°C)	N	number of observations for each day
RH	relative humidity (%)	FS_T	difference between Φ_T and F_T
Φ_T	cumulative distribution function of T within each individual month	$\Sigma_i FS_T$	summation of FS_T for each day of each month
m	month	Φ_{RH}	cumulative distribution function of RH within each individual month
i	i -th value	F_{RH}	cumulative distribution function of RH within each individual day
$K(i)$	rank of the i -th value of the daily average of the considered month	FS_{RH}	difference between Φ_{RH} and F_{RH}
N	number of observations for each month	$\Sigma_i FS_{RH}$	summation of FS_{RH} for each day of each month
F_T	cumulative distribution function of T within each individual day	$\Sigma_i FS_{total}$	summation between $\Sigma_i FS_T$ and $\Sigma_i FS_{RH}$
d	day	SH	specific humidity (g/kg)
$J(i)$	rank of the i -th value of the daily average of the considered day	a	parameters from Magnus formula ($a = 7.5$)
		b	parameters from Magnus formula ($b = 273.15$ °C)
		p	atmospheric pressure (mbar)
		r	pore size radius (μm)
		T_{max}	maximum of temperature (°C)
		T_{min}	minimum of temperature (°C)
		$T_{daily\ range}$	daily range of temperature (°C)
		RH_{max}	maximum of relative humidity (%)
		$RH_{min}(\%)$	minimum of relative humidity
		$RH_{daily\ range}$	daily range of relative humidity (%)

PROPOSAL OF INNOVATIVE FLUID DYNAMIC NONLINEAR SERVOVALVE SYNTHETIC MODELS

Parid Alimhillaj

Lorenzo Borello

Matteo D. L. Dalla Vedova

Department of Mechanical and Aerospace Engineering, Politecnico di Torino, Torino, Italy
Corso Duca degli Abruzzi 24 – 10129 TORINO

ABSTRACT

The design of modern flight control systems involves the need of highly detailed models in order to analyse the specific components or subsystems; on the contrary more simple and synthetic models, nevertheless having an acceptable level of accuracy, are requested for the simulation of the dynamic behaviour of entire systems. Aims of the work is the development of some innovative synthetic fluid-dynamic servovalve models, characterized by a semi-empirical formulation, having the ability to take into account the effects of a variable supply pressure and of a leakage acting among the control ports connecting the valve to the motor element; to the purpose, five different models have been proposed and their behaviour has been compared to an highly detailed model one. The merits or demerits of the proposed models, related to their ability to properly describe the fluid-dynamic behaviour of the valve, are represented by the diagrams reporting their “characteristics” and by the simulations of a typical servomechanism obtained by their use.

Keywords: Fluid-dynamic, hydraulic, valve, simulation, synthetic model

1 INTRODUCTION

Today's flight control systems are characterized by a higher and higher number of more and more complex components; their conception have the purpose of accomplishing more and more severe requirements concerning performance and safety levels. From the design point of view it involves the need of highly detailed models in order to analyse the specific components or subsystems; on the contrary more simple and synthetic models, nevertheless having an acceptable level of accuracy, are requested for the simulation of the dynamic behaviour of entire systems, particularly in case of high workload regarding the computers when the monitoring duties must be performed. In fact the above mentioned synthetic models are particularly suited to the system monitoring software, usually employed both in ground and in flight operations.

This duty must be performed in real time, so requiring a high burden for the on board computers. The aforesaid considerations may be applied to the basic component of any proportional hydraulic control system, that is control valves, servovalves, etc.

2 AIMS OF THE WORK

Any fluid-dynamic control valve model falls into one of the two following categories:

- models having the controlled differential pressure acting on the motor as output;
- models having the controlled flow as output.

The former category describes the relationship between an output variable which is considered as the differential pressure imposed on the motor element and an input variable represented by the spool displacement, having as the feedback input the controlled flow through the motor element itself. This consideration is quite valid both in highly detailed models [1] and in the simplified ones, that are the subject of the present work.

The latter category of models, not considered in the present work, has the controlled flow as the output variable and the differential pressure as the feedback input, while the spool displacement is still retained as the main input variable.

Contact author: Borello¹, Dalla Vedova²

¹Email: lorenzo.borello@polito.it

²Email: matteo.dallavedova@polito.it

Corso Duca degli Abruzzi, 24 – 10129 Torino, Italy

The most commonly used synthetic model can be generally represented by the fully linear arrangement as in Fig. 1: the differential pressure acting on the motor element is proportional to the spool displacement through the pressure gain of the valve, reduced by the value of the pressure losses related to the controlled flow through the pressure/flow gain ratio. The typical shortcoming of this model is represented by its inability to take correctly into account the effects of the supply pressure limits and, therefore, of the actual stall conditions of the motor element.

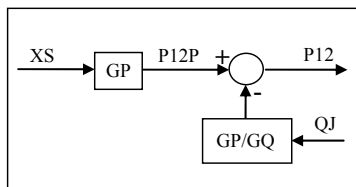


Figure 1

A possible variant derived from the previously described model is reported in Fig. 2: it consists of the implementation of a saturation block acting on the differential pressure developed through the related gain. This improving measure is able to compute, in some way, the effects of the differential pressure limits due to the hydraulic power supply; it must be noted that the so described simple measure has a severe shortcoming, represented by the underestimation of the actuation rate in case of a fully open valve, particularly noticeable when a large portion of the spool stroke concerns the saturation condition.

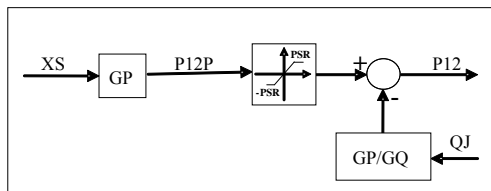


Figure 2

In a previous work, issued in Italian language [2], further models was developed starting from the above mentioned ones, in order to take into account in a better way the problem of the differential pressure limits connected to the hydraulic power supply. Nevertheless all the previously considered models have the same shortcomings regarding leakages and variable pressure supply, as described below.

Aims of the work is the improvement of some previously seen models into a more synthetic formulation, having the ability to take into account the effects of a variable supply pressure and of a leakage acting among the control ports connecting the valve to the motor element. In fact, from the computational point of view, the variation of the hydraulic power supply differential pressure, affects both pressure and flow gains, besides the direct action on the pressure limits.

Further, the simulation of the aforesaid leakage usually involves an instantaneous feedback loop, affected by consequent numerical instabilities and related computational troubles. This work suggests a possible solution to all these problems on the basis of some considerations explained as follows. Taking into account all the above mentioned matters, a computational algorithm is performed for each considered model, having the merit of solving all the problems connected both with the variable values of pressure and flow gains and with the possible numerical instabilities of the leakage simulation. The algorithm is developed both in low level computational languages (FORTRAN, C, etc.) and in high level ones as, for example, MATLAB-SIMULINK. These algorithms, applied to the FORTRAN and SIMULINK languages, perform both the diagrams reporting the fluid-dynamic characteristics of the valve and the simulations of the dynamic behaviour of a typical hydraulic system, so proving the model abilities, by comparing them with those given by a detailed numerical model [1], previously published by the authors. In conclusion, the present work analyses merits and demerits of the proposed numerical models. The abovementioned comparisons have been carried out by means of the corresponding performance's diagrams and also by means of dynamic simulations of an actuation system in which the aforesaid servovalve is coupled to a linear jack with relative aerodynamic control surface. Fig. 3 shows the typical diagram of the four ways valve to which the job refers, while Fig. 4 represents the layout of the above-mentioned complete actuation system.

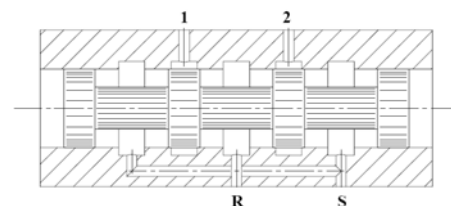


Figure 3 – Four ways valve's schematic

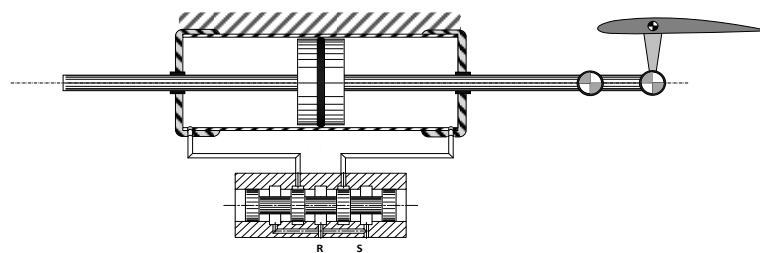


Figure 4 – Schematic of the hydraulic actuation device

3 SIMPLIFIED NUMERICAL MODELS

The new approach to all the simplified models, as they are presented in this work, takes into account the effects of the variable values of the supply/return differential pressure performed by the hydraulic system, reported as PSR: to this purpose, it must be noted that the effect of PSR on both pressure (GP) and flow (GQ) gain amounts can be computed in a reasonable but simple form by considering the general layout of the models, which is as linear as possible and, consequently, is conceived around the acceptable hypothesis of a linear relationship between each considered gain and the value of PSR. The actual values of GP are sufficiently close to the proportionality with respect to PSR, but the actual values of GQ are more and more close to the proportionality with the square root of PSR.

As a consequence, the assumption concerning the proportionality between GQ and PSR is not so realistic, nevertheless it is accepted as a valid hypothesis because it is consistent with the general linear layout of the considered models. As a consequence of this assumption the pressure to flow gain ratio (GP/GQ) can be considered independent on the value of PSR and the same can be said for the particular value of the generic spool displacement XS at which the differential pressure produced on the motor element in zero-flow condition P12P is equal to PSR, reported as XSS.

According to these assumptions, the value of P12P can be computed dividing XS by XSS and multiplying it by the value assumed by PSR in the present situation, as shown in fig. 8; further, the pressure to flow gain ratio GP/GQ can be replaced by GPQ, characterized by its invariant value with respect to PSR.

Regarding the leakage model and related computational algorithm, the following considerations are necessary. The leakages taken into account by the proposed models are all those developing an amount of flow through the control passageways of the valve: in fact, usually, the flow controlled by the valve passageways and driven to the ports 1 and 2 (fig.3) mainly operates across and within the motor element displacing a proper volume and developing mechanical power, but a small amount of it passes through imperfect seals or intentional bypass devices (based on suitable small orifices) directly from port 1 to 2 or vice versa, so being unable to perform any useful work; nevertheless it produces further pressure losses across the valve passageways, besides those developed by the operating flow. According to the very small dimensions and related flow QLk of the leakage passages, it is often sufficiently realistic and suited to an essentially linear model to state a linear relationship between the differential pressure P12 and the consequent drained flow QLk, as reported in the following relationship $QLk = CLK \cdot P12$, through the leakage coefficient CLK.

As a consequence, the leakage effects can be properly represented by the feedback loop containing the CLK block, as in fig.5, in which CLK is the ratio between the leakage flow and the differential pressure P12, being its cause.

The leakage flow QLk, added to the working one QJ, gives the total flow crossing the valve control passageways and the related differential pressure loss is obtained, multiplying it by GPQ = GP/GQ (pressure/flow gain ratio).

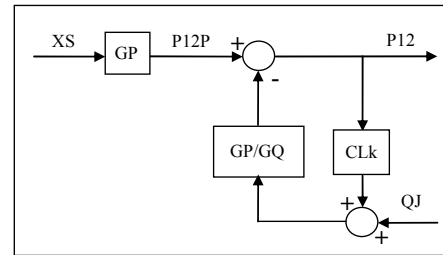


Figure 5 – Linear model able to take in account the servovalve leakage

In this formulation the computational structure is characterized by a numerical shortcoming: in fact, the leakage loop, as modified in fig.6, contains only instantaneous blocks and the related numerical instabilities are not quite avoidable.

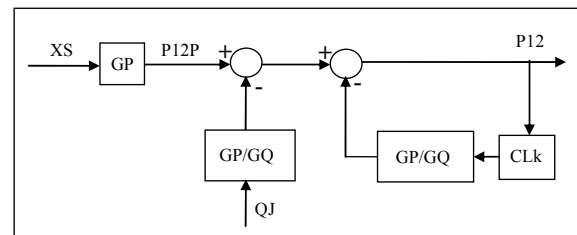


Figure 6 – Flow and leakage loop separation

As usual in these cases, the solution of the problem is possible by means of a different formulation of the computational algorithm, based on the preventive analytical solution of the instantaneous loop, as in fig.7, having no more troubles.

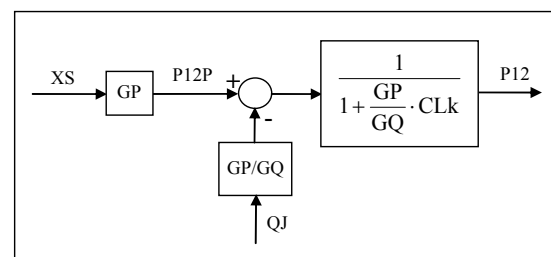


Figure 7 – Servovalve leakage loop solution

Therefore the final evolution of the completely linear standard model, taking into account both the leakage and the variable supply differential pressure PSR effects, is represented by the MODEL A, in fig.8.

Similar considerations can be done starting from the model reported in fig.2: the same modifications are introduced to take into account the effects of both the variable value of PSR and the leakage.

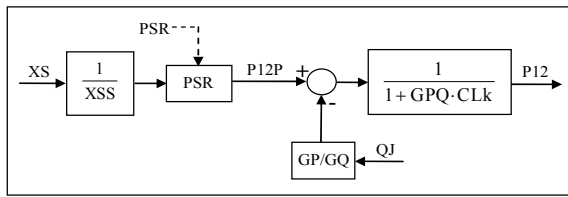


Figure 8 – MODEL A evolution able tom take in account leakage and variable supply pressure effects

The final arrangement of the so developed model is represented by the MODEL B of fig.9.

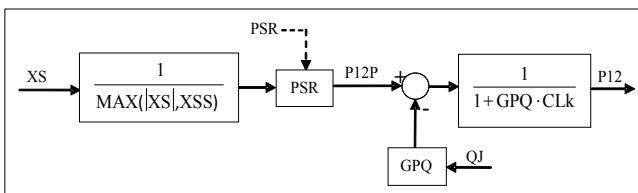


Figure 9 – MODEL B developed by Fig. 2 model

In the above mentioned previous work (bibl.[2]) a modified version of model 3 is reported as model 4; the difference consists of the new position assumed by the saturation block, which is displaced downstream the flow feedback, as it can be seen in fig. 10.

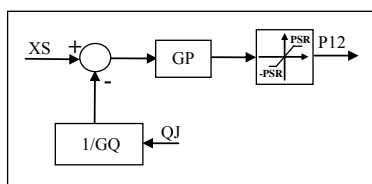


Figure 10

The advantage offered by this layout consists of the ability to take acceptably into account the effects of P12 limitations on the actuation rate, so obtaining a more proper value of the no-load actuation rate itself. On the contrary, the shortcoming of this model is represented by the inability to simulate the temporary overload conditions, eventually affecting the motor element. In this formulation the shortcoming is generally not considered so important, while the advantage regarding the acceptable evaluation of the actuation rate is seen as appreciable. Having a mind to the true purpose of these models, consisting of an arrangement between two opposite requirements, maximum simplicity with maximum computational accuracy, in this work several models and related algorithms are developed from model 4 of bibliography [2], having the ability to compute the effects of both the leakage and the variable value of PSR.

A possible development of the above mentioned model 4, including leakage and variable PSR computational algorithms, is reported in fig.11, in which, in order to employ the invariant GPQ block, the flow feedback sum block has been displaced downstream the GP one,

nevertheless being upstream the saturation block PSR. In this formulation the leakage loop is entirely located downstream the pressure saturation block, limited within the values \pm PSR. In order to compute the effects of the variable value of PSR, the model must be compliant not only with variable values of PSR along the simulation run, but also with the related variable values of pressure and flow gains, according to the above discussed assumption of proportionality between GP, GQ and PSR. Further, the leakage loop must be previously analytically solved in order to prevent any computational instability.

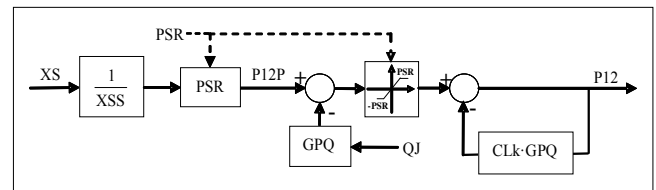


Figure 11 – MODEL C1 initial formulation

As a consequence, the final evolution of this model, similarly developed as the previous MODEL A, is reported in fig.12, as MODEL C1.

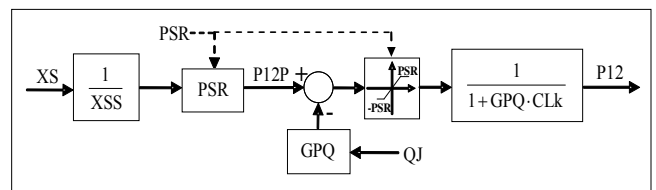


Figure 12 – MODEL C1 final formulation

Another development of model 4, including the same improvements described in fig. 11, is reported in fig. 13.

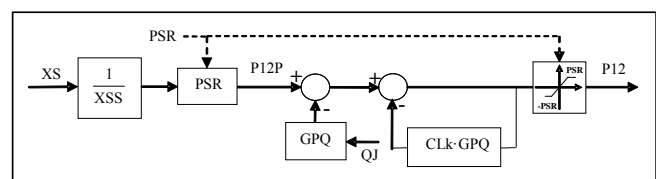


Figure 13 – MODEL C2 initial formulation

In this formulation the leakage loop is entirely located upstream the pressure saturation block, limited within the values \pm PSR. Developing the same considerations as above, the final evolution of this model is reported in fig. 14 as MODEL C2.

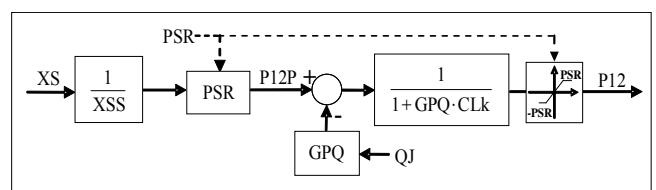


Figure 14 – MODEL C2 final formulation

Both MODEL C1 and C2 are characterized by possible shortcomings regarding the evaluation of the leakage effects in which the pressure gain contained in GPQ does not take into account the differential pressure saturation.

4 VALVE FLUID-DYNAMIC CHARACTERISTICS MODELLING AND RELATED RESULTS

According to each above considered mathematical model and related algorithm, a computational program performing the fluid-dynamic characteristics of the valve has been prepared.

The results given by this program consist of diagrams in which the differential pressure P12 acting on the motor element is computed, for each value of PSR and CLk, as a function of the valve spool displacement XS, having the flow QJ through the piston as a parameter.

All the following results are given for a valve geometrically characterized by the values of XSS=0.1 mm and GPQ=6.667*10¹¹ Pa*s/m³, independent on PSR, relating the values of GP or QJ and PSR each other.

In fig. 15 (MODEL A) the results concern the values of CLk=0 m³/s/Pa, GQ=0.3 m²/s, PSR=20 MPa, GP=2*10¹¹ Pa/m. The slope of the zero-flow curve is equal to the value of GP, because of the effect of CLk=0, as it appears correct, while no saturation is present, according to the model structure. Higher values of QJ refer to lower P12 ones, like expected, not only in the present case but also in the following, as a consequence of the sign assumptions.

In fig. 16 (MODEL A) the results concern the same values as before except for CLk=2*10⁻¹³ m³/s/Pa. The slope of the zero-flow curve is constant and lower than the value of GP, because of the effect of CLk>0, as it appears correct.

Fig. 17 (MODEL A) shows the results related to the same values of fig. 20 except for PSR=12 MPa. The slope of the zero-flow curve is further reduced because of the effects of both CLk>0 and low PSR.

Fig. 18 (MODEL B) reports the results concerning the values of CLk=2*10⁻¹³ m³/s/Pa, GQ=0.3 m²/s, PSR=20 MPa, GP=2*10¹¹ Pa/m. The slope of the zero-flow curve, in its central portion, is lower than the value of GP, because of the effect of CLk>0, as it appears correct.

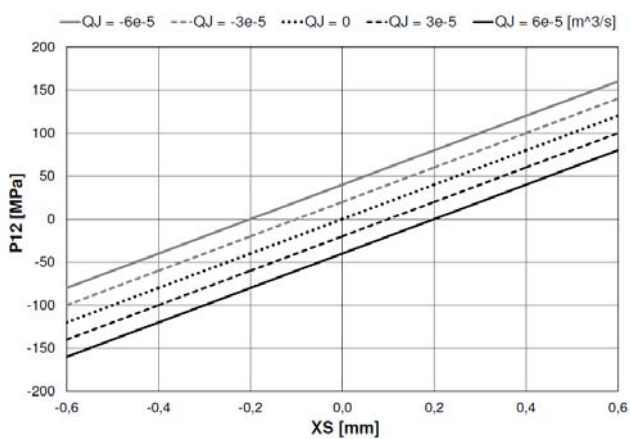


Figure 15

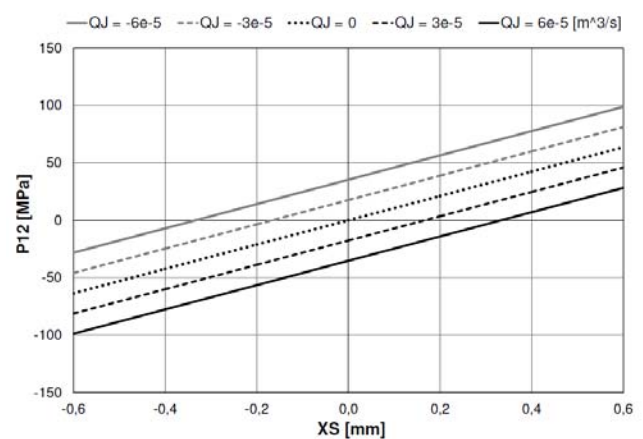


Figure 17

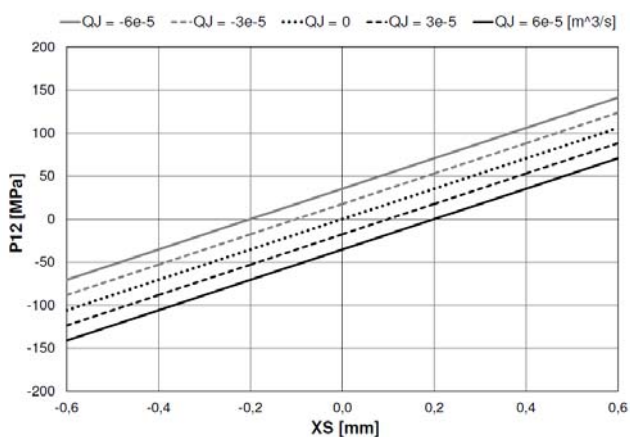


Figure 16

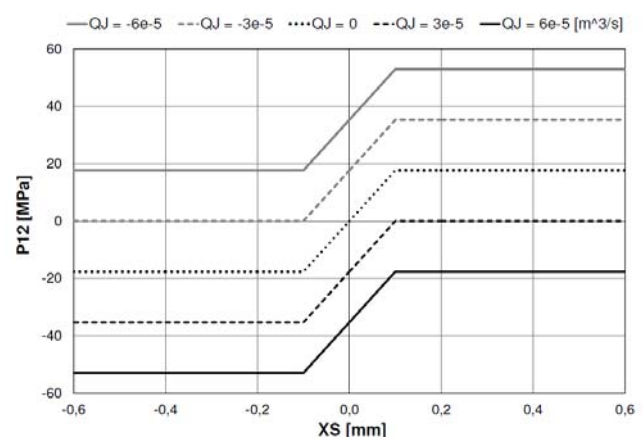


Figure 18

In fig. 19 (MODEL C1) the results concern the values of $CLk=0 \text{ m}^3/\text{s}/\text{Pa}$, $GQ=0.3 \text{ m}^2/\text{s}$, $PSR=20 \text{ MPa}$, $GP=2*10^{11} \text{ Pa}/\text{m}$. The slope of the zero-flow curve in its central portion, is equal to the value of GP , because of the effect of $CLk=0$. In saturation conditions, PSR is computed as invariant with respect to XS for all the values of QJ , as a consequence of the model structure. It represents the inability of the model to compute correctly the high values reached by PSR in case of “water hammer”, related to a sudden valve centring when the motor element is running quickly. As before, higher values of QJ refer to lower $P12$ ones.

In fig. 20 (MODEL C1) the results concern the same values as before, except for $CLk=2*10^{-13} \text{ m}^3/\text{s}/\text{Pa}$. The slope of the zero-flow curve, in its central portion, is lower than the value of GP , because of the effect of $CLk>0$, and the saturation value of $P12$, represented by PSR , cannot be reached, because the leakage block follows the saturation one, as reported in Fig. 12 (block diagram).

Fig. 21 (MODEL C1) shows the results related to the same values of fig. 20 except for $PSR=12 \text{ MPa}$. The slope of the zero-flow curve is further reduced because of the effects of both $CLk>0$ and low PSR . As in Fig. 20, the algorithm shows the inability of $P12$ to reach the PSR value in saturation condition; it can be considered as a shortcoming in certain conditions, partially solved in the following formulations.

In Fig. 22 (MODEL C2) the results regards the values of $CLk=0 \text{ m}^3/\text{s}/\text{Pa}$, $GQ =0.3 \text{ m}^2/\text{s}$, $PSR=20 \text{ MPa}$, $GP=2*10^{11} \text{ Pa}/\text{m}$. As it can be expected the layout of the diagram is the same as in Fig. 19, because the different algorithm architecture has no effect when $CLk=0 \text{ m}^3/\text{s}/\text{Pa}$; so, the same considerations, as in Fig. 19, can be done.

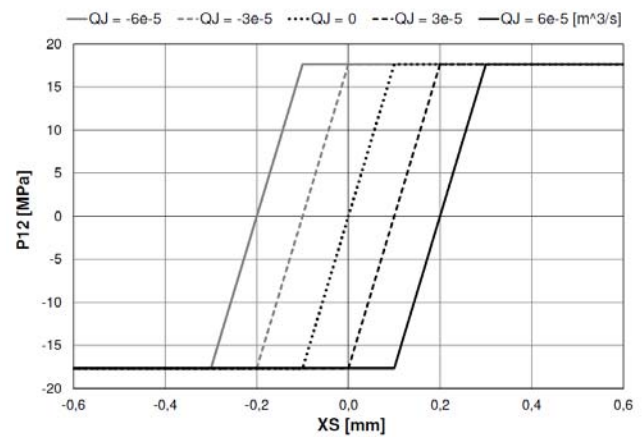


Figure 20

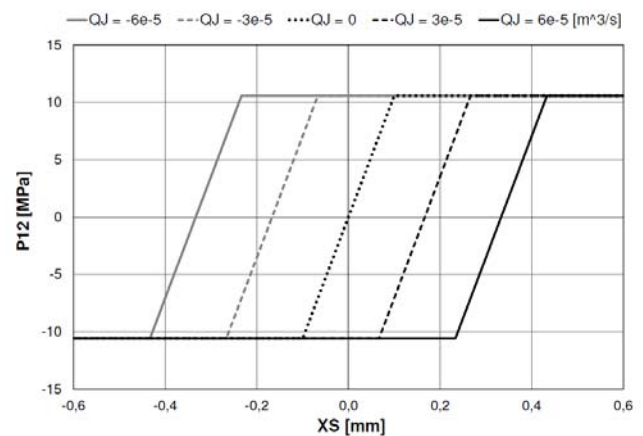


Figure 21

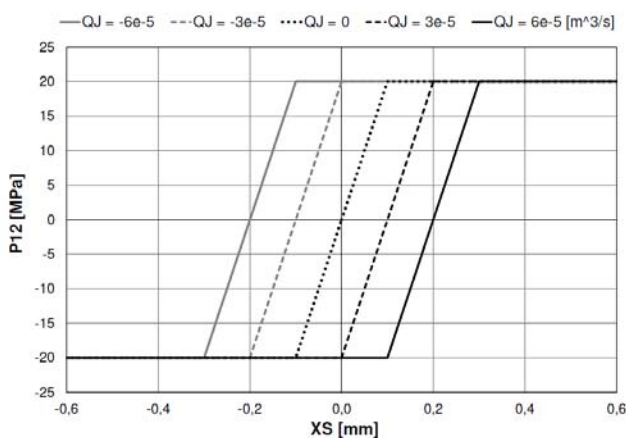


Figure 19

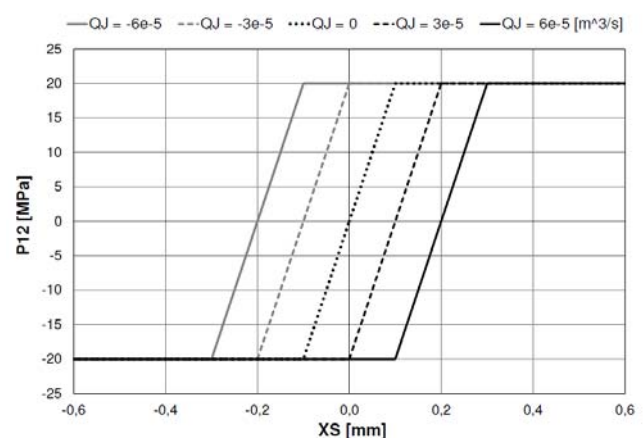


Figure 22

In Fig. 23 (MODEL C2) the results concern the same values as before, except for $CLk=2 \cdot 10^{-13} \text{ m}^3/\text{s}/\text{Pa}$. The slope of the zero-flow curve, in its central portion, is lower than the value of GP, because of the effect of $CLk>0$, but the saturation value of P12, represented by PSR, is correctly reached because the saturation block follows the leakage one, as in Fig. 14 (block diagram).

Fig. 24 (MODEL C2) shows the results related to the same values of Fig. 23 except for $PSR=12 \text{ MPa}$. The slope of the zero-flow curve is further reduced because of the effects of both $CLk>0$ and low PSR. As in Fig. 23 the saturation value of P12 can be correctly reached.

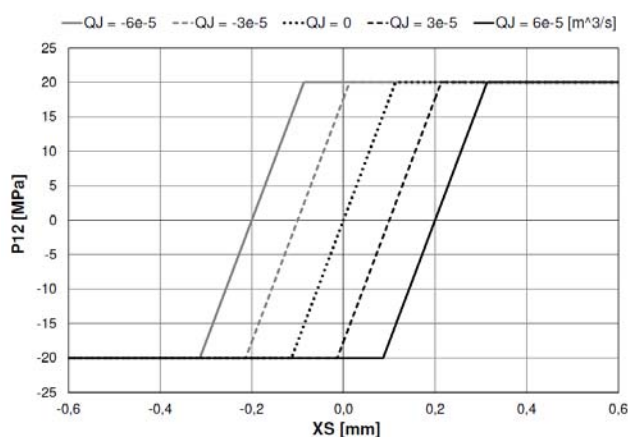


Figure 23

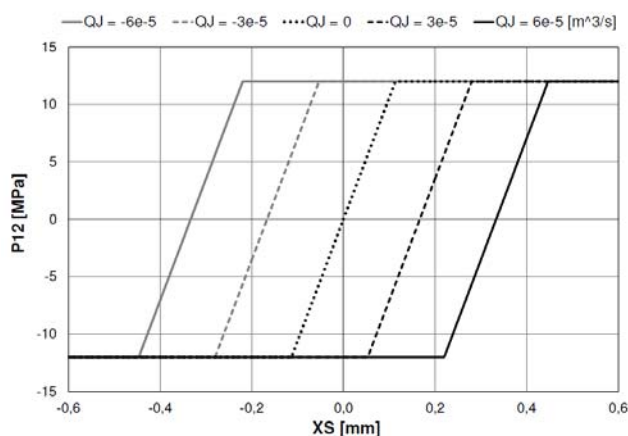


Figure 24

5 ACTUATION SERVO-SYSTEM MODELLING

In order to compare the behaviour of the different models and related computational algorithms concerning the fluid-dynamics of the control valve equipping a hydraulic actuation servomechanism, a typical system was considered. The schematic of such actuation system is shown in Fig. 4, in which the position transducer and related feedback control loop is not reported. The system mainly consists of a Power Control and Drive Unit (PCDU) and its control is performed by an Electronic Control Unit

(ECU), not shown in Fig. 4, closing the position control loop. The PCDU contains hydraulic piston, and control electro-hydraulic two stage servo-valve. The model takes into account the hydraulic and mechanical characteristics of all the system components which are relevant to the purpose.

In particular, the model is able to compute the following (bibl. [3]):

- inertia, viscous and eventual Coulomb friction regarding the hydraulic piston,
- third order electromechanical dynamic model of the servo-valve with first and second stage ends of travel and simplified fluid-dynamic model, containing the motor element internal leakage.

6 ACTUATION SERVO-SYSTEM SIMULATION RESULTS

Different simulations, reported in the present work as Figs. 25 to 28, have been run applying step inputs on the considered servomechanism; all the simulations concern the dynamic response of the abovementioned hydraulic servo-system to a defined time history of the three input quantities here considered, when the fluid-dynamic model of the SV spool is described by means of each different algorithm: MODEL A (Fig. 25), MODEL B (Fig. 26), MODEL C1 (Fig. 27) and MODEL C2 (Fig. 28). Further, a high definition spool fluid-dynamic algorithm, applied to the servo-system model, is reported in Fig. 29 (MODEL HD), for comparison purposes, been generally considered as an instrument able to perform accurate simulations.

The three input quantities are the position command Com, the load FR acting on the motor element and the supply/return differential pressure PSR. The time history applied to Com consists of a series of three step changes from 0 m (initial position) to 0.02 m at Time=0 s, to 0.03 m at 0.3 s, to 0.02 m at 0.75 s; only MODEL B is interested by a twin step command from 0 m (initial position) to 0.01 m at Time=0 s and back to 0.005 m at 0.7 s.

The time history of FR, having null value since 0 s to 0.2 s, reaches the final constant value (10400 N) through a step change at Time=0.2 s; so, the actuation run of the system following the first step command is unloaded, while FR acts as an opposing or aiding load during the second run (starting at Time=0.3 s) or the third one (Time=0.75 s and following) respectively.

The time history of PSR considers three time intervals, each characterised by a constant differential pressure value: during the first (Time since 0 s to 0.35 s) and the third (0.45 s to the end of simulation) time interval, the 20 MPa nominal value is kept as a constant (corresponding stall load $FR=14.1 \text{ kN}$), while during the second (0.35 to 0.45 s) time interval the constant 12 MPa reduced value (related stall load $FR=8.5 \text{ kN}$) is performed through two step changes. So, the effect of a temporary supply pressure drop, acting during the opposing load actuation run, is evaluated. All the above mentioned simulations (Figs. 25 to 28) have been run having the leakage coefficient $CLk=2 \cdot 10^{-13}$

$\text{m}^3/\text{s}/\text{Pa}$; the command (Com) and motor element position (XJ) are expressed in meters, the motor element velocity (DXJ) in dam/s , the spool displacement (XS) in dm , the pressures (PSR and P12) in 10^7 Pa and the load acting on the motor element (FR) in MN . Fig. 25 shows the dynamic behaviour of the system according to MODEL A, which can be compared with the high definition model of Fig. 29. The simulation of the unloaded actuation run is sufficiently accurate, notwithstanding higher starting accelerations and lower stopping decelerations, as shown by the differential pressure P12 acting on the motor. Similar considerations can be done in case of aiding load run, while the opposing load actuation travel shows a markedly different behaviour: according to MODEL A, the effect of the opposing load on the actuation rate is underestimated and, when the supply pressure drops, the system back movement is completely absent, as a consequence of the typical MODEL A inability to compute the correct P12 saturation value. In loaded and motionless conditions the spool displacement is correctly not null, according to GP value. Fig. 26 shows the dynamic behaviour of the system described by MODEL B, to be compared with MODEL HD. Typical severe shortcoming of MODEL B is represented by the underestimation of the actuation rate in large spool displacement conditions, due to the overestimation of the related damping action: in fact, when $\text{XS} > \text{XSS}$, MODEL B computes the same flow as $\text{XS} = \text{XSS}$, so acting as $\text{XSM} = \text{XSS}$. However, the evaluation of FR and PSR effects on the underestimated actuation rate seems to be more reasonable than in MODEL A. As a consequence, any other consideration is out of place and unnecessary. Figs. 27 and 28 present the dynamic behaviour of the system according to MODEL C1 and MODEL C2 respectively, in comparison with MODEL HD. Both the unloaded and the aiding load actuation runs are rather accurately simulated, in spite of lower stopping deceleration and slightly higher starting accelerations, as the P12 behaviour proves. The opposing load actuation travel reveals some significant discrepancy with respect to

MODEL HD: the load effect on the system actuation rate, in terms of reduction of the rate itself, is underestimated as in MODEL A and, when the supply pressure drops, the system back movement is overestimated, performing an incorrect constant back acceleration. Further, the acceleration following a spool displacement change keeps a constant value along a relevant part of the acceleration transient, rather than the much more plausible asymptotic trend, reported in MODEL HD, similar to a first order response which follows a step input; the reason lies on the simple, but partially unsatisfying action of the P12 saturation block, contained within the algorithms of Figs. 12 and 14. In these conditions, the results given by MODEL C1 and MODEL C2 are unreliable with respect to the surely more accurate MODEL HD ones, but the computational inaccuracies ascribable to MODEL C2, MODEL C1 are high and much higher respectively and are emphasized by increasing CLk values in MODEL C1. Similar considerations regard the stop following the aiding load run, performing an incorrectly delayed action. It proves the inability of MODEL C1 and MODEL C2 to take correctly into account the damping action related to the flow crossing the valve passageways, when load and deceleration require particularly high P12 value, eventually exceeding PSR. This improper behaviour depends upon the restrictions imposed to P12 level without regarding the specific system working condition; in fact, MODEL C2 limits the P12 amount within $\pm \text{PSR}$, whatever CLk value is, MODEL C1 limit P12 within $\pm \text{PSR}^*$, where PSR^* is as lower than PSR as CLk is high (PSR^* is to be intended as PSR reduced by leakage effect). In case of an actual system having the valve spool fully displaced, the stall load characterising the piston decreases as CLk grows and it is a valuable aspect of MODEL C1 with respect to MODEL C2, but, if an over-stall load is reached, the inability to perform properly high P12 levels represents a severe shortcoming, mainly for MODEL C1.

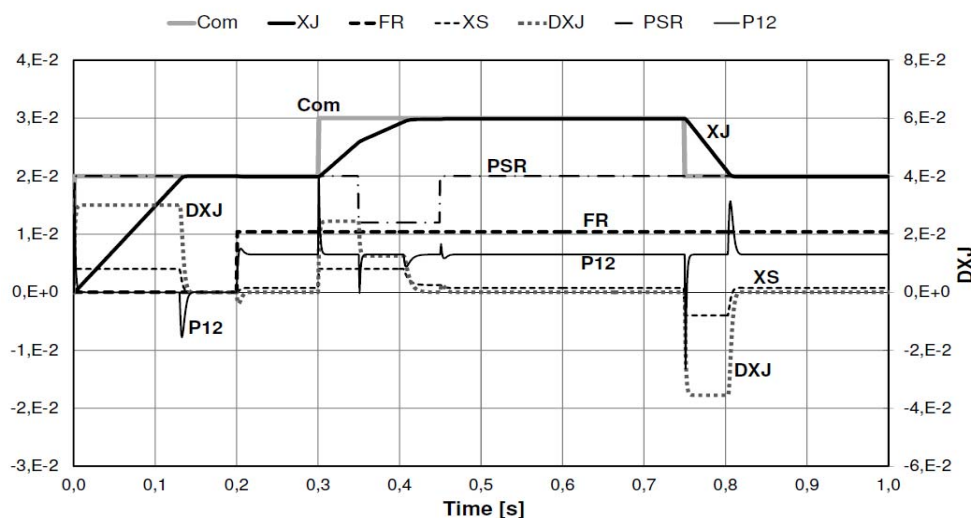


Figure 25

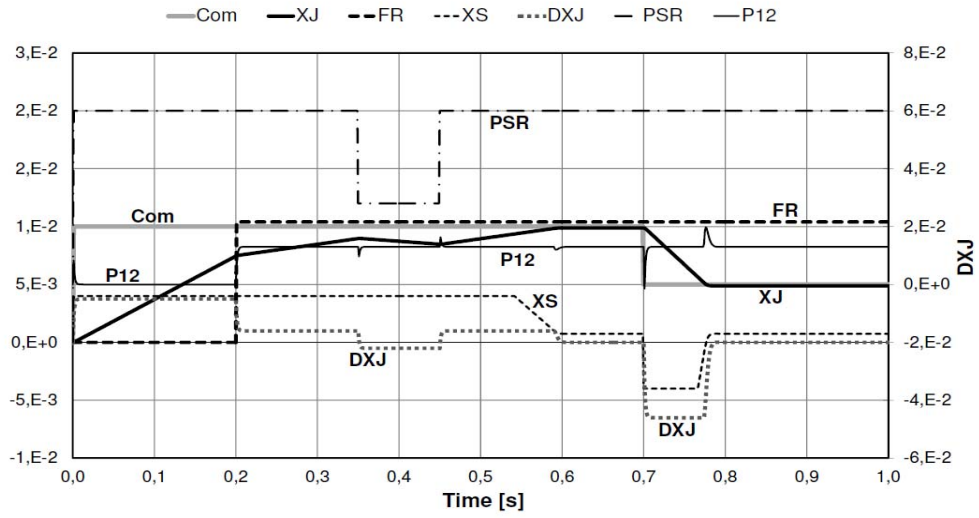


Figure 26

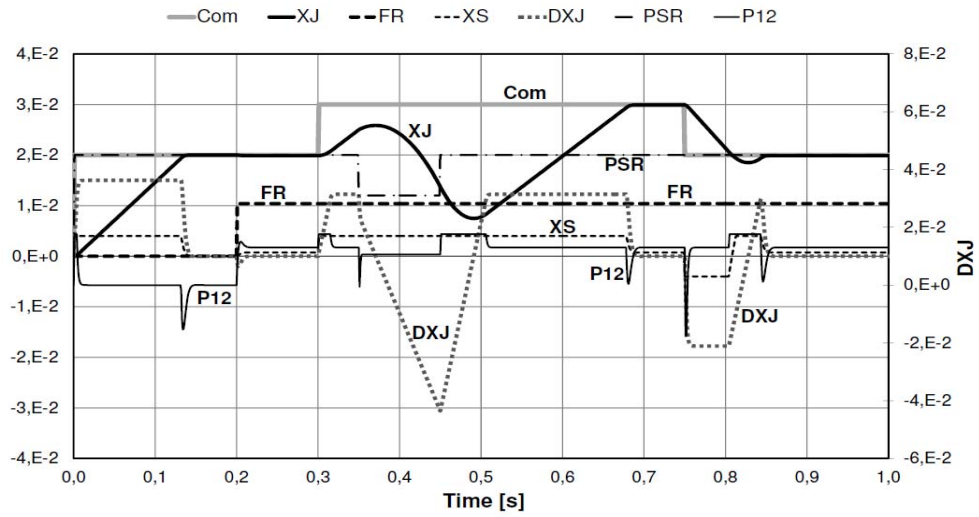


Figure 27

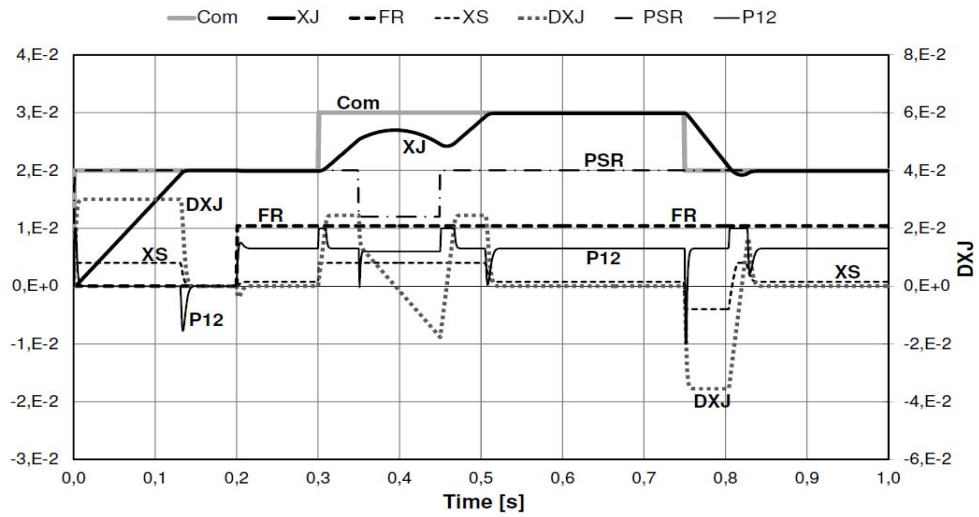


Figure 28

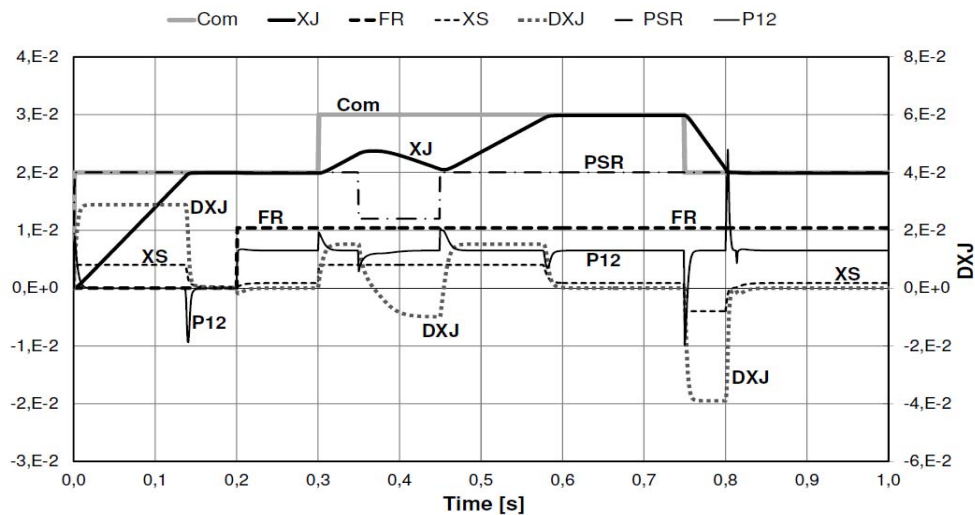


Figure 29

7 CONCLUSIONS

The analysis of the performance of the four different fluid dynamic models of control valve reported in the present work put in evidence their few merits and several deficiencies.

The evaluation of transients (accelerations, decelerations) is more or less deficient (over- or under-estimated) in all the models. The simulation of both the unloaded and aiding loaded actuation runs are sufficiently accurate in MODEL A, MODEL C1 and MODEL C2. The opposing load actuation travel computational evaluations are generally unsatisfying because of the overestimation of the actuation rate itself in MODEL A, MODEL B, MODEL C1 and MODEL C2. The over-stall condition when an opposing load actuation run is commanded produces the marked rate overestimation in MODEL A and the high underestimation in MODEL C1 and MODEL C2.

MODEL B is completely unsatisfying when $XS > XSS$, while it is quite equivalent to MODEL A if $XS \leq XSS$.

In conclusions, the considered approaches to the typical fluid dynamic non-linearities, characterising the proportional control valves, present some deficiencies, specifically in the nonlinear fields; further studies, able to produce more efficient algorithms, are necessary, in order to enhance the capability of performing acceptable simulations of all the possible working conditions.

8 LIST OF SYMBOLS

Clk	Leakage coefficient
Com	Servomechanism position command
DXJ	Motor element velocity
FR	Load acting on the motor element
GP	Pressure gain
GQ	Flow gain
GPQ	Pressure to flow gain ratio GP/GQ
P12	Actual differential pressure
P12P	Zero-flow controlled differential pressure
PSR	Supply/return differential pressure
QLk	Leakage flow
QJ	Working flow
XJ	Motor element position
XS	Spool displacement
XSM	Spool end of travel displacement
XSS	P12P saturation spool displacement

REFERENCES

- [1] Borello L., Villero G., Modello matematico completo di valvole di comando per azionamenti idraulici. *NT Tecnical & Tecnologia*, No. 1, pp. 39-47, 1991.
- [2] Borello L., Villero G., Confronto fra modelli semplificati di valvole di comando. *XI A.I.D.A.A. National Congress*, Forlì (Italy), 14-18 October 1991.
- [3] Jacazio G., Borello L., A non-linear model of an electro-hydraulic servo system with axial piston hydraulic motor. *7th International Fluid Power Symposium*, Bath (UK), 16-18 September 1986.

EPI.Q-1.2, A HYBRID MOBILE MINI ROBOT WITH A RECONFIGURABLE THREE WHEELED LOCOMOTION UNIT

Giuseppe Quaglia, Walter Franco, Daniela Maffiodo, Silvia Appendino, Riccardo Oderio

Dipartimento di Meccanica, Politecnico di Torino - C.so Duca degli Abruzzi, 24 - 10129 Torino - ITALY

ABSTRACT

This document presents *Epi.q-1.2*, a smart mini robot able to move on flat, inclined, undulating or uneven terrain, to climb over obstacles, to go up stairs and to change its kind of locomotion from a rolling (on wheels) to a stepping (on legs) one. The kind of locomotion changes automatically according to ground conditions or thanks to an axial device. Moreover robot locomotion unit can vary its geometry from a closed configuration to an open one: the first configuration is suitable to reach restricted spaces and the second one to get over high obstacles. All these kinds of functioning are obtained thanks to its innovative driving device that consists of a double epicyclic gearing and an axial device, able to lock or free some DOFs along the kinematic chain. *Epi.q-1.2* consists of three elements: the forecarriage, the central body and the rear axle, these three elements are linked by two mutually perpendicular cylindrical joints that grant to the robot great mobility and a correct contact between wheels and ground, even in presence of uneven terrain. *Epi.q-1.2* overall dimensions are about 160×360×280 mm (height×length×width) and weighs about 2,6 kg. The robot was designed on the basis of the results of some kinematic and dynamic models presented in this paper. It was experimentally tested on flat ground, slopes, uneven terrain, it goes up stairs and climbs over 90 mm obstacles, that are 72% of the locomotion unit height.

Keywords: mobile robot, hybrid locomotion, stair climbing

1 INTRODUCTION

In the last few years the evolution of mobile robotics leads to build hybrid prototypes, aiming to comprise the advantages of known wheeled, tracked and legged robots and, at the same time, to reduce their disadvantages.

Literature presents numerous solutions for robots moving on structured and unstructured environments. Some interesting prototypes, that can be considered as smart reference prototypes for this robot, are the Spacecat [1], developed by the Ecole Polytechnique Fédérale de Lausanne and characterized by its three wheeled locomotion unit, and the Whogs [2] and [3], developed by the Case Western Reserve University, with a three legged locomotion unit. Other interesting solutions are the VIPeR

[4], co-developed by Elbit Systems and Galileo Mobility Instruments and characterized by the 'Galileo Wheel' that combines wheel and track in a single component switching back and forth between the two modes within seconds, the RHex [5] and [6], developed by the Carnegie Mellon Robotics Institute and characterized by compliant leg elements that provide dynamically adaptable legs and a mechanically self-stabilized gait, the Packbot [7], developed by iRobot and characterized by 'flippers' that enable the robot to climb over obstacles, self right itself and climb stairs, and another vehicle [8] developed in Ibaraki University (Japan) and characterized by a polymorphic locomotion tracked crawler that provides two kinds of outputs, in different form, only using one actuator thanks to a planetary gear reducer.

Epi.q mini robots presents an innovative 'wheel-leg' hybrid locomotion design consisting in a suitable planetary gearing which allows to obtain different kinds of motions with only one motor for each locomotion unit. The first prototype, *Epi.q-1.1*, is described in previous works, [9] and [10].

Contact author: G. Quaglia¹, W. Franco², D. Maffiodo³

¹Email: giuseppe.quaglia@polito.it

²Email: walter.franco@polito.it

³Email: daniela.maffiodo@polito.it

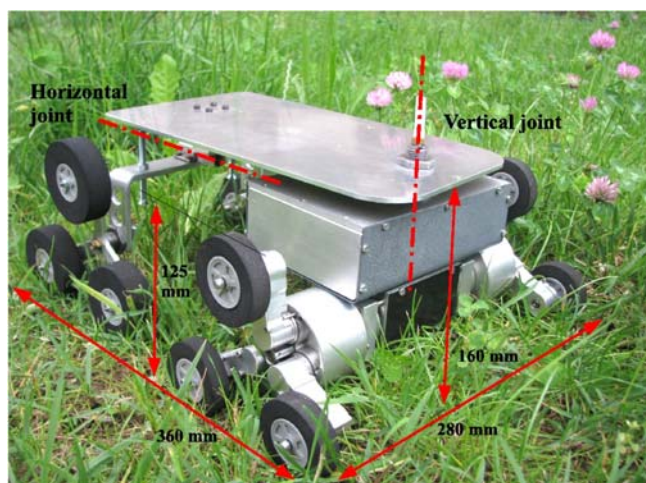


Figure 1 Side view of the Epi.q-1.2

Tests on *Epi.q-1.1* enlightened a great robot mobility on uneven terrain, in going up stairs and in climbing over obstacles, but also some limits: a disadvantageous disposition of weights, the lack of space for the payload, a rear axle not suited for climbing operations and the electronics exposed to danger.

For this reason a second *Epi.q* prototype, able to get over these limits, was built: *Epi.q-1.2*, the mobile mini robot presented in this article.

Application fields are numerous: monitoring, surveillance and intervention tasks in restricted spaces, like in rescuing operations after earthquake, operations in potentially dangerous environments, stair climbing wheel-chair applications or robotic transport devices. Stair climbing wheelchairs are a particularly interesting issue: the same locomotion of *Epi.q-1.2* may be adapted to propose a valid alternative to a wide range of existing solutions, both motor and hand driven, which have been developed to help disabled in overcoming barriers. Remarkable devices designed in this field are for example [11] and [12].

In the past authors have already studied stair climbing hybrid robots like in [13], [14], [15], [16] and [17].

Aim of this article is to discuss different aspects of the project: the *Epi.q-1.2* design is described, as well as its different kinds of motion with some mentions to the kinematic analysis, an analytical study of the motion transition conditions is exploited and some experimental results of *Epi.q-1.2* are shown.

2 EPI.Q-1.2 DESIGN

Epi.q-1.2 consists of three elements: the forecarriage, the central body and the rear axle.

These three elements are linked by two mutually perpendicular cylindrical joints, as shown in Fig.1; the vertical joint allows the relative rotation between forecarriage and the rest of the robot while the horizontal joint permits the rotation between rear axle and the rest of the robot, allowing a correct contact between wheels and

ground, also on uneven terrain. The front vertical cylindrical joint permits a differential steering, similar to the one obtained by robots with two front wheels and one pivoting rear wheel. Robot trajectories are generated by controlling wheel rotation speed of right and left locomotion units. The absence of such front joint would bring to considerable slipping on ground.

The forecarriage is composed by two anterior locomotion units, generating the traction action, linked by two boxes where motors and electronics are placed; the electronics comprises a radio-receiver device, a motors' driver and batteries. The boxes prevent motors and electronics from dust and from dangerous impacts against obstacles.

The rear axle comprises two triple wheel groups, consisting in a triangular structure free to rotate around its axis with three idle wheels placed at its vertices: this permits the robot to climb over higher obstacles with respect to the previous version.

The central body is a metal plate linking forecarriage and rear axle: here is possible to place a payload, like a video-camera or a robotic arm.

The locomotion unit consists of a gearing train, connected to a motor, and an axial device able to lock or free some DOFs (degrees of freedom) along the kinematic chain. Thanks to this particular locomotion unit the robot can move on flat, inclined or undulating ground, get over obstacles and go up stairs (these kinds of motion will be explained in detail in next sections). Moreover the locomotion unit can also change its geometry, from a closed configuration to an open one, as shown in Fig.2: the first configuration is suitable to reach restricted spaces and the second one to get over high obstacles.

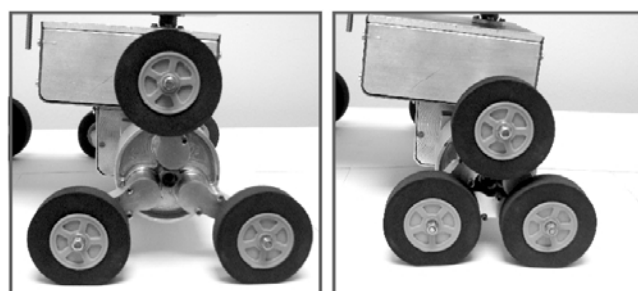


Figure 2 Locomotion unit in open (on the left) and in closed (on the right) configuration

In order to limit the complexity of *Epi.q* prototype only front locomotion units are able to automatically change their configuration, while the rear triple wheels groups have the possibility to manually change the configuration from an open to a closed one by differently positioning the wheels along the group legs. Future work foresees a prototype with four identical locomotion units. Finally the particular geometry of the locomotion unit allows to reduce robot pitching when it moves on uneven terrain, thanks to the fact that locomotion unit is free to rotate around its axis.

An important weight and overall dimension decrease is obtained using only one motor and one axial device for each locomotion group.

A remote control unit allows robot control: a radio signal is sent to the receiver device, located on the robot, that transmits the information to a motor driver, providing motors voltage. Robot trajectory is consequently controlled: straight trajectory is obtained using the same speed for the two motors, left steer is obtained when right motor speed is higher than left one, and vice versa. The present robot is not provided with sensors and therefore the operator directly controls the advancing direction by means of the remote control. Future work foresees a closed loop position control.

Robot weighs about 2.6 kg and its overall dimensions are 160×360×280 mm (h × l × w), with a locomotion unit that measures 125 mm in height.

It is equipped with two gearmotors, one for each locomotion unit; declared motor characteristics are a no load angular speed of 62 rpm and a maximum torque of about 1 Nm.

3 DESCRIPTION OF DIFFERENT KINDS OF MOTION

A detailed description of the locomotion unit configuration during different kinds of motion is given in this paragraph, as well as some mentions to the system kinematical analysis. Epi.q is able to move on flat, inclined or undulating ground, to go up stairs, to climb over obstacles and to change the locomotion unit configuration from a closed to an open one. Each locomotion unit is driven by only one motor and one axial device, which permit to realize all these kinds of motion.

3.1 DESCRIPTION OF THE LOCOMOTION GROUP

Locomotion unit design stems from the assumption that different motions can be obtained using one transmission system, if the transmission kinematical chain can be modified by locking or freeing DOFs along it.

Locomotion unit consists therefore of a double epicyclic train and of an axial device which allows the DOF hindering, as depicted in the kinematic scheme of Fig. 3, where only one arm is represented.

The locomotion unit elements are: input ring gear (1) (linked with the motor), planet carrier (2), planet gear (3), solar gear (4), sliding solar gear (5), leg planet gear (6), pulleys (7) and (8), belt (9) and wheel (10).

Some of these elements are always rigidly connected: pulley (7) is always fixed to planet gear (3) and it drives pulley (8) - always fixed to wheel (10) - by means of the belt transmission (9).

The axial device consists of a mini-motor (11) linked to a lead screw system (12), as can be seen in Fig.3. This system allows the sliding solar gear (5) to move axially and couple with solar gear (4): this modifies the kinematical chain and the gearing changes its functioning mode.

Three different kinds of motion, corresponding to three different gearing configurations, are possible: "Automatic

& climbing mode", "Opening & closing legs mode", and "Rotating legs mode". The motions will be analyzed in following paragraphs whereas the different gearing conditions are to be seen, respectively, in Fig. 4a, Fig. 4b and Fig. 4c.

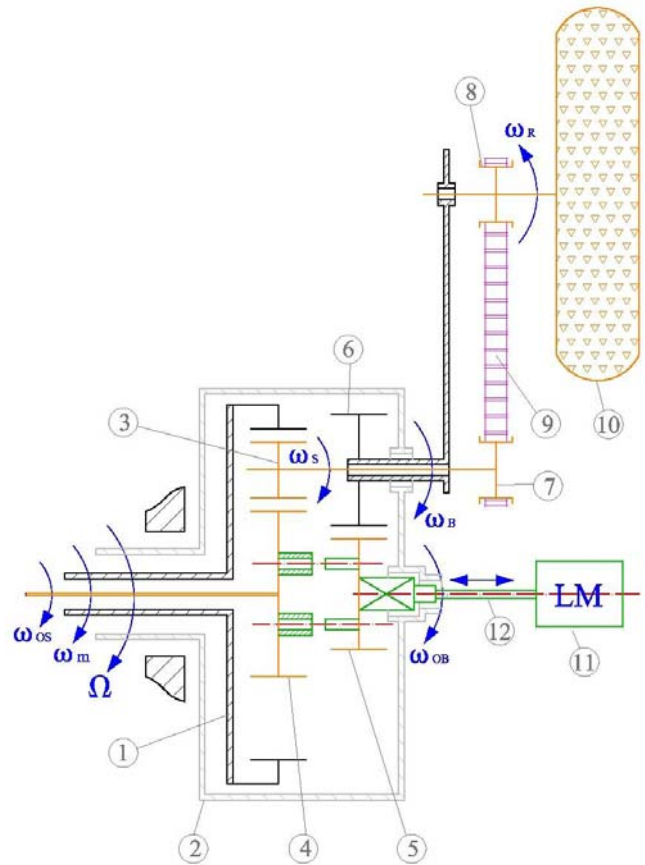


Figure 3 Kinematic scheme of the locomotion unit (labels are referred to Table 1)

Table 1 - Nomenclature and geometrical ratios

Nomenclature	Symbol or subscript	Radius	Absolute rotation speed	Element number
Input ring gear	m	r_m	ω_m	1
Planet carrier			Ω	2
Planet gear	S	r_S	ω_S	3
Solar gear	OS	r_{OS}	ω_{OS}	4
Sliding solar gear	OB	r_{OB}	ω_{OB}	5
Leg planet gear	B	r_B	ω_B	6
Leg	B		ω_B	
Pulley fixed to planet gear	PS	r_{PS}	ω_S	7
Pulley fixed to wheel	PR	r_{PR}	ω_R	8
Belt				9
Wheel	R	r_R	ω_R	10

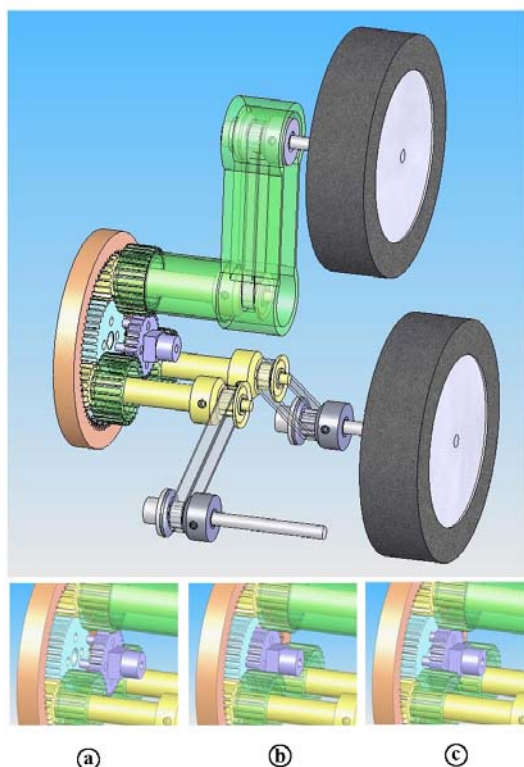


Figure 4 Locomotion unit in different configurations:
 a) advancing & automatic climbing mode
 b) opening and closing legs mode
 c) rotating legs mode

3.2 ADVANCING & AUTOMATIC CLIMBING MODE

This is the common robot functioning mode: in this configuration (see Fig. 4a) it moves on flat, inclined or undulating ground, it goes up stairs and it climbs over obstacles. Depending on local friction and dynamic conditions, the robot changes its functioning - from advancing to climbing - automatically, without any operator intervention.

Sliding solar gear (5) is in its right hand side position and, thanks to a prismatic coupling, it is fixed to the planet carrier (2): this hinders a relative rotation between the two elements. Sliding solar gear (5) is also always meshed with leg planet gears (6): this coupling locks the legs in a prefixed position, with respect to planet carrier, either in closed configuration or in open one.

3.2.1 Advancing

In "Advancing" mode robot moves on flat, inclined or undulating ground, with its legs rigidly connected to the planet carrier either in open or in closed configuration.

Planet carrier is free to rotate around its axis, but the group balance and the contact between bottom wheels and ground constrain its angular position.

In the hypothesis of locomotion on flat ground, the contact between two bottom wheels and ground hinders the planet carrier rotation.

The gear ratio in this locomotion condition is expressed as follows:

$$i_A = \frac{\omega_R}{\omega_m} = k_e \cdot k_c$$

where k_e and k_c are defined as:

$$k_e = r_m / r_s$$

$$k_c = r_{PS} / r_{PR}$$

The significant speed for this motion is the linear velocity of the robot, which can be expressed as a function of the motor rotation speed:

$$v_A = \omega_r \cdot r_R = \omega_m \cdot i_A \cdot r_R = \omega_m \cdot k_e \cdot k_c \cdot r_R$$

3.2.2 Automatic climbing

When the robot is moving forward in "Advancing" mode and it bumps against a step or an obstacle, the local friction conditions between wheel and obstacle may be strong enough to block the wheel and generate the rotation of the locomotion unit around the stopped wheel: in this case the robot automatically climbs over the step or obstacle.

The gear ratio for this motion is expressed as follows:

$$i_{AC} = \frac{\Omega}{\omega_m} = \frac{k_e \cdot k_c}{k_e \cdot k_c - 1}$$

In this case the significant speed is the planet carrier angular speed, which can be expressed as:

$$\Omega = \omega_m \cdot i_{AC} = \omega_m \cdot \frac{k_e \cdot k_c}{k_e \cdot k_c - 1}$$

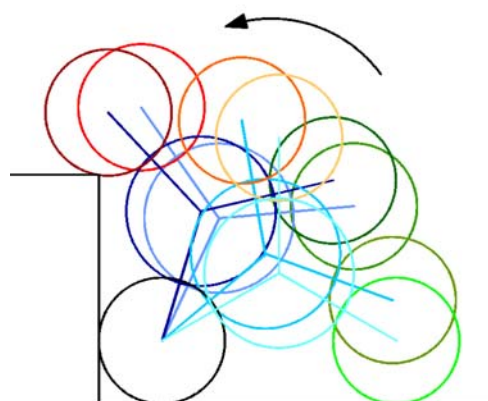


Figure 5 Scheme of the locomotion unit during step climbing operation

The planet carrier dimensions are such to permit the surpassing of almost all obstacles without interference. In

closed configuration the planet carrier is protected by the wheels and therefore can not bump against obstacles. In open configuration it may happen that the planet carrier touches the obstacle: we experimentally verified that the robot gets anyhow over the obstacle with a slightly irregular motion which combines advancing and climbing modes.

The threshold obstacle height can be seen in Fig. 5, where a scheme with true dimensions depicts the locomotion unit climbing a step with height equal to 70% of the locomotion unit height.

The revolution of the locomotion unit may also be triggered by robot acceleration or by slope, if these exceed a limit value, as will be exploited in § 4.

3.3 OPENING AND CLOSING LEGS MODE

The locomotion unit can change its configuration from an open to a closed one (see Fig. 2) by legs rotating. This functioning permits the robot to be more agile in obstacle surpassing (open configuration) and also to adapt itself to move in spaces with reduced height (closed configuration) with a properly designed rear axle.

In this case the axial device shifted sliding solar gear (5) towards solar gear (4) and coupled with it, whereas (5) is no more engaged in planet carrier (2), as shown in Fig. 4b. This motion occurs in two stages in order to avoid liabilities of the gearing: first sliding solar gear (5) couples with solar gear (4), then sliding solar gear (5) is disconnected from planet carrier (2).

Slow motor rotation and suitable elastic elements allow a correct axial engagement between sliding solar gear (5) and solar gear (4) fitting.

For a correct functioning the planet carrier angular speed must be null, and this is possible by including a brake into the device.

The gear ratio is expressed as:

$$i_{OCL} = \frac{k_e \cdot k_{OB}}{k_e - 2}$$

and the legs angular speed may be expressed in function of motor rotation speed:

$$\omega_B = \omega_m \cdot i_{OCL} = \omega_m \cdot \frac{k_e \cdot k_{OB}}{k_e - 2}$$

where k_{OB} is defined as:

$$k_{OB} = r_{OB} / r_B$$

Depending on friction conditions between wheels and ground, this functioning implies a relative slipping between wheels and ground or a whole robot advancing during opening and closing operations.

3.4 ROTATING LEGS MODE

When the robot can not climb an obstacle in "automatic climbing mode" because the friction forces are not great enough or when it moves upon an uneven terrain where the wheels slip, another operation mode permits to transform the whole locomotion unit into a rigid body, which rotates around its axis.

Fig. 4c shows the gearing configuration for this functioning mode: sliding solar gear (5) is shifted, by means of the axial device, into an intermediate position, so to be simultaneously engaged with the solar gear (4) and with the planet carrier (2). The whole locomotion unit acts therefore as a rigid body and the motor rotation provides the rotation of the whole group, as if it was a single rotating element.

Excessive wheels wear is a possible drawback of this functioning since remarkable slipping conditions occur between wheel and obstacle.

4 TRANSITION BETWEEN ADVANCING AND AUTOMATIC CLIMBING MODE

As described in § 3.2, the drive system employed in robot locomotion unit exhibits the interesting characteristic of generating both the wheeled motion (advancing functioning) and the legged motion (automatic climbing functioning). The transition between different kinds of motions occurs at least in three motion conditions. The first one takes place during normal advancing, when the robot acceleration overcomes a limit value: this happens because motor torque is roughly proportional to robot acceleration and there is a torque limit value that triggers the planet carrier revolution, causing legged motion. The second one ensues during uniform speed advancing on an inclined surface: beyond a limit slope value the robot motion turns to "automatic climbing", because the motor torque is proportional to the slope. The last condition occurs when the robot faces big obstacles, able to stop the front wheel motion.

In this paragraph the investigation of transition conditions is exploited, by means of simplified analytical models, considering the influence of gear ratios, locomotion unit efficiency and robot geometry (rear and front axle weight distribution, height of the center of mass, leg and wheel dimensions).

These analytical models are useful design tools because they provide gear ratios and robot geometry corresponding to chosen transition conditions for different motions.

4.1 TRANSITION DUE TO LIMIT ACCELERATION (MOTION ON FLAT SURFACE)

The following simplifying hypothesis are assumed:

- the rear axle, central body and forecarriage weight forces resultant is considered as a force applied on the center of mass, G;
- locally rear axle, forecarriage and locomotion unit masses are negligible;
- rolling friction and bearing friction are negligible

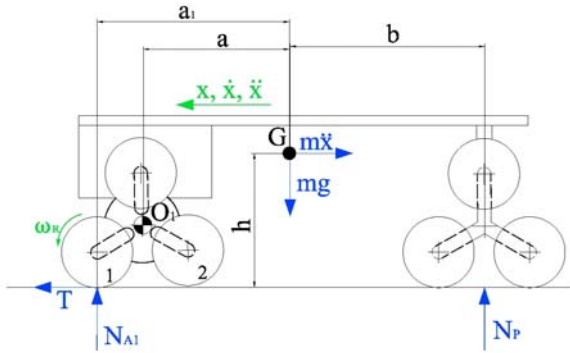


Figure 6 Robot free body diagram in detachment limit condition

The robot free body diagram, depicted in Fig. 6, describes the detachment limit condition in which front axle wheel, marked as 2, brushes the ground and so no more forces are exchanged.

Following equations represent the simplified model. Locomotion unit efficiency leads to:

$$C_m = C_R \frac{i_A}{\eta} \quad (\text{with } i_A = \frac{\omega_R}{\omega_m} = k_e \cdot k_c; \Omega = 0) \quad (1)$$

Robot equilibrium equations are:

$$mgb - mh\ddot{x} - N_{A1}(a_1 + b) = 0 \quad (2)$$

$$N_{A1} + N_P = mg \quad (3)$$

$$T = m\ddot{x} \quad (4)$$

Rotational equilibrium of the locomotion unit and of wheel 1 (free body diagram in Fig. 7) lead to:

$$C_m - TR_1 \sin \alpha - N_{A1} R_1 \cos \alpha = 0 \quad (5)$$

$$C_R = T \cdot r_R \quad (6)$$

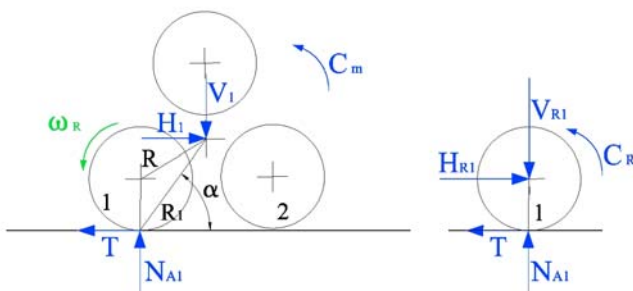


Figure 7 Free body diagram of the locomotion unit and of wheel 1

Equations from Eq. (1) to Eq. (6) allow to write:

$$\frac{i_A}{\eta} = \frac{C_m}{C_R} = \frac{R_1}{r_R} \left[\sin \alpha + \left(\frac{b}{a_1 + b} \cdot \frac{g}{\ddot{x}} - \frac{h}{a_1 + b} \right) \cos \alpha \right] \quad (7)$$

Moreover, robot geometry determines the following equations:

$$\frac{R_1}{r_R} = \sqrt{1 + \left(\frac{R}{r_R} \right)^2 - 2 \frac{R}{r_R} \cos \left(\frac{2}{3} \pi \right)} \quad (8)$$

$$\alpha = \frac{\pi}{2} - \arcsin \left(\frac{R}{R_1} \sin \frac{\pi}{3} \right) \quad (9)$$

Eq. (7) expresses the relationship between limit acceleration and ratio i_A/η : graphically this is a curve which divides the functioning space in two fields, corresponding to two different kinds of motion. Curve parameters are the ratio R_1/r_R , between legs and wheel radius, and the position of the center of mass ($b/(a_1+b)$ and $h/(a_1+b)$).

Eq. (7) can give some suggestions for the choice of a suitable gear ratio i_A so to obtain a wheeled motion inside a fixed acceleration range. This value is however a very rough estimate because of efficiency variability and uncertainty. Influence of parameters can be better explained by reversing Eq. (7):

$$\ddot{x} = \frac{\frac{b}{a_1 + b} g \cos \alpha}{\frac{i_A}{\eta} \cdot \frac{r_R}{R_1} - \sin \alpha + \frac{h}{a_1 + b} \cos \alpha} \quad (10)$$

For a selected locomotion unit (i_A/η fixed), the limit acceleration value, triggering the transition between wheeled and legged motion, increases if:

- $b/(a_1+b)$ is increasing, that is the center of mass moves towards front axle;
- r_R/R_1 is decreasing, that is the wheels are smaller or the locomotion unit is in open configuration;
- $h/(a_1+b)$ is decreasing, that is the center of mass is lower.

Fig. 8 shows the curves of Eq. (7) with Epi.q 1.2 in open and in closed configuration.

The area under the curve identifies the field of assured wheeled motion because it implies torques C_M lower than the one expressed by Eq. (5), and this condition is observed when wheel 2 is in contact with ground. The area over the curve is characterized by the legged motion with the planet carrier revolution, because it implies torques C_M bigger than the one expressed by Eq. (5), in this case it is not possible to omit the inertial effects on the locomotion unit. The yellow rectangle highlights the experimental range of values for the Epi.q 1.2 ratio i_A/η .

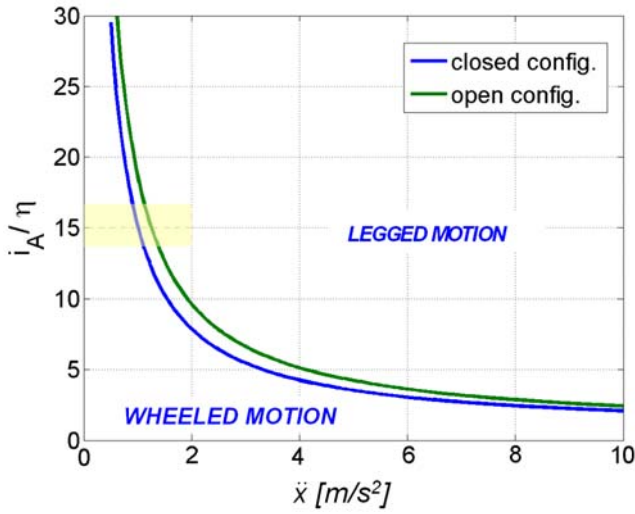


Figure 8 Relationship between limit acceleration \ddot{x} and ratio i_A/η , showing the transition due to limit acceleration in case of motion on flat surface

4.2 TRANSITION DUE TO LIMIT SLOPE (UNIFORM SPEED MOTION ON INCLINED SURFACE)

Referring to Fig. 9 free body diagram, it is possible to analyze slope conditions which trigger the automatic climbing mode.

By adopting the same simplifying hypotheses of § 4.1, the equilibrium equations become:

$$mgb \cos \delta - mgh \sin \delta - N_{A1} (a_1 + b) = 0 \quad (11)$$

$$N_{A1} + N_P = mg \cos \delta \quad (12)$$

$$T = mg \sin \delta \quad (13)$$

Moreover, Eq. (1), Eq. (5), and Eq.(6) are still applicable and therefore it is possible to obtain the relationship, in transition conditions, between gear ratio and slope:

$$\frac{i_A}{\eta} = \frac{R_1}{r_R} \left[\sin \alpha + \left(\frac{b}{a_1 + b} \cdot \frac{1}{\tan \delta} - \frac{h}{a_1 + b} \right) \cos \alpha \right] \quad (14)$$

Eq. (14) and Eq. (7) are similar: it is possible to find Eq.(14) by substituting $1/\tan \delta$ instead of g/\ddot{x} in Eq. (7). This is clear, since the only difference between the free body diagrams is due to the resulting forces on the center of mass. In the first case the ratio between parallel and perpendicular force components - with respect to the advancing plane - is $m\ddot{x}/mg$, in the second case it is $mg \sin \delta / mg \cos \delta$. The diagrams are therefore equal if $\ddot{x}/g = \tan \delta$.

Accelerating along the advancing plane is therefore equivalent to climbing a slope with constant speed, for what concerns equilibrium.

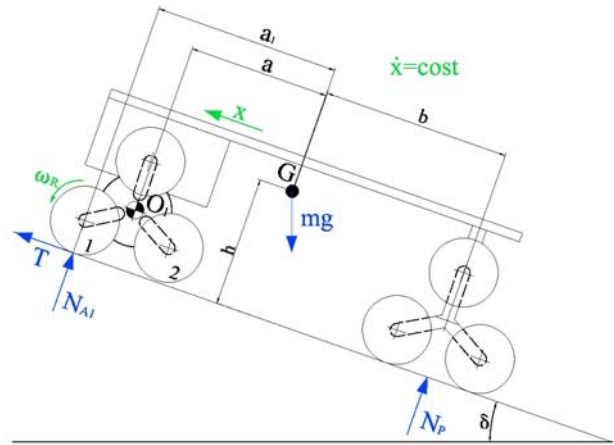


Figure 9 Robot free body diagram in take-off limit condition

Also in this case a brief analysis to evaluate the weight of single parameters on the resulting relationship can be accomplished. Eq. (14) can be inverted and rewritten as:

$$\tan \delta = \frac{\frac{b}{a_1 + b}}{\left(\frac{i_A}{\eta} \cdot \frac{r_R}{R_1} - \sin \alpha \right) \frac{1}{\cos \alpha} + \frac{h}{a_1 + b}} \quad (15)$$

For a selected locomotion unit (i_A/η fixed), the limit slope value, triggering the transition between the wheeled and the legged motion, increases if:

- $b/(a_1+b)$ is increasing, that is if the center of mass moves towards front axle;
- r_R/R_1 is decreasing, that is if the wheels are smaller or the locomotion unit is in open configuration;
- $h/(a_1+b)$ is decreasing, that is if the center of mass is lower.

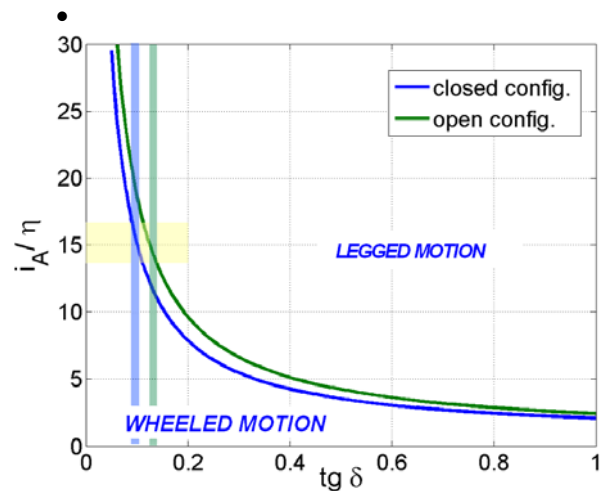


Figure 10 Relationship between limit slope δ and ratio i_A/η , showing the transition due to limit slope in case of motion on inclined surface

Eq. (14) is depicted in Fig.10: the light blue and green rectangles express the experimental range of $\tan\delta$ values found for Epi.q 1.2 transition in closed and in open configuration, respectively. The yellow rectangle represents the range of i_A/η values: its width depends on efficiency fluctuations. Although the curves stem from a simplified model they adequately describe the transition conditions. Other comments are corresponding to the ones for Fig. 8, by simply substituting slope percentage instead of acceleration.

For the sake of concision the dynamic analysis concerning the surpassing of an obstacle is not illustrated.

5 EXPERIMENTAL RESULTS

The robot was experimentally tested on flat, inclined and undulating ground, in open field and in structured environments; the results are below collected.

Epi.q-1.2 can move on flat ground reaching the maximum speed of about 0.5 m/s, this value depends only on motor power and on maximum speed and can easily increased by choosing different motors, without any problems connected to vehicle dynamic.

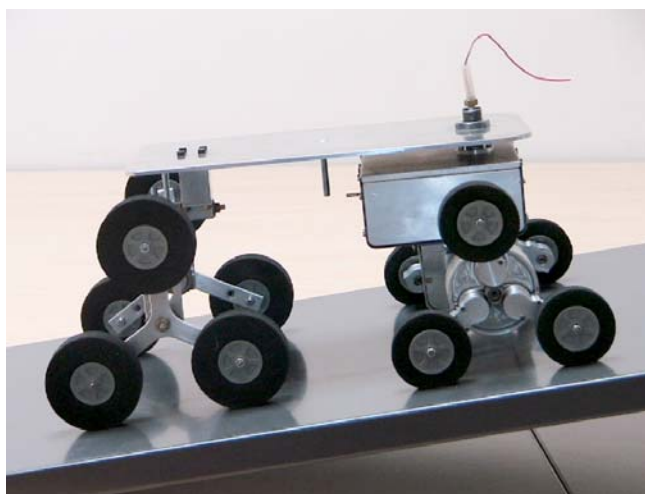


Figure 11 Epi.q-1.2 moving on inclined ground



Figure 12 Epi.q-1.2 getting over obstacle

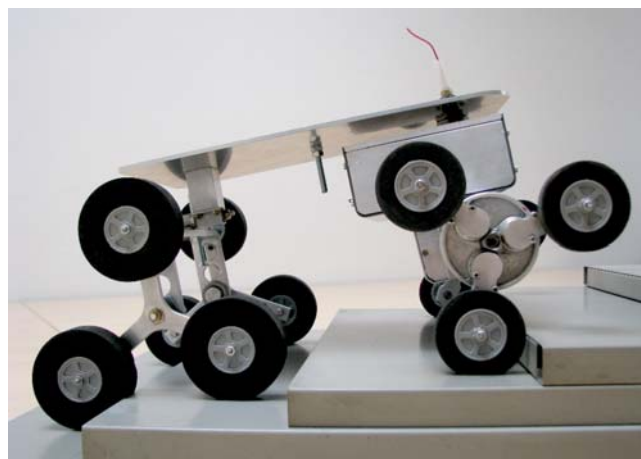


Figure 13 Epi.q-1.2 climbing stairs

When the robot, kept in open configuration, moves on inclined ground, Fig. 11, the robot automatically changes its locomotion from "advancing" to "automatic climbing" mode when the slope is between 12% and 14,3%; if the robot is kept in closed configuration, the transition between these two locomotion modes happens when ground slope is between 8,6% and 11%.

Moreover the robot can climb over obstacles with maximum height of 90 mm, that is 72% of locomotion unit height, Fig.12, and go up stairs, Fig. 13.

The robot was tested in open field, moving on uneven terrain, and in structured environment, in these conditions it is possible to better appreciate the robot "advancing and automatic climbing mode".

These tests permit to roughly estimate Epi.q-1.2 locomotion unit efficiency as about 25%.

6 CONCLUSIONS

This work presents the design of a new hybrid mini robot. It is a small and compact device which is able to move on uneven ground and in presence of obstacles. It is also very adaptable, thanks to its ability of changing configuration: this functioning can be useful for transportation or for operations in restricted environments.

The different kinds of motion, which permit the employment on various kinds of terrain, are obtained using, for each locomotion unit, a single motor and an axial device, able to activate both the advancing and the configuration change.

The transition between advancing and automatic climbing mode may be triggered by robot acceleration, by a slope or by an obstacle. The article illustrates the analytical investigation of the transition conditions in these different cases.

Experimental results, concerning motion ability on different kinds of terrain and transition conditions, are shown and compared with the theoretical study.

Future work foresees further testing and an eventual model review in order to find a better correspondence between analytical and experimental values.

A new prototype is foreseen with a new mechanical drive provided only with gears. This solution will both decrease internal friction actions (and consequently increase the efficiency) and lead to a stronger drive device, of course with the same abilities of the previous version.

Moreover future applications could be specific tasks customization, in particular stair climbing wheelchair solutions and video-surveillance robots.

7 ACKNOWLEDGMENTS

This work has been developed in *PRIN 2005*, protocol number 20055099809 - "Mini-robotic system for advanced technological applications".

REFERENCES

- [1] Siegart R., Lauria M., Mausli P. and Van Winnendael M., Design and Implementation of an Innovative Micro-Rover. *Proc. of Robotics 98, the 3rd Conference and Exposition on Robotics in Challenging Environments*, Albuquerque (New Mexico), April 26-30, 1998.
- [2] Allen T.J., Quinn R.D., Bachmann R.J. and Ritzmann R.E., Abstracted Biological Principles Applied with Reduced Actuation Improve Mobility of Legged Vehicles. *Proc. of the 2003 IEEURSJ - Int. Conference on Intelligent Robots and Systems*, Las Vegas (Nevada), October, 2003.
- [3] Quinn R.D., Nelson G.M., Bachmann R.J., Kingsley D.A., Offi J.T., Allen T.J., and Ritzmann R.E., Parallel complementary strategies for implementing biological principles into mobile robots. *The International Journal of Robotics Research*, Vol. 22, No. 3, pp. 169-186, 2003.
- [4] Elbit Systems and Galileo Mobility Instruments, <http://www.galileomobility.com>
- [5] Altendorfer R., Moore N., Komsuoglu H., Buehler M., Brown Jr. H.B., McMordie D., Saranli U., Full R. and Koditschek D.E., Rhex: A biologically inspired hexapod runner. *Autonomous Robots*, Vol. 11, No. 3, pp.: 207-213, 2001.
- [6] Saranli U., Rizzi A.A. and Koditschek D.E., Model-based dynamic self-righting maneuvers for a hexapedal robot. *The International Journal of Robotics Research*, Vol. 23, No. 9, pp.:903-918, 2004.
- [7] Mourikis A.I., Trawny N., Roumeliotis S.I., Helmick D.M. and Matthies L., Autonomous stair climbing for tracked vehicles. *The International Journal of Robotics Research*, Vol. 26, No. 7, pp: 737-758, 2007.
- [8] Lan G., Ma S., Inoue K. and Hamamatsu Y., Development of a novel crawler mechanism with polymorphic locomotion. *Advanced Robotics*, Vol. 21, No. 3-4, pp. 421-440, 2000.
- [9] Oderio R., Progetto di robot mobile a locomozione ibrida riconfigurabile. *Thesis*, Politecnico di Torino, Mechanical Department, 2006.
- [10] Quaglia G., Appendino S., Franco W. and Maffioldo D., Design of a minirobot with transformable locomotion. In: *Proc. of AIMETA 2007*, Brescia (Italy), September 11-14, 2007.
- [11] Morales R., Feliu V., Gonzalez A. and Pintado P., Kinematic Model of a New Staircase Climbing Wheelchair and its Experimental Validation. *The International Journal of Robotics Research*, Vol. 25, No. 9, pp. 825-841, 2006.
- [12] Kenneth Ray Cox, Battery powered stair-climbing wheelchair, US6484829, 26 November, 2002
- [13] Quaglia G., Belforte G. and Ferraresi C., Problems in locomotion of legged mobile robots. *Proc. of ISIR - International Society for Intelligent Research*, Copenhagen (Denmark), pp.367-372, October 21, 1990.
- [14] Quaglia G. and Ferraresi C., A new hybrid locomotion mobile robot for semi-structured environments. *Proc. of RAAD - The International Workshop on Robotics in Alpe-Adria-Danube Region*, Krems (Austria), pp.SU5.5 - 1/9, June, 1993.
- [15] Quaglia G. and Ferraresi C., A high-performance mobile robot for use in domestic and public environments. *Proc. of ICAR - Int. conference on Advanced Robotics*, Sant Feliu de Guixols (Spain), pp.925-931, September 20-22, 1995.
- [16] Quaglia G., Ferraresi C. and Sambuelli L., Wheeled robot for geophysical survey. *Proc. of RAAD - Robotics in Alpe Adria Region*, Vienna (Austria), May 16-18, 2001.
- [17] Quaglia G., Ferraresi C. and Gherlone G., Real time trajectory generation for vehicle position control. *Proc. of IEEE ICIT - International Conference on Industrial Technology*, Bangkok (Thailand), Vol. I, pp.169-174, December 11-14, 2002.

TEMPLATE FOR PREPARING PAPERS FOR PUBLISHING IN INTERNATIONAL JOURNAL OF MECHANICS AND CONTROL

Author1* Author2**

* affiliation Author1

** affiliation Author2

ABSTRACT

This is a brief guide to prepare papers in a better style for publishing in International Journal of Mechanics and Control (JoMaC). It gives details of the preferred style in a template format to ease paper presentation. The abstract must be able to indicate the principal authors' contribution to the argument containing the chosen method and the obtained results. (max 200 words)

Keywords: keywords list (max 5 words)

1 TITLE OF SECTION (E.G. INTRODUCTION)

This sample article is to show you how to prepare papers in a standard style for publishing in International Journal of Mechanics and Control.

It offers you a template for paper layout, and describes points you should notice before you submit your papers.

2 PREPARATION OF PAPERS

2.1 SUBMISSION OF PAPERS

The papers should be submitted in the form of an electronic document, either in Microsoft Word format (Word'97 version or earlier).

In addition to the electronic version a hardcopy of the complete paper including diagrams with annotations must be supplied. The final format of the papers will be A4 page size with a two column layout. The text will be Times New Roman font size 10.

2.2 DETAILS OF PAPER LAYOUT

2.2.1 Style of Writing

The language is English and with UK/European spelling. The papers should be written in the third person. Related work conducted elsewhere may be criticised but not the individuals conducting the work. The paper should be comprehensible both to specialists in the appropriate field and to those with a general understanding of the subject. Company names or advertising, direct or indirect, is not permitted and product names will only be included at the discretion of the editor. Abbreviations should be spelt out in full the first time they appear and their abbreviated form included in brackets immediately after. Words used in a special context should appear in inverted single quotation mark the first time they appear. Papers are accepted also on the basis that they may be edited for style and language.

2.2.2 Paper length

Paper length is free, but should normally not exceed 10000 words and twenty illustrations.

2.2.3 Diagrams and figures

Figures and Tables will either be entered in one column or two columns and should be 80 mm or 160 mm wide respectively. A minimum line width of 1 point is required at actual size. Captions and annotations should be in 10 point with the first letter only capitalised *at actual size* (see Figure 1 and Table VII).

Contact author: author1¹, author2²

¹Address of author1.

²Address of author2 if different from author1's address
E-mail: author1@univ1.com , author2@univ2.com

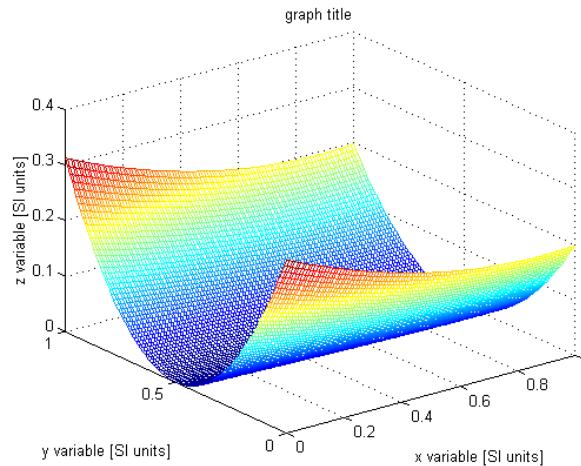


Figure 1 Simple chart.

Table VII - Experimental values

Robot Arm Velocity (rad/s)	Motor Torque (Nm)
0.123	10.123
1.456	20.234
2.789	30.345
3.012	40.456

2.2.4 Photographs and illustrations

Authors could wish to publish in full colour photographs and illustrations. Photographs and illustrations should be included in the electronic document and a copy of their original sent. Illustrations in full colour ...

2.2.5 Equations

Each equation should occur on a new line with uniform spacing from adjacent text as indicated in this template. The equations, where they are referred to in the text, should be numbered sequentially and their identifier enclosed in parenthesis, right justified. The symbols, where referred to in the text, should be italicised.

- point 1
 - point 2
 - point 3
- 1. numbered point 1
- 2. numbered point 2
- 3. numbered point 3

$$W(d) = G(A_0, \sigma, d) = \frac{1}{T} \int_0^{+\infty} A_0 \cdot e^{-\frac{d^2}{2\sigma^2} t} dt \quad (1)$$

3 COPYRIGHT

Authors will be asked to sign a copyright transfer form prior to JoMaC publishing of their paper. Reproduction of any part of the publication is not allowed elsewhere without permission from JoMaC whose prior publication must be cited. The understanding is that they have been neither previously published nor submitted concurrently to any other publisher.

4 PEER REVIEW

Papers for publication in JoMaC will first undergo review by anonymous, impartial specialists in the appropriate field. Based on the comments of the referees the Editor will decide on acceptance, revision or rejection. The authors will be provided with copies of the reviewers' remarks to aid in revision and improvement where appropriate.

5 REFERENCES (DESCRIPTION)

The papers in the reference list must be cited in the text. In the text the citation should appear in square brackets [], as in, for example, "the red fox has been shown to jump the black cat [3] but not when...". In the Reference list the font should be Times New Roman with 10 point size. Author's first names should be terminated by a 'full stop'. The reference number should be enclosed in brackets. The book titles should be in *italics*, followed by a 'full stop'. Proceedings or journal titles should be in *italics*. For instance:

REFERENCES (EXAMPLE)

- [1] Smith J., Jones A.B. and Brown J., *The title of the book*. 1st edition, Publisher, 2001.
- [2] Smith J., Jones A.B. and Brown J., The title of the paper. *Proc. of Conference Name*, where it took place, Vol. 1, paper number, pp. 1-11, 2001.
- [3] Smith J., Jones A.B. and Brown J., The title of the paper. *Journal Name*, Vol. 1, No. 1, pp. 1-11, 2001.
- [4] Smith J., Jones A.B. and Brown J., *Patent title*, U.S. Patent number, 2001.

International Journal of Mechanics and Control – JoMaC
Published by Levrotto&Bella
TRANSFER OF COPYRIGHT AGREEMENT

<p>NOTE: Authors/copyright holders are asked to complete this form signing section A, B or C and mail it to the editor office with the manuscript or as soon afterwards as possible.</p>	<p><i>Editor's office address:</i> Andrea Manuello Bertetto Elvio Bonisoli <i>Dept. of Mechanics</i> <i>Technical University – Politecnico di Torino</i> <i>C.so Duca degli Abruzzi, 24 – 10129 Torino – Italy</i> <i>e_mail: jomac@polito.it</i> <i>fax n.: +39.011.564.6999</i></p>
--	---

The article title:

By: _____

To be Published in *International Journal of Mechanics and Control JoMaC*
Official legal Turin court registration Number 5320 (5 May 2000) - reg. Tribunale di Torino N. 5390 del 5 maggio 2000

- A Copyright to the above article is hereby transferred to the JoMaC, effective upon acceptance for publication. However the following rights are reserved by the author(s)/copyright holder(s):
1. All proprietary rights other than copyright, such as patent rights;
 2. The right to use, free or charge, all or part of this article in future works of their own, such as books and lectures;
 3. The right to reproduce the article for their own purposes provided the copies are not offered for sale.
- To be signed below by all authors or, if signed by only one author on behalf of all co-authors, the statement A2 below must be signed.*

A1. All authors:

SIGNATURE _____ DATE _____ SIGNATURE _____ DATE _____

PRINTED NAME _____ PRINTED NAME _____

SIGNATURE _____ DATE _____ SIGNATURE _____ DATE _____

PRINTED NAME _____ PRINTED NAME _____

A2. One author on behalf of all co-authors:

"I represent and warrant that I am authorised to execute this transfer of copyright on behalf of all the authors of the article referred to above"

PRINTED NAME _____

SIGNATURE _____ TITLE _____ DATE _____

B. The above article was written as part of duties as an employee or otherwise as a work made for hire. As an authorised representative of the employer or other proprietor. I hereby transfer copyright to the above article to *International Journal of Mechanics and Control* effective upon publication. However, the following rights are reserved:

1. All proprietary rights other than copyright, such as patent rights;
2. The right to use, free or charge, all or part of this article in future works of their own, such as books and lectures;
3. The right to reproduce the article for their own purposes provided the copies are not offered for sale.

PRINTED NAME _____

SIGNATURE _____ TITLE _____ DATE _____

C. I certify that the above article has been written in the course of employment by the United States Government so that no copyright exists, or by the United Kingdom Government (Crown Copyright), thus there is no transfer of copyright.

PRINTED NAME _____

SIGNATURE _____ TITLE _____ DATE _____

CONTENTS

- 3 Perspectives in the Mechanization of Saffron (Crocus Sativus L.)**
F. Gambella, F. Paschino and A. Manuello Bertetto
- 9 A Study of Fatigue in High Speed Gears**
F. Curà, F. Gallo and C. Rosso
- 21 Magneto-Inductive Energy Harvesting: Application to a Computer Mouse**
E. Bonisoli and N. Manca
- 29 Methodology to Investigate the Microclimate of a Cultural Heritage Inserted in a Semi-Confined Environment**
G. Carcangiu, M. Casti, G. Desogus, P. Meloni and R. Ricciu
- 39 Proposal of Innovative Fluid Dynamic Nonlinear Servovalve Synthethic Models**
P. Alimhillaj, L. Borello and M.D.L. Dalla Vedova
- 49 Epi.q-1.2, a Hybrid Mobile Mini Robot with a Reconfigurable Three Wheeled Locomotion Unit**
G. Quaglia, W. Franco, D. Maffiodo, S. Appendino and R. Oderio

next issue titles will be from the papers of:

RAAD 2014

23th International Workshop on Robotics in Alpe-Adria-Danube Region

Smolenice Castle, Slovakia
3 - 5 September 2014